



5-2015

Wide Band Embedded Slot Antennas for Biomedical, Harsh Environment, and Rescue Applications

Yun Seo Koo

University of Tennessee - Knoxville, ykoo@vols.utk.edu

Recommended Citation

Koo, Yun Seo, "Wide Band Embedded Slot Antennas for Biomedical, Harsh Environment, and Rescue Applications." PhD diss., University of Tennessee, 2015.
https://trace.tennessee.edu/utk_graddiss/3379

This Dissertation is brought to you for free and open access by the Graduate School at Trace: Tennessee Research and Creative Exchange. It has been accepted for inclusion in Doctoral Dissertations by an authorized administrator of Trace: Tennessee Research and Creative Exchange. For more information, please contact trace@utk.edu.

To the Graduate Council:

I am submitting herewith a dissertation written by Yun Seo Koo entitled "Wide Band Embedded Slot Antennas for Biomedical, Harsh Environment, and Rescue Applications." I have examined the final electronic copy of this dissertation for form and content and recommend that it be accepted in partial fulfillment of the requirements for the degree of Doctor of Philosophy, with a major in Electrical Engineering.

Aly E. Fathy, Major Professor

We have read this dissertation and recommend its acceptance:

Syed K. Islam, Seddik M. Djouadi, Seung J. Baek

Accepted for the Council:

Dixie L. Thompson

Vice Provost and Dean of the Graduate School

(Original signatures are on file with official student records.)

Wide Band Embedded Slot Antennas for Biomedical, Harsh Environment, and Rescue Applications

A Dissertation Presented for the
Doctor of Philosophy
Degree
The University of Tennessee, Knoxville

Yun Seo Koo
May 2015

Copyright © 2015 by Yun Seo Koo.
All rights reserved.

DEDICATION

*To my beloved son, Brandon Inhoe Koo
(9.21 2012 ~ 12.6 2014)*

ACKNOWLEDGEMENTS

I would like to express my deepest and sincere gratitude to my advisor, Dr. Aly E. Fathy for providing me the inspiration that led to the completion of this dissertation. His extensive experience, superior knowledge, and expertise in the field of RF and Microwaves, have been extremely helpful in solving various technical problems throughout my research. Furthermore, his continued support and patience helped me complete my PhD degree.

I would like to extend my sincerest thanks to my beloved parents Yeon Geon Koo and Young-Sook Kang, without whose continued love and support throughout my entire life, I would not be able to complete this work. Special thanks to my wife Yun Hyung Choi and children Anthony, Brandon, Celine for their devoted love and patience for me throughout the years.

I also wish to express my sincere thanks to my committee members, Dr. Syed Kamrul Islam, Dr. Seddik M. Djouadi, and Dr. Seung J. Baek for their support and great suggestions.

Also, I would like to appreciate to Dr. Jeffrey Phillips, Dr. Robab Kazemi, Dr. Quanhua Liu to finish the hyperthermia applicator project and Dr. Richard Fink, Dr. Ahmad Hoorfar for helping me to design antennas under protection.

Thanks also go to all my lab collaborators, IT staff, supervisors and colleagues Sungwoo Lee, Mohamed Awida, Yazhou Wang, Song Lin, Ki Ryung Shin, Essam Elkhoully, Reza Ghahremani, Haofei Wang, Lingyun Ren, Mohamed Saleh, William Rhodes, Justin Forbes and many others at the University of Tennessee.

ABSTRACT

For many designers, embedded antenna design is a very challenging task when designing embedded systems. Designing Antennas to given set of specifications is typically tailored to efficiently radiate the energy to free space with a certain radiation pattern and operating frequency range, but its design becomes even harder when embedded in multi-layer environment, being conformal to a surface, or matched to a wide range of loads (environments).

In an effort to clarify the design process, we took a closer look at the key considerations for designing an embedded antenna. The design could be geared towards wireless/mobile platforms, wearable antennas, or body area network.

Our group at UT has been involved in developing portable and embedded systems for multi-band operation for cell phones or laptops. The design of these antennas addressed single band/narrowband to multiband/wideband operation and provided over 7 bands within the cellular bands (850 MHz to 2 GHz). Typically the challenge is: many applications require ultra wide band operation, or operate at low frequency. Low frequency operation is very challenging if size is a constraint, and there is a need for demonstrating positive antenna gain.

TABLE OF CONTENTS

CHAPTER I Introduction	1
1.1. Examples of Embedded Antennas	4
1.1.1. Embedded Antennas in Concrete	4
1.1.2. Implantable Microstrip Antennas for Medical Implants	5
1.1.3. Antenna Embedded in Low Permittivity Metamaterial	8
1.1.4. Gain Enhanced of Embedded Microstrip Antennas	11
1.1.5. 2.4GHz printed antennas embedded in small UAV wings.....	13
1.2. Examples of Embedded Antennas	16
1.2.1. Example I: Antenna for Hyperthermia Treatment	17
1.2.2. Example II: Embedded Antenna in Harsh Environment.....	17
1.2.3. Example III: Antennas for Vital Sign Detection through Debris and Rubbles.....	18
1.3. Challenges in Designing Embedded Antennas and systems.....	20
1.4. Contributions in Designing Embedded Antennas and Systems.....	21
CHAPTER II Development of a High SAR Conformal Antenna for Hyperthermia Tumors Treatment.....	22
2.1. Examples of Embedded Antennas	22
2.2.1 Hyperthermia Treatment	22
2.2. Hyperthermia Research by RF Engineers.....	23
2.2.1 IMS Frequency Band for Hyperthermia Treatment	23
2.3. Properties of Tissues	24
2.4. Hyperthermia Antenna Development	27
2.4.1. Hyperthermia Antenna Requirement.....	27
2.4.2. State of Art	28
2.5. Antenna Design for Hyperthermia Applicator.....	34
2.5.1. Hyperthermia Antenna Requirement.....	35
2.5.2. Microwave Hyperthermia Control Unit	38
2.5.3. Phantom Tissue Model.....	42
2.5.4. Methodology	42
2.6. Antenna Design for Hyperthermia Applicator.....	43
2.6.1. Return Loss.....	43
2.6.2. Electric Field Patterns	46
2.6.3. SAR Patterns	48
2.6.4. Effects of Patches within the Slot of the Conformal Antennas	50
2.6.5. Effects of Body Curvature.....	52
2.7. Conclusion	54
CHAPTER III Wideband Embedded Slot Antenna.....	56
3.1. Background.....	56
3.1.1. Survey of Low Profile Antennas	56
3.1.2. Slot Antennas as a Viable Candidate	59
3.2. Microstrip Slot Antennas	60
3.3. Our Proposed Solution and their advantages	66
3.3.1. Antenna Structure.....	66

3.3.2. Parametric Study	69
3.4. Numerical and Experimental Results.....	76
3.4.1. VSWR	77
3.4.2. Radiation Pattern and Gain.....	78
3.5. Conclusion	80
CHAPTER IV Enhanced System for Vital Sign Detection	81
4.1. Operation Frequency Selection.....	82
4.2. 1.5-4.5GHz UWB Pulse Radar System	84
4.2.1. Transceiver RF Front End	84
4.2.2. Conventional 1.5-4.5GHz Vivaldi Antenna and Array Design.....	89
4.3. Antenna Design Optimization with Various Walls	94
4.4. Algorithm to Enhance Vital Sign Detection	102
4.4.1. Conventional 1.5-4.5GHz Vivaldi Antenna and Array Design.....	103
4.4.2. Conventional Method.....	105
4.4.3. Logarithm Method.....	106
4.4.4. Experimental Results.....	107
4.5. Conclusion	110
CHAPTER V Conclusions and Future Work	111
5.1. Use of Metamaterials to Enhance Antenna Performance	111
5.2. Antenna for Medical Application	115
BIBLIOGRAPHY	118
APPENDIX	134
VITAE.....	138

LIST OF TABLES

Table 2.1 IMS Frequency Band for hyperthermia treatment.....	24
Table 2.2 Comparison of the performance of the different application at 434 MHz.....	33
Table 2.3 Performance comparison of the different low profile applicators at 434MHz .	34
Table 2.4 Electrical Parameters of Tissue Material at 434MHz.....	42
Table 2.5 Penetration Depth for Different Size of the Patches.....	52
Table 3.1 Various Low Profile Antennas	59
Table 4.1 Characteristics of Various Building Material	83
Table 4.2 Isolation requirement between radar transmitter and receiver.....	88
Table 4.3 Dynamic range analysis of the radar transceiver	88
Table 4.4 Performance comparison between an optimized antennas and air Antenna...	100

LIST OF FIGURES

Figure 1.1 DriveCam product from Ethertronics is a custom quad-band embedded antenna that operates over the GSM 850, GSM 900, DSC and PCS bands for sending video data over the cellular network [1].	2
Figure 1.2 Geometrical dimensions of the antennas under consideration: (a) Dipole, (b) loop, (c) Microstrip patch, and (d) PIFA [2].	5
Figure 1.3 Simulation model (left), (a) spiral and (b) serpentine antennas (in mm scale) [3].	8
Figure 1.4 Wire-based metamaterial [18].	9
Figure 1.5 Measurement setup for metamaterial characterization and measured radiation pattern at 10GHz, number of wire layers as parameter [18].	11
Figure 1.6 Geometry of electromagnetically coupled embedded microstrip antenna (left), E and H-plane radiation patterns near peak gain (right). [23]	12
Figure 1.7 Prototyped antenna array within the wing structure (left), maximum array gain (right). [24].	15
Figure 2.1 The effect and usage of thermal energy on tissues at different temperature. [1]	23
Figure 2.2 Permittivity of skin, fat, and muscle tissue.	25
Figure 2.3 Conductivity of skin, fat and muscle tissue.	26
Figure 2.4 Penetration of skin, fat and muscle tissue.	26
Figure 2.5 The water-filled applicator reduces reflection and provides variable surface cooling on the interface.	29
Figure 2.6 The conventional horn antenna applicator and the proposed Lucite Cone Applicator.	29
Figure 2.7 (a) The box-horn applicator with uniform E-field at the aperture, (b) The modified box-horn applicator with a larger aperture.	30
Figure 2.8 Various types of hyperthermia applicators.	32
Figure 2.9 The multi-layer antenna structure. Four prototypes (UT1, UT2, UT3, and UT4) have a total thickness of 0.47 cm, while prototype UT5 has an additional back-shield and a neoprene layer and its total thickness is 0.98 cm.	35
Figure 2.10 (a) Parameters of the proposed antenna in millimeter scale, (b) fabricated antenna.	37
Figure 2.11 Simulated S_{11} for different distance between the antenna and back shield.	38
Figure 2.12 Control board block diagram.	39
Figure 2.13 Simulated S_{11} with various dielectric constant of muscle.	40
Figure 2.14 Time-temperature profile from a single 60-min treatment on a dog [33].	41
Figure 2.15 Simulated S_{11} for the slot antenna with different embedded patch sizes and numbers.	44
Figure 2.16 Measured S_{11} for the slot antenna with different embedded patch sizes and their number.	44
Figure 2.17 Simulated S_{11} for various multi-layered model.	45
Figure 2.18 Tangential E-field distribution at the center of antennas.	47
Figure 2.19 (a) Antenna geometry (UT5); SAR distribution for the antenna at (b) surface, (c) 1 cm, (d) 2 cm, (e) 3 cm, (f) 4 cm in depth.	48

Figure 2.20 Simulated SAR with skin-fat-muscle-bone model.	49
Figure 2.21 Simulated and measured SAR of the antennas.	51
Figure 2.22 Simulated SAR with various curved body.	53
Figure 2.23 EFS defined with various curved surface.	54
Figure 3.1 Various Antenna Structures.	64
Figure 3.2 Permittivity of the composite panel with a thickness of 35mm.	65
Figure 3.3 Loss tangent of the panel with a thickness of 35 mm.	65
Figure 3.4 The proposed multi-layer antenna structure.	67
Figure 3.5 Parameters of the proposed antenna after optimization. L = 100, W = 100, W50 = 2.2, W1 = 15.4, W2 = 5.5, L = 100, L1 = 30, L2 = 19.8, R = 0.3, Space = 10.5 in mm scale.	68
Figure 3.6 Current distribution on the slot and microstrip line at different frequencies.	69
Figure 3.7 Effect of the length of the microstrip feed line on (a) input VSWR and (b) the real part of the input impedance.	70
Figure 3.8 Effect of the opening rate, R on (a) input VSWR, (b) the real and (c) imaginary parts of the input impedance.	71
Figure 3.9 Effect of the reactive impedance layer, W2 on (a) input VSWR, (b) the real and (c) imaginary parts of the input impedance.	73
Figure 3.10 Reflection phase of the reactive impedance layer structure.	74
Figure 3.11 Effect of the ground plane size (GND) on the radiation pattern.	75
Figure 3.12 Simulated and measured VSWR of the proposed antenna.	76
Figure 3.13 Prototype of the proposed conformal wideband antenna embedded in ballistic panels.	77
Figure 3.14 Simulated and measured VSWR of the proposed antenna.	77
Figure 3.15 Radiation patterns in (a) XZ- and (b) YZ-plane.	78
Figure 3.16 Measured and simulated gain of the antenna in dB scale.	79
Figure 4.1 Simulated one way through wall reflection and transmission through various building materials with a thickness of 6 inch.	83
Figure 4.2 Detailed block diagram of the developed UWB pulse radar.	85
Figure 4.3 Photograph of the developed UWB PD radar RF front-end module.	86
Figure 4.4 Link budget analysis of the radar transceiver.	87
Figure 4.5 Photograph of a top view and bottom view of the compact wideband Vivaldi antenna, with a size of 12cm by 9cm and a thickness of 31-mil.	89
Figure 4.6 Simulation and experimental VSWR result of the fabricated Vivaldi antenna.	90
Figure 4.7 Photograph of the fabricated Vivaldi sub-array.	91
Figure 4.8 Measured return loss of the Vivaldi sub-array, showing good match at 1 to 5.5 GHz.	91
Figure 4.9 Measured radiation pattern of the Vivaldi sub-array, showing good directional characteristics over the operation frequency.	92
Figure 4.10 Measured S_{21} (dB) of the 2 elements of the Vivaldi antenna, showing good S_{21} (dB) over the operation frequency.	93
Figure 4.11 Measured S_{21} (dB) of the 2 elements of conventional Vivaldi antenna depending on the location of a brick wall.	93
Figure 4.12 Vivaldi Antennas optimized with various walls.	94

Figure 4.13	Vivaldi Antennas optimized with various walls.....	95
Figure 4.14	Set up for measuring the received signal.....	97
Figure 4.15	Received signal comparison in various walls cases.	98
Figure 4.16	Radiation measurement setup adjacent to a cement wall.	99
Figure 4.17	Radiation measurement.	99
Figure 4.18	Measured Radiation Pattern through 3 inch brick wall.	101
Figure 4.19	Demonstration of collected pulses.....	104
Figure 4.20	(a) Experiment setup, (b) Localization with UWB system.	107
Figure 4.21	Demodulated thorax displacement of (a) subject 1, (b) subject 2.	108
Figure 4.22	Respiration and heart rate of (a) subject 1 using logarithm method, (b) subject 2 using logarithm method, (c) subject 2 using conventional method.	109
Figure 5.1	The low-profile spiral antennas above the EBG surface [1, 2].	112
Figure 5.2	Unit cell for AMC ground and a broadband dipole antenna above it [5].....	114

CHAPTER I

INTRODUCTION

There have been lots of activities to design and manufacture high performance, light weight antennas for use in a variety of portable wireless applications including satellite phones, military radios, handheld navigation, GPS tracking, recreational devices and laptop computers. Antennas can come in a range of plastic housings as well as embedded antennas. The embedded antennas are custom built to sit perfectly in the application's own housing.

Generally speaking embedded antennas are designed for:

Multiband functionality

For designers of portable and embedded systems, the evolution from single band/narrowband to multiband/wideband has been rapid, with antenna designers reporting demand for penta-band coverage in the cellular bands (850 MHz to 2 GHz). Designers too desire to miniaturize these components as well and definitely their antennas are not an exception.

Previously, the need was confined to a single band, and the push was to go to higher frequencies, but now the interest towards having both the low and high frequency bands as well. Figure 1.1 shows a 4 band embedded antenna. Design for these low frequencies is very challenging as they are electrically and physically small, but design objective still to have relatively high efficiency, good return loss, and high isolation.

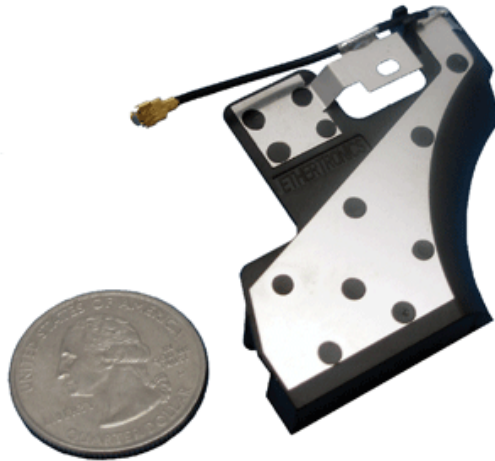


Figure 1.1 DriveCam product from Ethertronics is a custom quad-band embedded antenna that operates over the GSM 850, GSM 900, DSC and PCS bands for sending video data over the cellular network [1].

Efficiency

High efficiency translates into better signal reception i.e. S/N ratio, which reduces the number of dropped connections and improves the system's ability to support fast data transfer rates, and could be crucial for battery life for transceivers.

Bandwidth

Big concern for wide band signals, or for fast data rate to minimize distortion. Generally, achieving the efficiency and bandwidth for the internal media antenna in a small volume, along with lower power consumption are the main design concerns.

Return loss

Antennas are all designed to have a return loss of -10 dB or better, meaning that at least 90 percent of the electrical energy generated by the radio is transferred into electromagnetic wave energy, rather than being reflected back.

Isolation

It is an important parameter especially for multi antennas such as MIMO systems as selectivity of each of the antennas should be high to avoid crosstalk and interference.

Gain

Some applications would require certain gain/directivity or specific radiation pattern.

Others

Power handling capability is also a design concern as well as mechanical strength to stand impact. Furthermore, in case of operation in undercover vehicles, no external antennas are allowed.

Antennas are typically designed to operate in free space. However, antennas' performance could be significantly affected if embedded. The antenna designers should account for the effect of the package. In the following we will look into some examples of embedded antennas and the challenges in their design.

1.1. Examples of Embedded Antennas

1.1.1. Embedded Antennas in Concrete

Ref. [2] investigated the return loss, transmission loss, gain, and radiation patterns of a number of well-known antenna structures when embedded inside concrete. The study specifically focused on a bridge pier and led to envision that wireless sensors can be embedded inside it and still operate. Each wireless sensor will consist of a sensing element and a wireless transceiver to send and receive data. The sensor will be in a sleep/wake mode according to a defined schedule. To enable effective communication among buried sensors themselves as well like between a sensor and an outside base station we need to know how to design efficient communication antennas that can function inside concrete and steel reinforcements in the presence of variable quantities of moisture. We must also know the extent of the power loss such antennas will experience once embedded.

Pairs of buried dipoles, loops, microstrip patches, and planar inverted-F antennas were investigated while considering air-dried concrete, saturated concrete, and reinforced air-dried and saturated concrete. The study was used to show important guidelines for future embedded antenna designs. For example, it was found that both the planar inverted-F antenna and the microstrip patch will be good candidates for such applications. Although the loop antenna showed reasonably good performance it requires larger space compared to the other antenna types and will degrade in performance as more steel reinforcements are added. Similarly, the microstrip patch will also require larger space than the PIFA. As apparent, transmission loss for the PIFAs inside saturated concrete is around 45 to 48 dB.

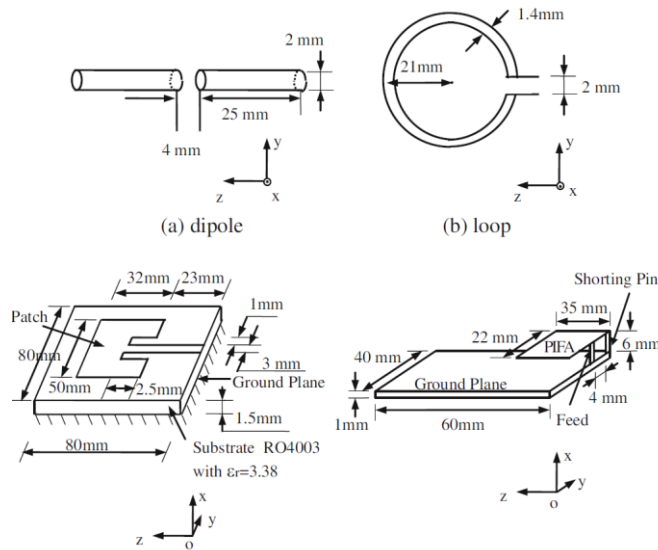


Figure 1.2 Geometrical dimensions of the antennas under consideration: (a) Dipole, (b) loop, (c) Microstrip patch, and (d) PIFA [2].

So it is clear from this study that the walls would affect the performance and should be accounted for, issues like antenna size too need to be considered. In any situation, link budget should shed some light on overall performance and the feasibility of securing adequate S/N ratio should be considered.

1.1.2. Implantable Microstrip Antennas for Medical Implants

Ref. [3] discussed that wireless communication techniques for air-to-air communication are improving and expanding at a phenomenal rate, but less for non-traditional wireless communication systems which include air-to-subsurface or subsurface-to-subsurface transmission paths where the antennas are “embedded” in lossy material. They point out that designing antennas for embedded applications is extremely

challenging because of reduced antenna efficiency, impact of the environment on the antenna, the need to reduce antenna size, and the very strong effect of multipath losses.

Additionally, there is a growing interest for Ultra-small devices (e.g., small enough to be injected into a human vein) and the desire to communicate with them, will inevitably lead to the need for miniaturized antennas embedded in lossy environments. Ref. [3] provides a better understanding of microstrip antennas embedded in lossy environments. The examples and sizes given were typical of those that could be used for a cardiac pacemaker or similar-sized implantable device, but the observations and trends can be scaled to smaller devices and higher frequencies as needed.

Embedded microstrip antennas have been also applied for numerous other sensory applications including sensors for dielectric property measurement [4, 5], sensing the presence of a dielectric object [6], moisture measurement [7], and geophysical well logging [8]–[10]. But in medical applications, embedded microstrip antennas have been used therapeutically for a number of applications including cardiac ablation [11, 12], balloon angioplasty [13], and cancer treatment using hyperthermia [13]–[17]. Designers of antennas for sensing or therapy need to address some of the difficult problems that degrade the performance of embedded antennas for communication - antennas are naturally sensitive to their environment (in consequence becoming good sensors), and inherently deposit large amounts of power in the near field of the antenna, particularly when it is embedded in lossy material, consequently becoming good therapeutic tools. These are advantages for sensing or therapy and disadvantages for communication applications. Inductive antennas (coils of wire around a dielectric or ferrite core) have been successfully adapted for biomedical telemetry, even if data rates are low, and

size/weight and biocompatibility issues limit the usage of the coil-wound devices. Ref. [3] evaluated microstrip configurations for potential use for communication with medical implant devices. Microstrip designs were chosen because of their huge flexibility in design, conformability, and shape. Methods to reduce the size of the antenna by adding ground pins [thus converting the antenna to a shaped planar inverted F antenna (PIFA)], using high dielectric substrate materials, and spiraling the conductor shape (planar helix) are applied. Both uniform and non-uniform superstrate materials were evaluated too.

Based on this research [3], several observations were made. Both spiral and serpentine designs were found to be effective radiators for communication with medical implants in the 402–405MHz MICS band. The spiral design was the smaller of the two designs and both were significantly smaller than a traditional rectangular patch. For optimal design, a biocompatible substrate and superstrate should have the largest possible ϵ_r , while having low conductivity, and thicker substrate and superstrate are better than thin. The best design can be found by first choosing the substrate and superstrate materials, then optimizing the length to provide approximately the correct resonant frequency. Finally, the antenna should be tuned by varying the location of the feed point with the ground point fixed very near one end of the antenna. The current distribution can then be observed, and an overall thinner design can be produced by using a superstrate that is thicker where the current density is high.

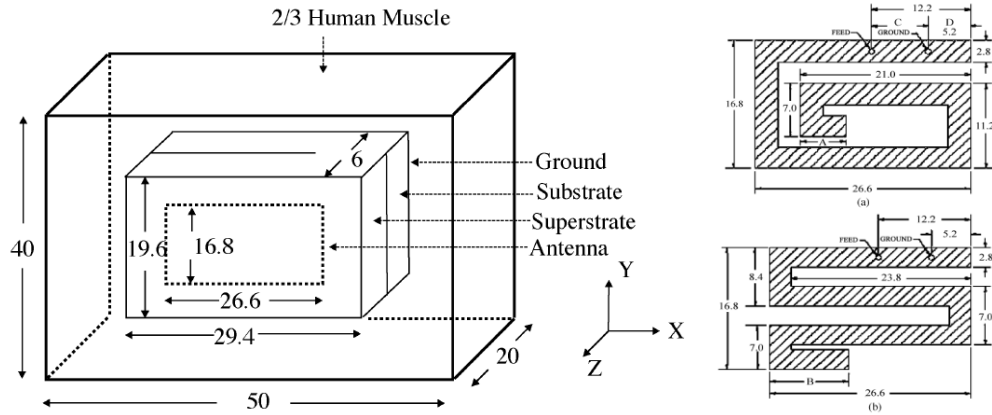


Figure 1.3 Simulation model (left), (a) spiral and (b) serpentine antennas (in mm scale) [3].

It is clear here that based on the application at hand, the design should be geared towards an optimum performance. Use of superstrate, the dielectric constant, the antenna type, emphasis in the near field radiation or far field, effect of surrounding environment on resonant frequency, possibility of communicating with the embedded antenna/system are prime design concerns.

1.1.3. Antenna Embedded in Low Permittivity Metamaterial

Metamaterials are structures composed of metallic or dielectric inserts embedded into a homogenous medium. If the size and spacing of the inserts are much smaller than the wavelength (usually less than one tenth of a free space wavelength), these materials can be homogenized and modeled with their macroscopic effective permittivity and permeability.

One of the most frequently used metamaterial is an array of parallel wires, a lattice constant of which is much smaller than the wavelength (see Figure 1.4) [18]. If the wires are parallel to the electric field vector of the incident electromagnetic wave, the effective permittivity exhibits well-known plasma-like behavior [19, 20]. Below the cut-off frequency (“plasma frequency”) of the wire array, the structure behaves as continuous material with negative permittivity. However, a very interesting application of thin-wire structure that operates slightly above its plasma frequency and therefore exhibits low positive permittivity has been proposed recently [21].

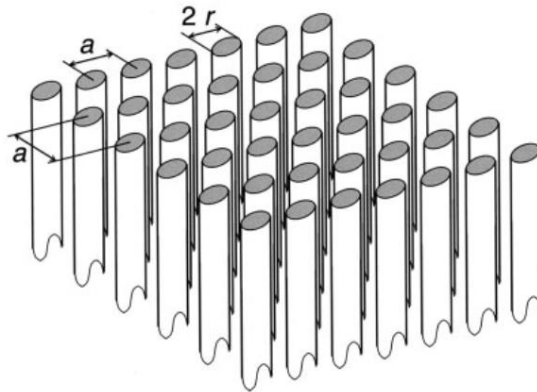


Figure 1.4 Wire-based metamaterial [18].

The above proposed application depends on the fact that if an electromagnetic wave emanated from an antenna is incident on a boundary between a metamaterial ($0 < \epsilon_r < 1$) and vacuum ($\epsilon_r = 1$), the refraction angle will be smaller than the incident angle. Since the relative permittivity of the metamaterial is very small but positive number, the refracted

beam will be almost perpendicular to the interface (ultra-refraction), yielding increasing directivity. Although the explanation is very intuitive and simple, it assumes an infinitely thick metamaterial slab. In practice, the metamaterial slab has finite thickness, which causes reflection from the second interface and possible excitation of leaky waves.

In a very recent theoretical study [22], it was shown that this mechanism of leaky waves is actually responsible for directivity increase phenomenon. The same paper gives several simplified equations for the directivity and bandwidth prediction.

In [18], a quarter wavelength monopole embedded in an anisotropic thin-wire metamaterial structure was investigated. The antenna and the metamaterial are designed for operation in 10 GHz frequency band. The influences of the number of wire-layers on the antenna directivity, gain, and input impedance were experimentally evaluated. This paper presented results to validate that the antenna directivity increase by using an anisotropic wire-based metamaterial. As expected, it was shown that this type of metamaterial also exhibits the effect of directivity increase similar to that previously observed when a 2D isotropic metamaterial was used. The obvious advantage of the anisotropic type of wire-based metamaterial is its much easier fabrication. The effect of splitting of the main beam that was theoretically predicted in previous studies has been confirmed too.

The influence of the number of wire-layers on the radiation patterns was also investigated and it was shown that there is an optimum number of layers for obtaining a maximum gain. It was also found that the presence of wires in the near-field of the antenna shifts the antenna input impedance locus to the inductive region of the Smith chart and closer to its edge with increased number of layers. This indicates that not only

the radiation properties but also the input impedance should be considered before practical applications of the metamaterial-embedded antennas.

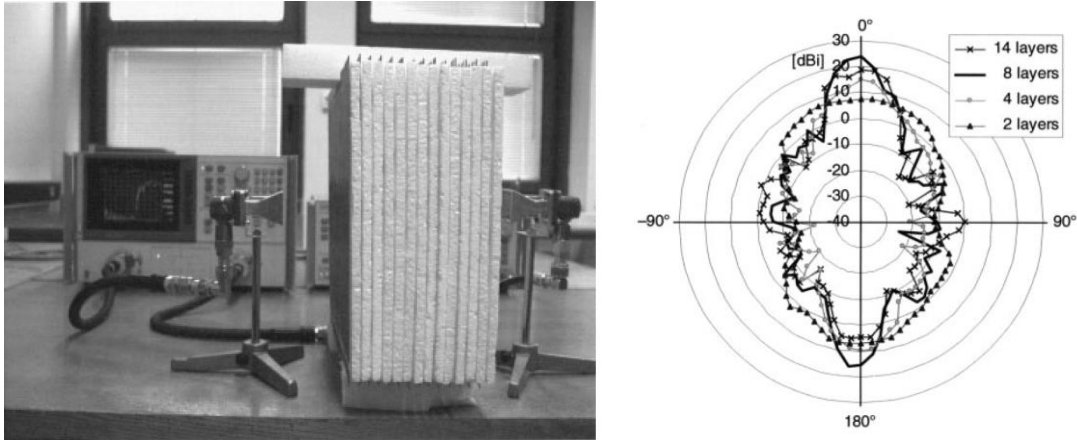


Figure 1.5 Measurement setup for metamaterial characterization and measured radiation pattern at 10GHz, number of wire layers as parameter [18].

So, use of metamaterial as part of the multi-layer antenna structure can significantly help in providing in-phase reflection. This is simply translated into higher directivity. There are different ways to implement this metamaterials, like the use of multi-layer wires which is simple and very promising.

1.1.4. Gain Enhanced of Embedded Microstrip Antennas

Ref. [23] showed that a microstrip antenna embedded inside a dielectric medium representing the building material monitoring coupled to a parasitic patch, placed outside the embedding material can increase the antenna gain significantly.

In addition, by properly selecting the antenna depth inside the embedded material its radiation characteristics can be made less sensitive to the material parameters of the surrounding. It was shown that for an embedded microstrip antenna placing an electromagnetically coupled patch, external to the embedding material improves its performance significantly. The gain maximizes when the depth of the fed patch is about half the wavelength, where the beamwidth also is equalized. The resulting antenna is an ideal candidate for interrogating an embedded wireless sensor.

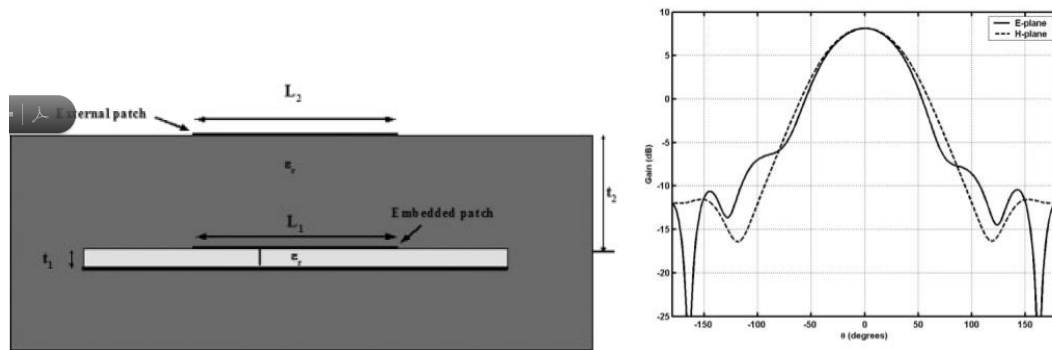


Figure 1.6 Geometry of electromagnetically coupled embedded microstrip antenna (left), E and H-plane radiation patterns near peak gain (right). [23]

So, even if the antenna is embedded, use of parasitic antennas can help in enhancing the performance. The parasitic element can be embedded as well within the layered structure or at the top of the package.

1.1.5. 2.4GHz printed antennas embedded in small UAV wings

Unmanned Aerial Vehicles (UAV) have been extensively used in exploration, surveillance and military applications. Such vehicles collect data via special sensors and send the data to the central station via wireless links.

The utilization of antenna arrays in UAVs has been present in literatures [25]–[27], none of them investigated the integration of such arrays as a part of the mechanical structure of the UAV or used any of the structural components as radiating elements. Printed antennas embedded in wing have been introduced in [24].

Utilizing the high gain (high directivity) of antenna arrays in the design of UAV structures is very attractive for several reasons.

- 1) Offer the UAV with higher data transmitting rates capability;
- 2) Antenna arrays extend the range of communication with the UAV;
- 3) Re-use of structural components as radiators can:
 - a. reduce weight: more flight time and smaller UAVs;
 - b. lower manufacturing costs;
 - c. make the system more robust by eliminating external components that can be damaged by the user or during take offs/landings;
 - d. internal structures reduce drag which provides longer flight times.

Several antenna elements were suggested to be integrated within the high altitude long endurance (HALE) UAV wing structure. Only helical antennas were realized while structurally integrated antennas like the printed Vivaldi were only simulated. The antennas were made for the L-band, and only wing surface antennas were considered. While in [28], a mechanical tracking mono-pulse radar was realized at the ground station

to track and enhance the directivity of the UAV-ground station link. This allowed for tracking ranges of 50–100 m. The antennas on the UAV were not altered, and no arrays were used. In [26], a broadband linear antenna array was used for the measurement of variations in the L-band (1.4 GHz) microwave emissions due to consumer electronics interference that can obscure the remote sensing of soil moisture in NASA missions.

The array of patch antennas was designed to be attached to the bottom of the body/wings of the UAV with a separate substrate thus adding to its total weight, also it has not been tested on a flying vehicle. While in [27], another L-band patch array was developed for the repeat-pass interferometric synthesis aperture radar (InSAR) instrument. A planar array was developed with 48 patch elements that were to be placed at the bottom of the UAV body structure with a radome height of 1.5 cm. Ref. [27] describes the simulation results of such an array and its importance in accurately mapping the crystal deformations associated with natural hazards. No hardware prototyping results were presented.

In [29], some key enabling technologies for antenna array implementations for SATCOM and UAV communications were illustrated. The use of UAVs in mobile ground terminal localization was discussed in [30]. A tracking technique for antenna arrays operating in the 2.4 GHz range for UAVs was discussed in [31] using commercially-off-the-shelf (COTS) electronics and an 8-element dipole array. The array was only simulated, and was designed to track the UAV within the ground station.

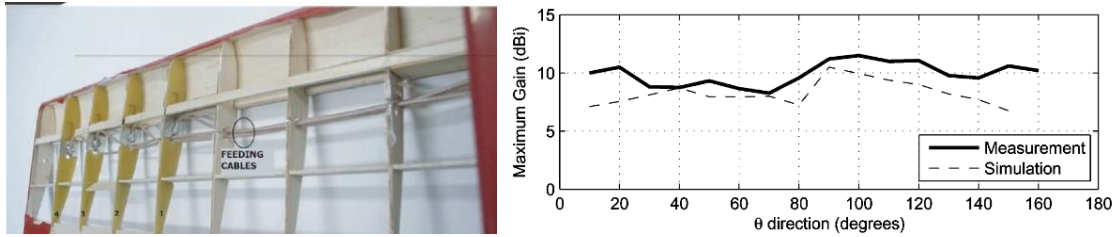


Figure 1.7 Prototyped antenna array within the wing structure (left), maximum array gain (right). [24]

The application at hand requires an extremely small element to be printed on the wing structural component because there is very limited space available for the feeding mechanism. Most of the antennas presented in the literature for operation in the 2.4 GHz band will not be suitable, either because of the size limitation or the feeding mechanism. However, what is fascinating *in this design is that it was built as part of the mechanical structure.*

To summarize what we have learned from the above discussion on embedded antennas:

- a) Embedded antennas could be part of the package*
- b) Embedded antennas could be designed taking the environment into account*
- c) Embedded antennas could be enhanced upon using parasitic elements that could be embedded too or placed on the surface.*
- d) Embedded antennas could be backed by metamaterial layers to provide in-phase reflection.*

e) *Embedded antennas could be designed for either near field to optimize sensing or treating, or for communication. So SAR and depth of penetration is important in the first, and the far field radiation and link budget are important for communication applications.*

1.2. Examples of Embedded Antennas

In this dissertation, we have investigated three examples for embedded antennas. The first example is for using a slot antenna for hyperthermia treatment. The antenna is designed to radiate into the tissue and the emphasis was in near field, SAR, and penetration depth. The antenna is embedded in soft substrate to maintain conformability and light weight. The antenna is backed by an absorbing material to prevent back radiation.

The second example is for an embedded antenna but this time the antenna is embedded in a very stiff substrate that can withstand very large mechanical impact/stress. The antenna should have positive gain over wide frequency range. Therefore, a metamaterial layer was used to provide an in-phase reflection thus enhancing its directivity and bandwidth.

The third example is UWB antennas designed to radiate through rubbles, walls, and debris. Typically, see through all antennas are designed in free space and within even a standoff distances. Here, we would like to investigate the feasibility of optimizing the design of the antennas for detecting vital signs of human beings hidden under the debris, similar to the antennas embedded in bridge structures.

Brief description of the outline of these three examples are given below, full details will be discussed in this dissertation.

1.2.1. Example I: Antenna for Hyperthermia Treatment

The embedded antenna within the hyperthermia applicator in this example has to be close to the tissue to have minimum possible return loss and transmits the highest amount of energy into the tissue. However, the close proximity of the antenna to the tissue would lead to significant detuning of the antenna operating frequency. This detuning can be explained by the fact that the human body has a high permittivity which represents a complex load to the antenna when located in its near-field and can detune the antenna from the system's frequency and influence its coupling and radiating characteristics.

The applicator should be suitable for various tissue loads while the system source should be less vulnerable to reflected power. Hence, we have been working on an applicator that has the tissue as an integral part of the antenna, i.e. is the antenna is directly attached to the skin. The radiating element should be embedded in a multilayer structure to provide conformability and to prevent back radiation. The developed antenna should operate at 434MHz and insensitive to tissue loading, and allow significant EM radiation deep penetration.

1.2.2. Example II: Embedded Antenna in Harsh Environment

To design a good-performance antenna in a harsh environment, it should be surrounded by a heavy material that stand any mechanical stress or impact. Several requirements still need to be satisfied including low profile, wideband radiation, low visibility, directional

radiation patterns, and positive gain characteristics. In addition, the interaction between the antenna and the covering/protective layers needs to be taken into account during the design stage.

Design of wideband antennas with low profile has been addressed before. For example, Zhou et al. [33] presented an antenna that operates in two modes at 470-706 MHz for digital video broadcasting-handheld (DVB-H) indoor application. H. Moon et al. [34] designed a very low profile wideband antenna composed of a flat grounded metallic plate with several ferrite bars placed between the plate and the ground plane at 30-300MHz. H. Nakano et al. [35] introduced a single-arm spiral (SAS) antenna. J. Oh et al. [36] designed and compared a low folded monopole antenna with capacitively coupled parasitic elements, and operates at 4-10 GHz.

In our effort, we will concentrate on developing a compact and wide band antenna that operates over 1-4 GHz frequency range for harsh environment applications.

1.2.3. Example III: Antennas for Vital Sign Detection through Debris and Rubbles

In developing a UWB antenna for see through walls or debris, we typically design it for free space operation. In this example, we investigated the feasibility of designing the antenna to radiate into the derris or walls directly. A good antenna candidate for portable UWB radar systems should have wideband, directional radiation pattern, and low phase distortion operation while being small size and low cost characteristics. There are different options to design such an antenna including stacked patches, microstrip slot [37], antipodal/tapered slot Vivaldi [39], coupled sectorial loops [40], elliptical-shaped dipole/monopole [41], and etc. Typically they are designed to operate in free space. Here, we

want to extend their design to radiate into wall and debris, i.e. in close proximity to a wall or embedded within debris. In our work here, we have extended our previous designs using exponential taper slot Vivaldi antenna that has been developed for our UWB radar prototype given its many advantages to radiate into lossy wall or debris, where the wall is an integral part of the antenna.

The developed antenna demonstrated ultra wide, low return loss, and typically radiates from a standoff distance, here we are investigating the possibility of redesigning the antenna in the presence of debris or wall materials. The antenna should have almost constant gain over the 1.5 GHz to 4.5 GHz frequency range.

To summarize again our work in this dissertation, we propose to survey available antenna designs in three areas and will show in detail the whole system design. For example, for the hyperthermia applicator we propose to survey available systems and applicator types, and then discuss various performance metrics for our proposed design. For vehicle mounted antennas operating in harsh environment, we discuss the role of the metamaterial layers in enhancing performance of the embedded antenna in multilayer structures. Finally, we discuss the vital sign detection through debris in detail, and as a demonstrating vehicle we propose to investigate the possibilities of detection of heart rates and respiration rates of victims covered with debris. The antenna design in this case, is optimized to improve S/N ratio upon reducing the significant energy reflection at the air/wall air/debris interfaces.

1.3. Challenges in Designing Embedded Antennas and systems

Although embedded antennas have gained a lot of attention and efforts by researcher, the available embedded antennas today still have their own limitations, when used for different surroundings. Most of the available antennas provide good impedance match to surrounds, but do not have a good gain and stable radiation pattern. In addition, embedded antennas operating at a narrow band work well for thin homogeneous and single media or through low-loss material.

It is a very challenging task to design good embedded antenna for inhomogeneous, multi-layer, and high-loss materials. A list of these challenges includes:

- (a) Develop a wideband, flexible, conformal, high directive antenna for hyperthermia treatment. A wide band width gives good match with various thickness of tissues. Also, flexibility provides uniform field distribution on curved body. Furthermore, high directivity toward a patient tissue prevents the unnecessary high field exposure to operators and improves the efficiency of the treatment as well.
- (b) Develop a robust antenna prototype with a composite panel as superstrate in order to operate well in a harsh environment.
- (c) Investigate and apply a reactive impedance surface (RIS) in order to enhance the gain, stabilize the radiation pattern, and remove the discontinuity in operating band as well.
- (d) Re-design and optimization of Vivaldi antennas with different walls in order to reduce the reflection from walls and improve the transmitting power through walls.

- (e) Accurate modeling and simulation
 - a. complicated tissue with high permittivity and high conductivity
 - b. ferrite material with high permeability and high tangential loss
 - c. composite panel with frequency dependent permittivity and tangential loss
- (f) Develop a new algorithm in order to improve the accuracy of estimating vital signs for UWB system in a very lossy environment.

1.4. Contributions in Designing Embedded Antennas and Systems

My major contributions include:

- Developed a flexible antenna at 434 MHz with wide bandwidth for hyperthermia treatment without using water bolus. It provides stable and uniform E-field, deep penetration depth, and minimum hot spots on skin with various tissue and body structure (skin, fat, muscle and bone).
- Developed a low profile antenna for harsh environments which achieves a wide bandwidth (1 to 4GHz) and maximizes the gain and unidirectional radiation pattern with applying a RIS and ferrite tile.
- Developed Vivaldi antennas re-optimized with various walls with less insertion loss through different walls than a conventional Vivaldi antenna designed in free space.
- Developed a new algorithm to improve conventional method for vital signs detection.

CHAPTER II

DEVELOPMENT OF A HIGH SAR CONFORMAL ANTENNA FOR HYPERTHERMIA TUMORS TREATMENT

Our first example for embedded antennas is the hyperthermia antenna. The investigated antenna is geared towards deeper penetration, and insensitivity to tissue loading. In the following sections we will overview hyperthermia treatment, basic metric parameters, followed by state of the art of various applicator antennas, and the challenges to design one.

2.1. Examples of Embedded Antennas

2.2.1 Hyperthermia Treatment

Hyperthermia treatment (HT) is a type of thermal therapy for cancer treatment that involves heating the target tissue (tumor) to 39°C-45°C for about 30 min - 1 hour, mostly as an adjuvant modality with the standard treatments such as radiation therapy and chemotherapy. The technology applied for low (39°C-41°C) and moderate (41°C-45°C) temperature HT is discussed in this chapter.

Thermal power can lead to cancer cell damage, usually with minimal injury to normal tissues. More important, for some types of cancer, heating the tumor can enhance the efficacy of radiation therapy and chemotherapy. The possibility of this enhancement has generated wide interest in developing equipment for conducting HT.

Figure 2.1 shows that the effect and usage of thermal energy on tissue at different temperatures. Here we are interested in low temperature and moderate temperature hyperthermia treatments.

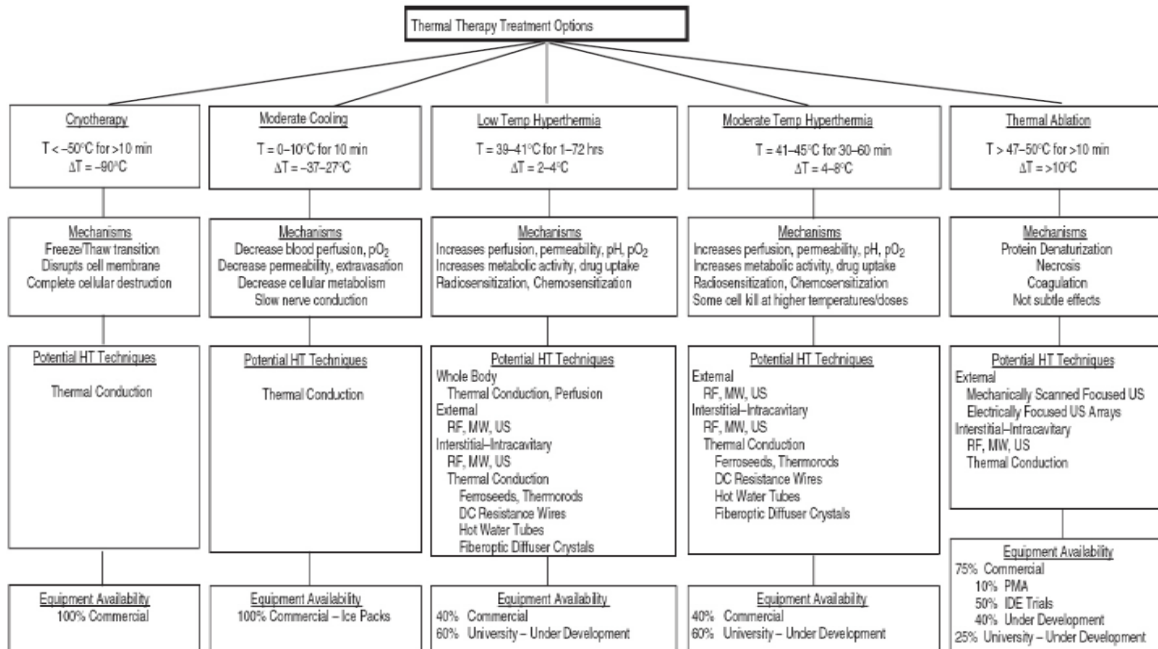


Figure 2.1 The effect and usage of thermal energy on tissues at different temperature. [1]

2.2. Hyperthermia Research by RF Engineers

2.2.1 IMS Frequency Band for Hyperthermia Treatment

Depending on the spectrum selection, hyperthermia applicators have exploited frequencies in various Industrial Scientific and Medical (ISM) frequency bands (or similar) at 7, 14, 27, 434, 915 and 2450MHz in Table 2.1. The longer wavelength of 434 MHz ($\lambda_0 = 0.690\text{m}$) has shown a more uniform specific absorption rate (SAR- refer to Appendix I for term definition) distribution and a greater penetration depth than 915 MHz ($\lambda_0 = 0.327\text{m}$) and 2450 MHz ($\lambda_0 = 0.122\text{m}$).

Table 2.1 IMS Frequency Band for hyperthermia treatment.

Center Frequency	BW (bandwidth)	λ (m) in air	λ (m) in muscle	Penetration Depth (m)	Hyperthermia Treatment
6.780MHz	30KHz	44.217	1.4552	0.26791	Popular in 1980s Capacitive coupling, Inductive Coupling. Regional, whole-body penetration depth \uparrow , coherence of the field \downarrow
13.560MHz	14KHz	22.109	0.99744	0.18732	
27.120MHz	326KHz	11.054	0.67286	0.13332	
40.680MHz	40KHz	7.3695	0.52822	0.11057	
433.92MHz	1.74MHz	0.69089	0.088174	0.051668	Small and light for applicators, shallow and adjustable thermal pattern, Waveguides, microstrip antenna and current sheets. superficial hyperthermia
915MHz	26MHz	0.32764	0.043577	0.0421	
2.45GHz	100MHz	0.12236	0.016731	0.02233	

In our work, we will use 434 MHz as our operating frequency. However, there are many other challenges that need to be addressed.

2.3. Properties of Tissues

Challenges of Antenna Design: To design an applicator, we should first know the Dielectric Properties of Tissues. The different water content of different body tissues determines the tissue dielectric properties, and consequently the RF energy absorption [2]. Due to the tissue water content, tissues are considered wet (skin and muscle) or dry (fat). The dielectric properties of a tissue are frequency dependent too which makes these problems difficult to analyze. Figure 2.2, 2.3, and 2.4 show the relative permittivity, the

conductivity, the penetration depth for skin, fat and muscle tissue in the range of frequency from 100 to 1000 MHz respectively.

It is shown that the permittivity decreases with frequency for the three tissues, while the fat presents a very low permittivity with little frequency dependence. Skin and muscle which contain water present greater permittivity values with a greater reduction rate at low frequencies. The conductivity increases with frequency and again it is shown that fat tissue presents the lowest values. The penetration depth, or skin depth, δ [m], is defined as the distance within a material at which the field reduces to $1/e^2$ (approximately 13.5%) of its value at the interface.

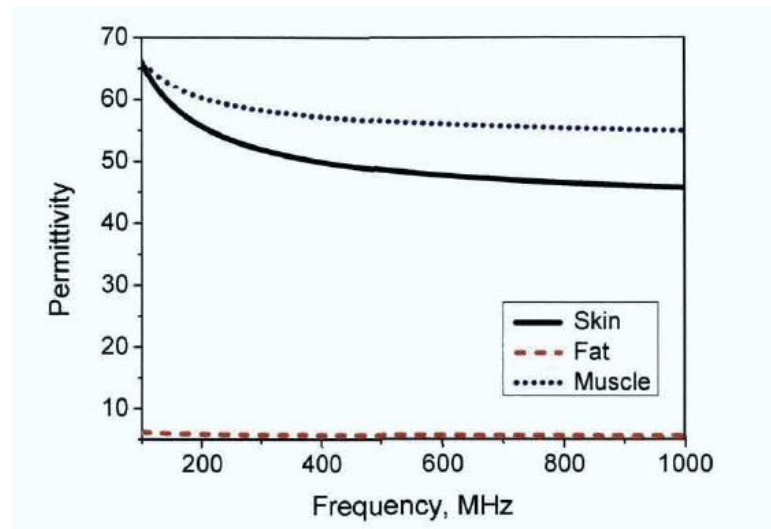


Figure 2.2 Permittivity of skin, fat, and muscle tissue.

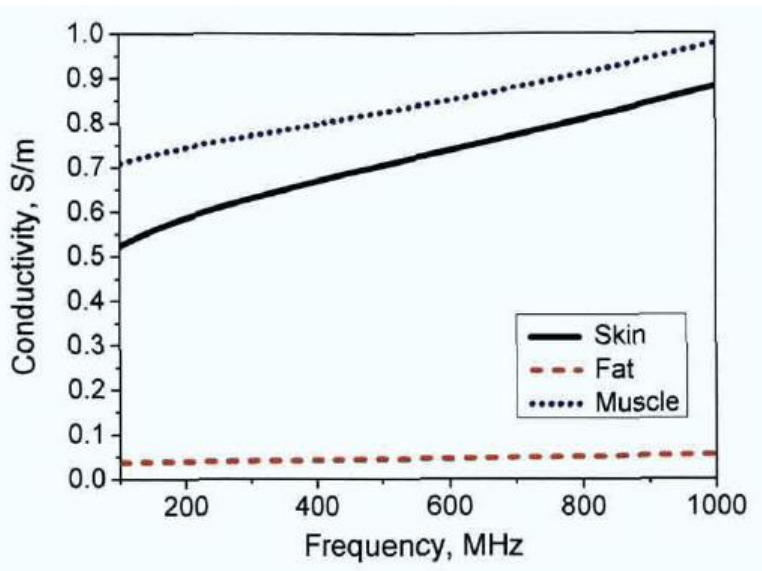


Figure 2.3 Conductivity of skin, fat and muscle tissue.

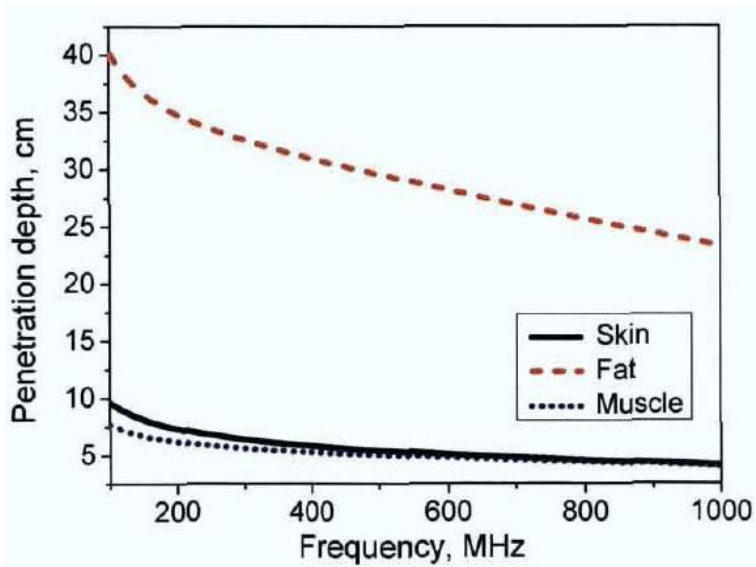


Figure 2.4 Penetration of skin, fat and muscle tissue.

Dielectric properties of human tissue may vary significantly among patients, tissue types and during treatment [3]. Normal and tumor tissues present different dielectric properties, and in general, tumor tissue presents greater conductivity and permittivity. As indicated in [4], for frequencies between 50 to 900 MHz the differences between normal and tumor tissue for kidney were around 6% and 4% for permittivity and conductivity respectively, while for mammary gland the differences were around 233% and 577%.

It is imperative to take into account the presence of tissue and the effect of tissue loading on these antennas to have proper radiation into tumors.

2.4. Hyperthermia Antenna Development

2.4.1. Hyperthermia Antenna Requirement

Distance related losses (DRL) and mismatch losses (ML) are two limitations that need to be considered when working with antennas for medical applications. The antenna has to be close to the tissue to have the minimum possible DRL and transmit the highest amount of energy into the tissue. In contrast, the antenna normally had to be far from the tissue to have minimum possible ML and detuning the antenna operating frequency [6]. The human body has a high permittivity complex load (different tissues of various dielectric properties) to an antenna when located in its near-field and can detune the antenna from the system frequency and interact with the coupling performance.

The applicator should be suitable for various tissue loads while the system source should be less vulnerable to reflected power. Conventional applicators show their

weakness of distance and various tissues dependent mismatching performance as will be clear from our survey studies given below.

2.4.2. State of Art

- **Waveguide Applicator Design**

An applicator using waveguide is one of the earliest examples of using thermal energy for therapeutic purposes [7]. The dominant E-field component of a rectangular waveguide is tangential to the surface, so the fat layer is not overheated. Waveguide is also used to carry very high power because of its strong mechanical structure [8]. In addition, many waveguide applicators are filled with water to decrease the size and reflection on the interface as seen in Figure 2.5 [9]. To enhance the Effective Field Size (EFS refer to Appendix I for term definition), an active slot antenna array fed by a waveguide was proposed by adjusting the amplitude and phase of each element [10]. In addition, a modified horn antenna applicator called the Lucite Cone Applicator (LCA) at 433MHz was proposed [11, 12]. The two walls parallel to the E-field of the LCA are made of Lucite instead of metal, and a PVS cone is inserted in the applicator as shown in Figure 2.6. This design has larger EFS than conventional horn antennas.



Figure 2.5 The water-filled applicator reduces reflection and provides variable surface cooling on the interface.

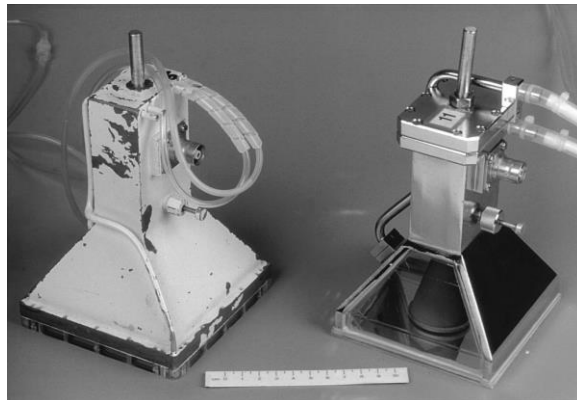


Figure 2.6 The conventional horn antenna applicator and the proposed Lucite Cone Applicator.

In [13], the authors proposed a modified water-loaded box-horn applicator. In Figure 2.8 (a), a box-horn applicator can provide a more uniform E-field at the aperture because both TE_{10} and TE_{30} are propagating modes. Moreover, the box-horn can be further modified to offer a bigger aperture for Surface Heating (SH) without decreasing the field

uniformity. A comprehensive analysis of the modified box-horn shows significantly better performance in array application than conventional horn antennas [14] and negligible mutual coupling between the box-horns [15].

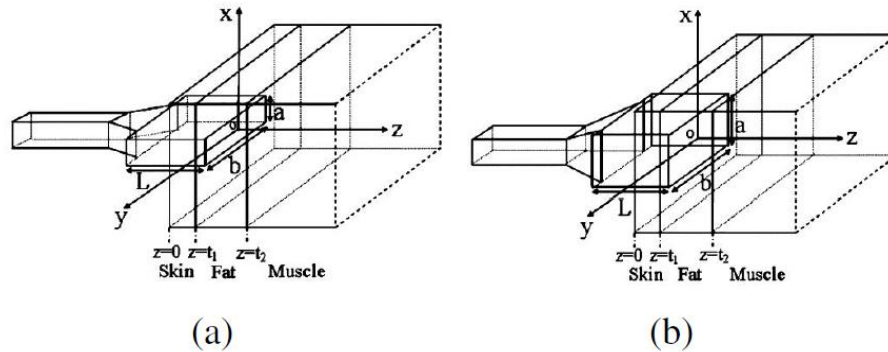


Figure 2.7 (a) The box-horn applicator with uniform E-field at the aperture, (b) The modified box-horn applicator with a larger aperture.

- **Microstrip Antenna Designs**

SH applicators using microstrip antennas have some advantages over waveguide applicators, such as smaller size, reduced weight and lower cost.

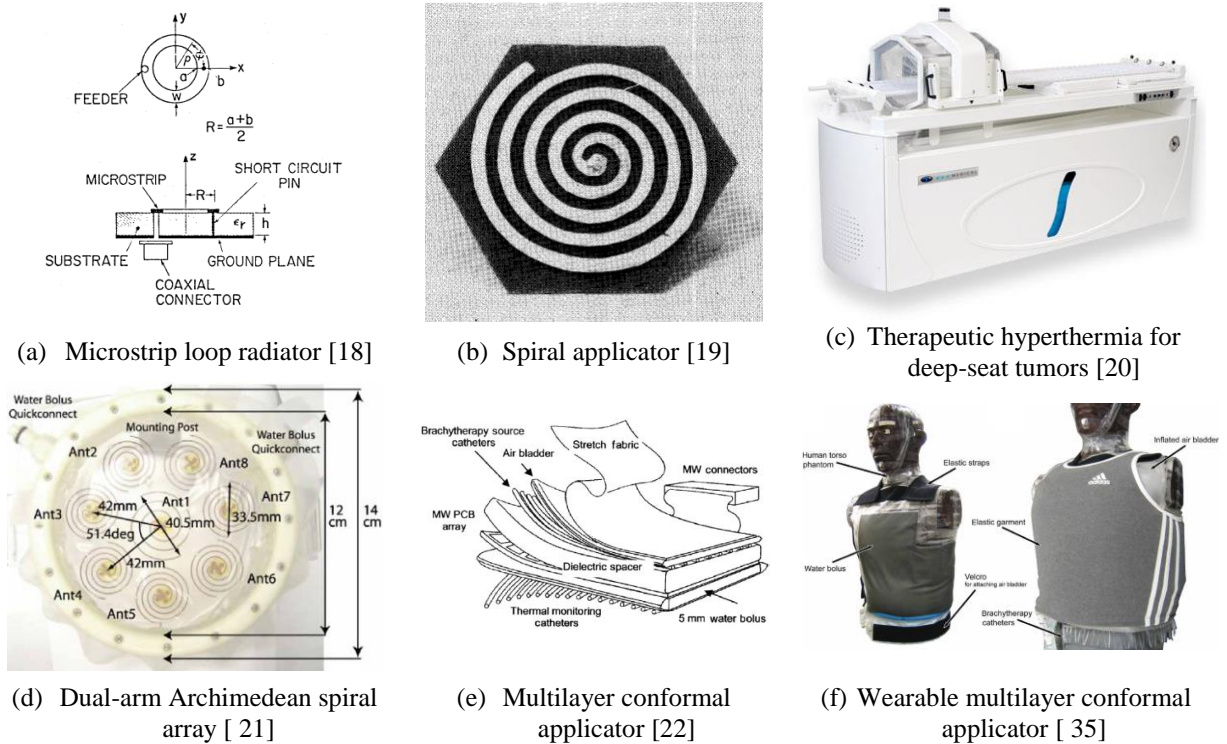
Firstly, the near-field is not symmetric for microstrip antennas and that causes non-uniform field distribution in Figure 2.8 (a) [18]. Secondly, because the resonance of the microstrip antennas occurs in the substrate, a significant difference in permittivity between the substrate and the water bolus results in a mismatch and poor efficiency in Figure 2.8 (b) [19]. Adding a superstrate layer above the antenna can improve the mismatch problem. Finally, a certain distance is required between the antenna and the

tissues (>3cm) because the near-field has a strong E-field component normal to the patient's skin. This problem can be solved by applying a thicker water bolus.

With respect to the different shapes of the microstrip antennas, the annular slot microstrip antenna has a smaller size, better transmission efficiency to the water bolus and a circularly symmetric SAR distribution compared to the rectangular microstrip antenna. If more than one frequency is considered in the same applicator, a microstrip spiral antenna provides broad bandwidth as the radiation mechanism is based on traveling waves.

The same concept has been applied to an array design [20]. The antenna sequential rotation extends and smoothes the heating pattern and the system operates at 400MHz instead of 915MHz for deeper penetration (3cm). The array using spiral antennas for SH is also commercialized in Figure 2.8 (c) [21], and Figure 2.8 (d) shows an array used in this evaluation. The evaluation shows that the applicator is able to cover a region up to 12cm in diameter and 2cm in depth. In addition, different shapes of heating patterns are also possible with this applicator.

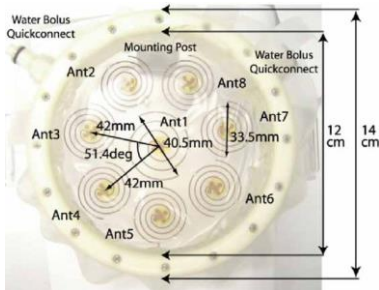
A multilayer conformal applicator was developed for SH treatment of recurrent breast cancer in the chest wall [22]. The applicator, as shown in Figure 2.8 (e) is able to administer a thermal and a radiation dose simultaneously. The air gaps between a patient's skin and the water bolus is always an issue that significantly affects the heating performance as the water bolus does not conform the body's shape well. In this design, the shape of the applicator is designed as a vest in Figure 2.8 (f). During treatment, the air bladder is inflated to significantly improve the contact, or reduce the air gaps, between the applicator and tissues.



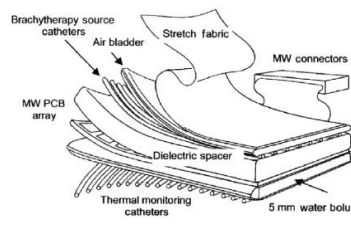
(a) Microstrip loop radiator [18]

(b) Spiral applicator [19]

(c) Therapeutic hyperthermia for deep-seat tumors [20]



(d) Dual-arm Archimedean spiral array [21]



(e) Multilayer conformal applicator [22]



(f) Wearable multilayer conformal applicator [35]

Figure 2.8 Various types of hyperthermia applicators.

- **Water Bolus**

A water bolus is common in most applicator designs. It is placed between the heating sources (coils, antennas, etc.) and the patient. The water bolus has multiple functions [23]:

- ✓ Reduce the reflection: the material properties of tissues are very different from that of air. The water bolus makes transmission of the EM field into the tissue with less reflection from the surface.

- ✓ Surface cooling: excessive superficial heating is a common problem in hyperthermia treatment. A water bolus with water circulated at a constant temperature can cool down the skin. Thus, the delivered power can be higher without burning the skin.
- ✓ Positioning: patient positioning is one of the important causes of uncertainty. The water bolus can be used as a fixture to anchor the patient to the applicator and thus reduce the uncertainty of patient positioning.
- ✓ Suppressing the emission: because of the great difference in permittivity between water and air, the water bolus can keep the leakage of the EM field at a safe level.

To address all of the above issues, we are interested in developing a new antenna that will demonstrate deep penetration depth, high SAR, large EFS, flexibility, and compactness of hyperthermia applicator without using water.

Table 2.2 Comparison of the performance of the different application at 434 MHz

Applicator Type	Dimension (mm)	SAR penetration depth (mm)	Reference
Dielectrically loaded waveguide	120×160	53.8*	[13]
Dielectrically loaded waveguide with water	28×56	33*	[14]
Flared horn aperture with dielectric inserts	100×100	36	[15]
Water loaded modified box-horn	90.3×125.5	40.1*	[16]
Microstrip shorted loop	R=20, H=3.2	28	[17]
Rectangular printed patch antenna on high $\epsilon_r = 80$	50×70×25	28	[18]
dipole-like radiator	150×160×5.5	14	[19]

*calculated

Table 2.3 Performance comparison of the different low profile applicators at 434MHz

Applicator Type	Description	SAR penetration depth (mm) for SAR > 0.5W/Kg
Wire loop [20]	Radius: 114.5 mm Width: 2 mm (full wavelength)	SAR < 0.5W/Kg*
Slot line [21]	Square slot line with dimension of 42 mm and width of 5 mm on a dielectric of 64 × 64 mm ²	15*
Circular Microstrip [22]	R= 19 mm on 78 × 78 mm ² with a dielectric with $\epsilon_r = 4$ and thickness of 1.5 mm	20*
Circular patch [23]	Circular patch surrounded by a concentric ring 130 mm × 130 mm × 2.97 mm, Taconic RF 35 ($\epsilon_r=3.5$), Two slots on the ground plane. Structure is fed by a coaxial feed placed on the annular ring	52.1*· ϕ
UT (this work)	microstrip-line-fed slot antenna with inserting a pair of metallic patches into the radiating slot on 100 × 150 × 4.7 or 9.8 mm ³ of multilayer	45 with a phantom (measured) 60*· ϕ

*calculated

ϕ : with 2.6 mm of Skin, 15 mm of Fat, 82.4 mm of Muscle

2.5. Antenna Design for Hyperthermia Applicator

The proposed antenna is a microstrip slot antenna, where patches are enclosed within the slot. It has a compact size, low cost, and easy to manufacture. The slot is fed by 50- Ω half wavelength meander-line. It provides most of the needed features such as high SAR, frequency detuning stability, and impedance matched at various distances from the body. This applicator is provided for the treatment of locally advanced superficial tumors in cats, dogs, and horses. Both the location and size of treated tumors are beyond the therapeutic range of hyperthermia modalities previously used in veterinary medicine. The antenna is designed to effectively radiate into the body not like conventional antennas that designed for free space radiation.

The developed conformal applicator addresses many of the weaknesses of traditional hyperthermia applicators. For example, the conformal nature of the applicator would allow for the treatment of irregularly contoured regions and the delivery of a more homogeneous electric field [6], [28]. The proximity of the conformal applicator to the tissue and its wideband properties effectively reduces voltage standing wave ratio seen with stand-off techniques (i.e. waveguides) and alleviates the necessity of a water bolus [4].

Electromagnetic simulation, electric field and SAR evaluation were performed using the CST Microwave Studio Suite 2012 software. Simulation results of the applicator are compared to those from similar size planar/flat microwave antenna and will be discussed in the following sections.

2.5.1. Hyperthermia Antenna Requirement

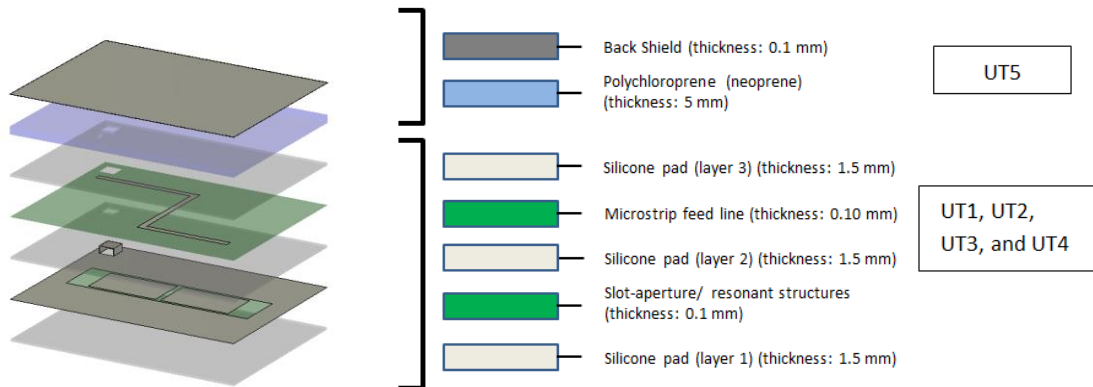


Figure 2.9 The multi-layer antenna structure. Four prototypes (UT1, UT2, UT3, and UT4) have a total thickness of 0.47 cm, while prototype UT5 has an additional back-shield and a neoprene layer and its total thickness is 0.98 cm

The geometry of the proposed slot antenna is shown in Figure 2.9. The antenna is comprised of two (RF-35P) very thin substrate layers of 0.10 mm with $\epsilon_r = 3.5$ and $\tan\delta = 0.0025$, one for printing the feed line and the other for printing the slot and resonant structure. These two RF-35P layers are inserted between three identical flexible silicone layers with $\epsilon_r = 3.8$, $\tan\delta = 0.004$, and thickness of 1.5 mm. The top flexible silicone pad is mounted on top of the antenna to not only prevent direct contact between the skin and slot structure, but also function as a buffer layer between the antenna and body to minimize reflections from the skin. The second silicone pad is inserted between the feed line layer and the slot structure. The third silicone layer is placed at the bottom and makes the antenna bend around the tissue easier, i.e. better conformability and flexibility. The parameters of the feed line, slot and two patches included within the slot are optimized for deeper penetration, insensitive match, and efficient radiation patterns. These parameters are indicated in Figure 2.10(a).

This multi-layer structure has overall dimensions of 11.0 cm \times 15.0 cm \times 0.47 cm (0.98 cm with a back-shield). All layers are flexible to allow for conformal application to the tissues.

A back-shield is utilized to prevent back radiation. It is made of fabric and has the same planar dimensions as the antenna (i.e. 11.0 cm \times 15.0 cm). A neoprene (Polychloroprene) layer is inserted between the antenna (UT5) and back-shield fabric to maintain a wide bandwidth. The distance from the top side of the antenna (facing the air side or the feed layer side) to the back-shield fabric is 5 mm; this gap is where the neoprene is inserted. In Figure 2.11, the effect of the distance between the antenna and

back-shield layer (i.e. neoprene thickness) is simulated in order to determine an optimal separation distance between the antenna and the shield.

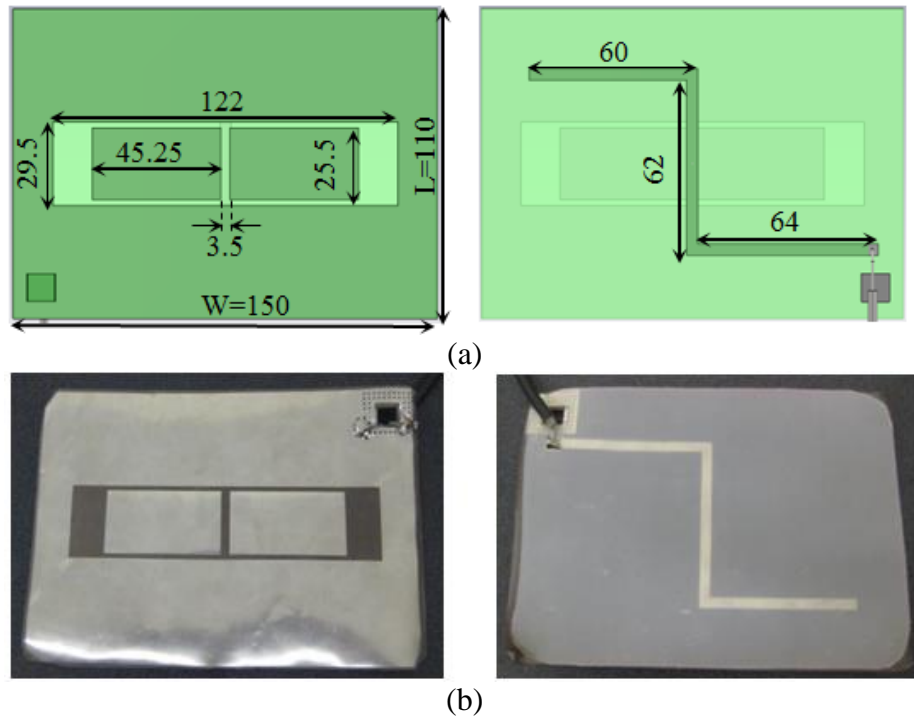


Figure 2.10 (a) Parameters of the proposed antenna in millimeter scale, (b) fabricated antenna.

Different from designing conventional antennas, this newly developed antenna was designed with the tissue loading accounted for. If the antenna radiates into free space, a very poor return loss will be seen; however if it is loaded with tissue, significant performance improvement will be noticed. The success of hyperthermia treatment lies in the focus of heat to within the cancerous tumor while avoiding the spread to surrounding normal tissues [29]. This will lead to a temperature increase during the hyperthermia

which is related to EM energy absorption in the tissue. This energy absorption is characterized by a specific absorption rate (SAR) parameter. The SAR value is related to the internal E-field [30]. This focusing of energy is generally characterized by other three parameters named: SAR penetration depth, effective field size (EFS), and effective heating depth (EHD) as measures of antenna efficiency.

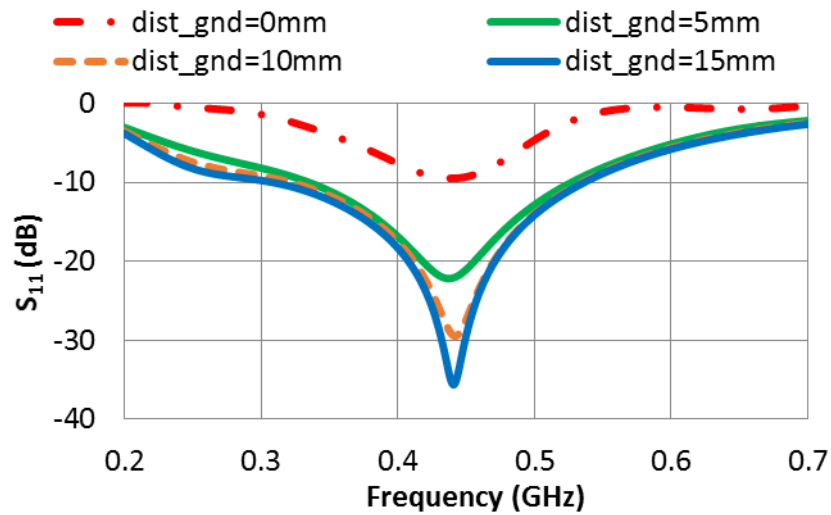


Figure 2.11 Simulated S_{11} for different distance between the antenna and back shield.

2.5.2. Microwave Hyperthermia Control Unit

A thermosensor is incorporated into the antenna to allow for monitoring and controlling the treatment. The block diagram is shown in Figure 2.12. The antenna is powered by a microwave transceiver operating at 434 MHz with a variable output power of 5-45 watts. The system can supply up to 60W of power to the proposed antenna, but a low or moderate power setting was selected in order to prevent skin burns and unwanted

damages to healthy tissues, as no water bolus is used. Typically, the maximum output power is set to 45W. Treatment time and surface temperature are defined by the user through a control board interface. Output power is then controlled automatically through a feedback from the antenna thermosensor; it is maximum at the beginning of tissue heating and reduces to near zero at temperatures at or above target temperature. In addition to this classic on-off control strategy, the output can be further modified by controlling the pulse repetition interval and/or pulse width based on feedback from the thermosensor. During initial heating, the interval can be shortened and/or the pulse width can be increased to speed up the acquisition of a given target temperature. Once a target temperature is reached, these values can then be adjusted to maintain constant surface temperature.

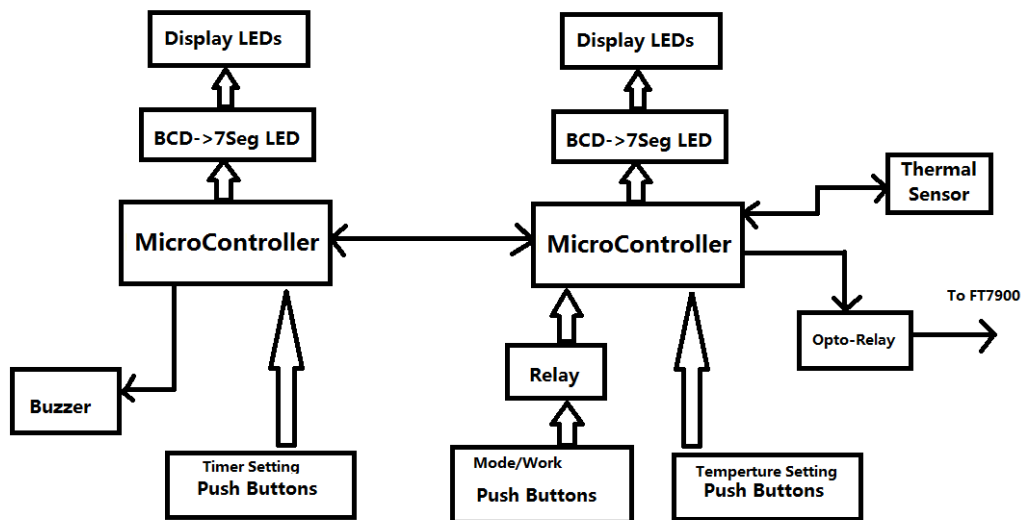


Figure 2.12 Control board block diagram.

It is imperative to mention here that the antenna gets mildly warm during the treatment, but in our setup a thermosensor controls the power amplifier and maintains a constant temperature. However, there is a slight variation in the dielectric constant, as indicated in [31] and [32] for example. Temperature dependent dielectric constant and conductivity values from 30°C to 50°C are approximately within $\pm 2\%$. To study this effect, simulations were carried out for a wider range of dielectric constants from $\epsilon_r = 52$ to 62. The S_{11} (dB) is shown in Figure. 2.13., where there is a slight frequency shift from the designed center frequency of 434 MHz. However, the result shows that a good return loss ($|S_{11}| > 10\text{dB}$) is still seen at 434 MHz since the designed antenna bandwidth is wide enough to tolerate such changes.

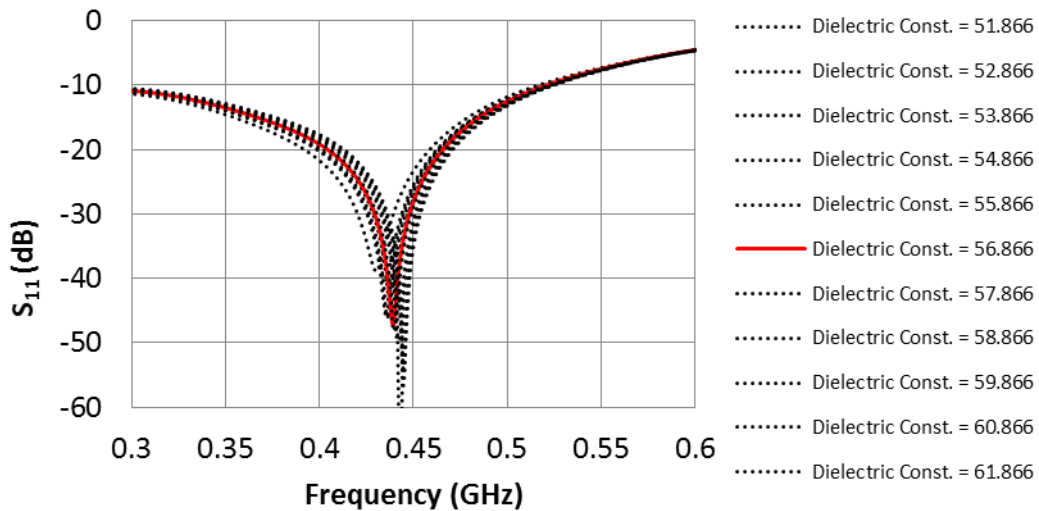


Figure 2.13 Simulated S_{11} with various dielectric constant of muscle.

In Figure 2.14., the time-temperature profile from a single 60-minutes treatment of a dog is shown. The profile at the surface and at about 4 cm deep within the tissue was measured. The actual temperature measurements are shown on the left axis, while cumulative equivalent minutes when the temperature at 4 cm depth reached 43°C (CEM43°C), are shown on the right axis. A thermal gradient of 3-4°C is seen between non-invasive and invasive temperature measurements, resulting in a significant difference between their CEM43°C. Typically, therapeutic temperature (>39°C) is reached in less than 10 minutes as determined by the surface and intra-tumoural measurements, as seen in Figure 2.14.

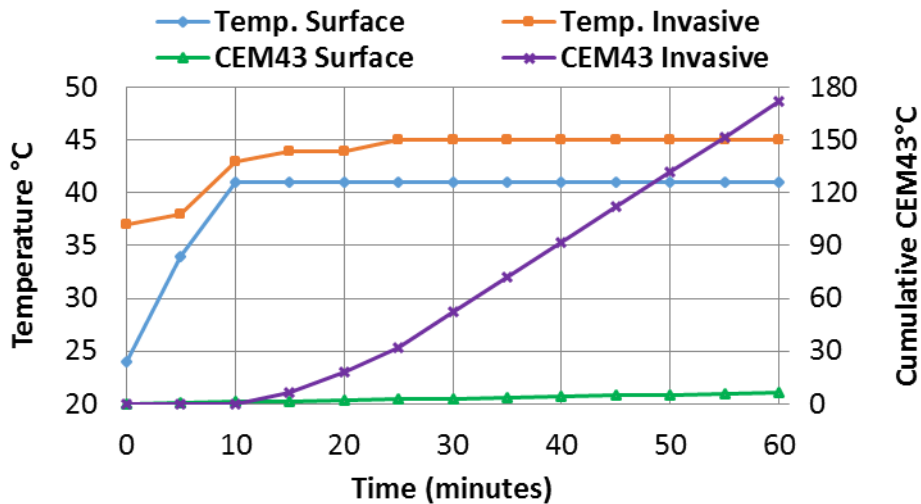


Figure 2.14 Time-temperature profile from a single 60-min treatment on a dog [33].

- Temperature surface= surface temperature measurements (± 0.5)°C;
- Temperature invasive = average intra-tumoural temperature measured along catheter track ~4 cm deep within tumor;
- CEM43 surface = cumulative equivalent minutes at 43°C as measured on the surface;
- CEM43 invasive = cumulative equivalent minutes at 43°C as measured intra-tumourally.

2.5.3. Phantom Tissue Model

The tissue dielectric parameters recommended by the IEEE SCC-34/SC-2 in P1528 [34] have been incorporated in this work. These parameters are derived from planar layer models simulating the highest expected SAR for the dielectric properties and tissue thickness variations in the human body. The complexity of the structure and composition of its biological materials are such that each region is broadened by multiple inhomogeneous constituents and its dielectric properties dispersion could be described by a Cole-Cole model representing its frequency dependence. In this case, parameters of the body tissue are derived from 4-Cole-Cole equations described in [35]. They are extrapolated according to the parameters specified in P1528 and the human inhomogeneous body. Derived electrical parameters of the tissue at the operating frequency of 434 MHz are given in Table 2.4.

Table 2.4 Electrical Parameters of Tissue Material at 434MHz.

	Permittivity (ϵ_r)	Conductivity (σ , S/m)	Density (ρ , Kg/m ³)
Tissue (FCC)	56.7	0.94	1000
Tissue (phantom)	56.636	0.934	1000

2.5.4. Methodology

Obviously, the main objectives for the hyperthermia antennas are the efficient radiation of power into the tissue. Our initial slot antenna geometry was designed to have a resonance with a single layer tissue model (UT1) and evolved to the slot antenna with

enclosed within patches and a back-shield (UT5). The penetration depth, EFS, and EHD were monitored upon adding the patches; the focusing effect was observed as a function of patch sizes in the simulation stage. The impedance matching between the antenna and the tissue, conformability, and uniform electrical near-field inside the tissue were also studied to measure the SAR response of four different antennas and the results are presented in the following section.

2.6. Antenna Design for Hyperthermia Applicator

2.6.1. Return Loss

Based on the simulation, it was concluded that VSWR performance at 434MHz is mainly determined by the length of the utilized meandered microstrip feed line and typically it is low over a wide band. Assuming the antenna loading would be equivalent to changing the electrical length of the feed line; as an example, the return loss of the UT3 antenna was calculated for different microstrip feed line lengths varying its length from 166 to 196 mm in steps of 10mm. As shown in Figure 2.16, all cases indicate adequate match at 434 MHz, which is a good indication of design insensitivity to detuning caused by tissue loading.

In order to optimize SAR, EFS, and the coupling between the microstrip feed line and the slot, UT5 was compared to other types of antennas as illustrated in Figure 2.18. Other parameters such as the number of patches and their sizes did not noticeably affect the antenna return loss performance at 434 MHz (<10 dB), as shown in Figure 2.17.

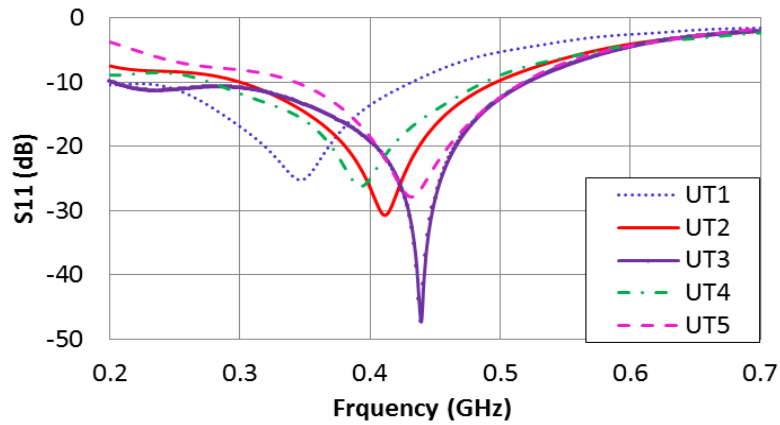


Figure 2.15 Simulated S_{11} for the slot antenna with different embedded patch sizes and numbers.

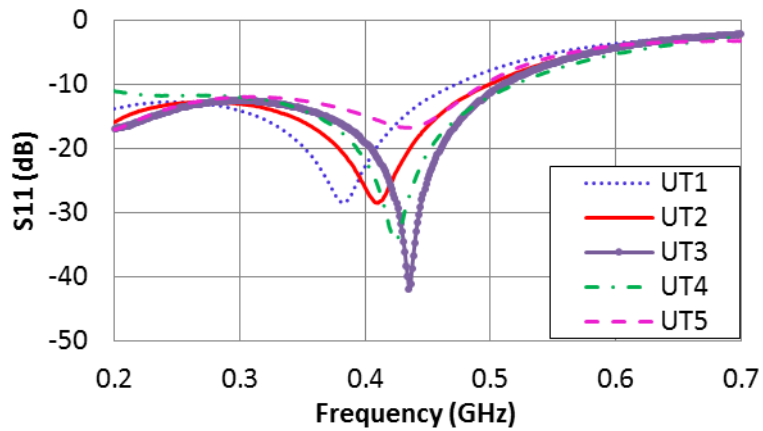


Figure 2.16 Measured S_{11} for the slot antenna with different embedded patch sizes and their number

To verify the validity of this simulation, a variety of species and tumor types were studied to illustrate the broad applicability of this technology. A horse, dog, and cat were used to measure the return loss (S_{11}) with an Agilent E8363B network analyzer. For

example, a measured return loss for the shoulder of a horse is shown in Figure 2.17 and was compared to the simulated return loss shown in Figure 2.16 (which uses a phantom).

Around the operating frequency, 434 MHz, the simulated S_{11} is in good agreement with measurement. The measured 10-dB bandwidth is around 300 MHz and the difference seen between the simulated and measured results is likely attributed to the difference in the assumed size of the surrounding tissues and that of the in-vivo measurements. Meanwhile, based on SAR measurements, the measured return losses of UT1 to UT5 were 29.2, 27.1, 31.9, 27.7 and 28.5 dB, respectively that are close to the simulated phantom and horse shoulder measured results.

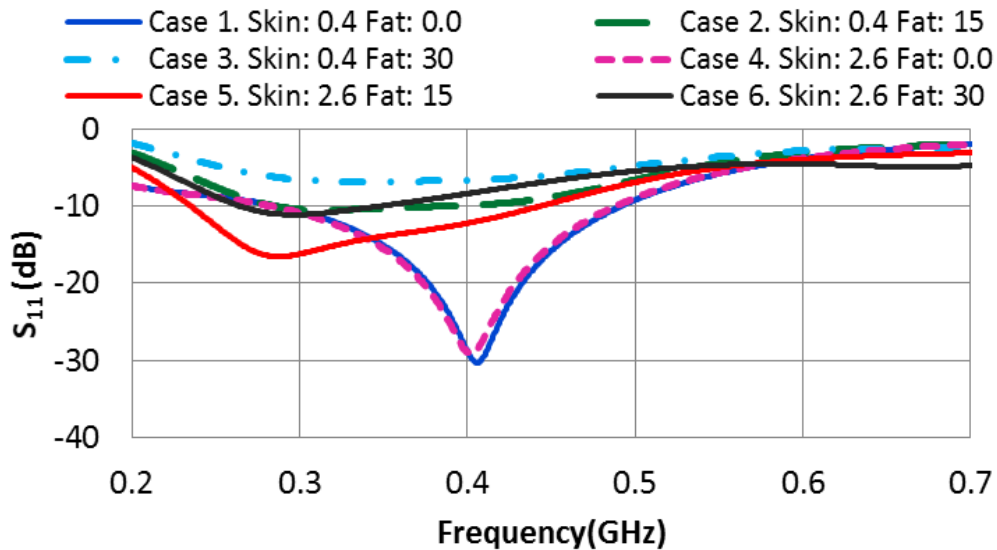


Figure 2.17 Simulated S_{11} for various multi-layered model.

To investigate the loading effect of multi-layer tissue on antenna performance, the simulations were carried out for different cases as seen in Figure 2.18. It is clearly visible that the performance is sensitive to the composition of the multi-layer model.

2.6.2. Electric Field Patterns

In Figures. 2.19-2.22, the illustrated results present the SAR measurements that were carried out to validate the modeling accuracy by comparing the measured and simulated results. The electric field patterns and the consequential specific absorption rate (SAR) patterns are functions of the patch sizes and their numbers enclosed within the slot of the ground plane.

Since the slot antenna is a bi-directional antenna, it is essential to eliminate or redirect the back radiation of the slot towards the patient. In our implementation, a back-shield at the top of the applicator prevents back radiation to the operator side. Its effect on the E-field was simulated as well. A two dimensional xz planes cuts for the near E-fields are shown in Figure 2.19. The near field provides information on the electric field intensity and distribution. The scale is clamped at 100 V/m for E-field plots for finer resolution illustration.

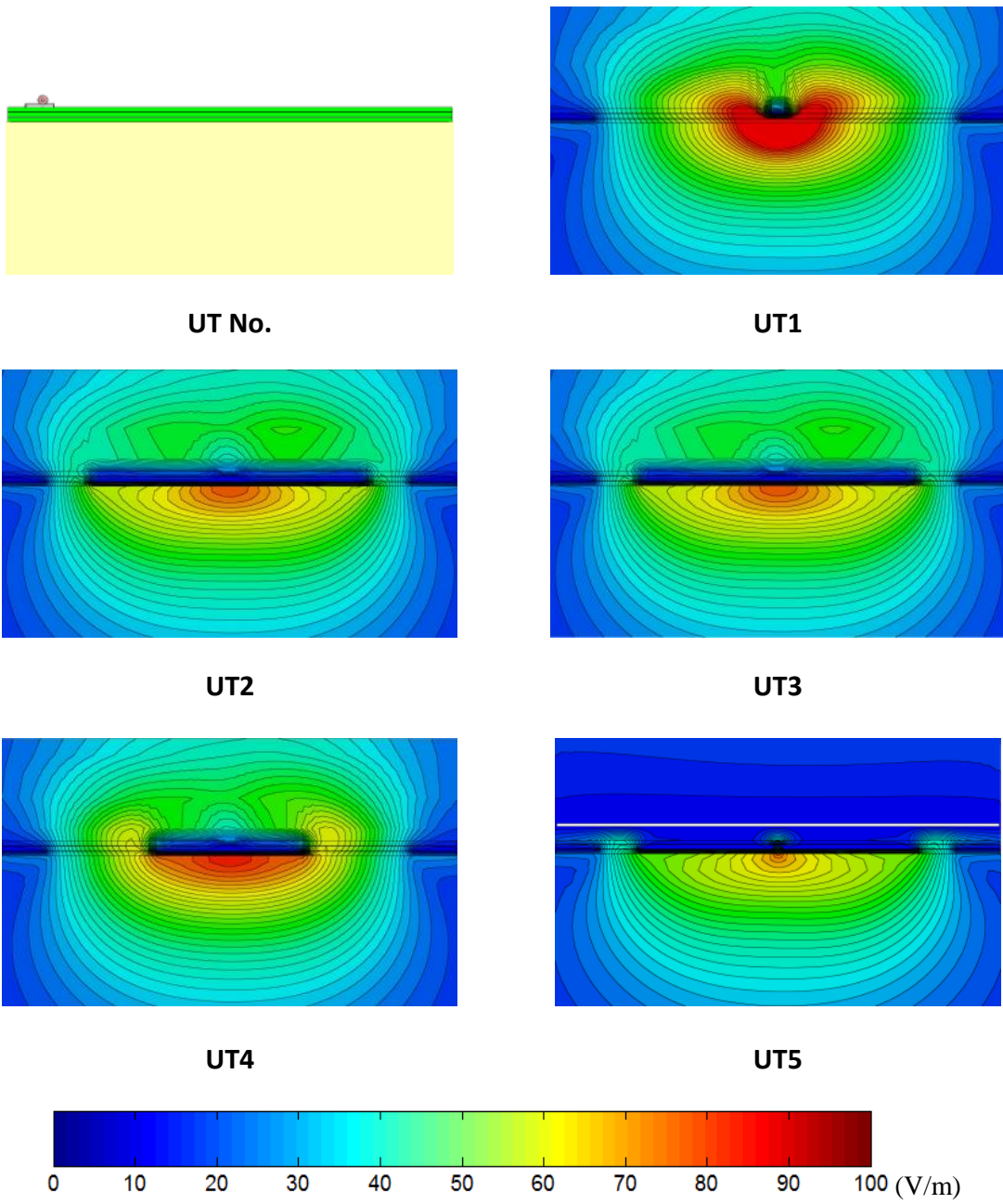


Figure 2.18 Tangential E-field distribution at the center of antennas.

2.6.3. SAR Patterns

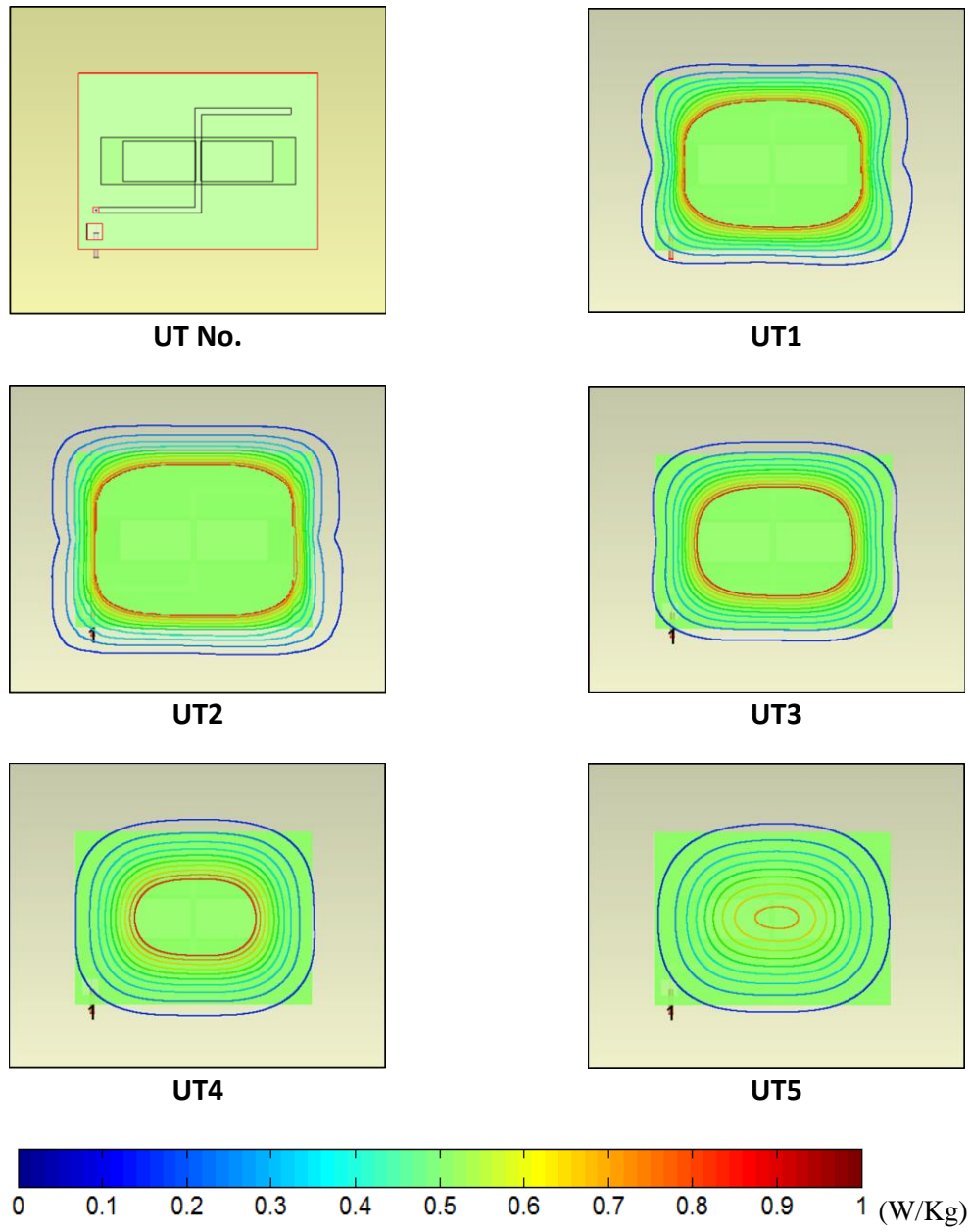


Figure 2.19 (a) Antenna geometry (UT5); SAR distribution for the antenna at (b) surface, (c) 1 cm, (d) 2 cm, (e) 3 cm, (f) 4 cm in depth.

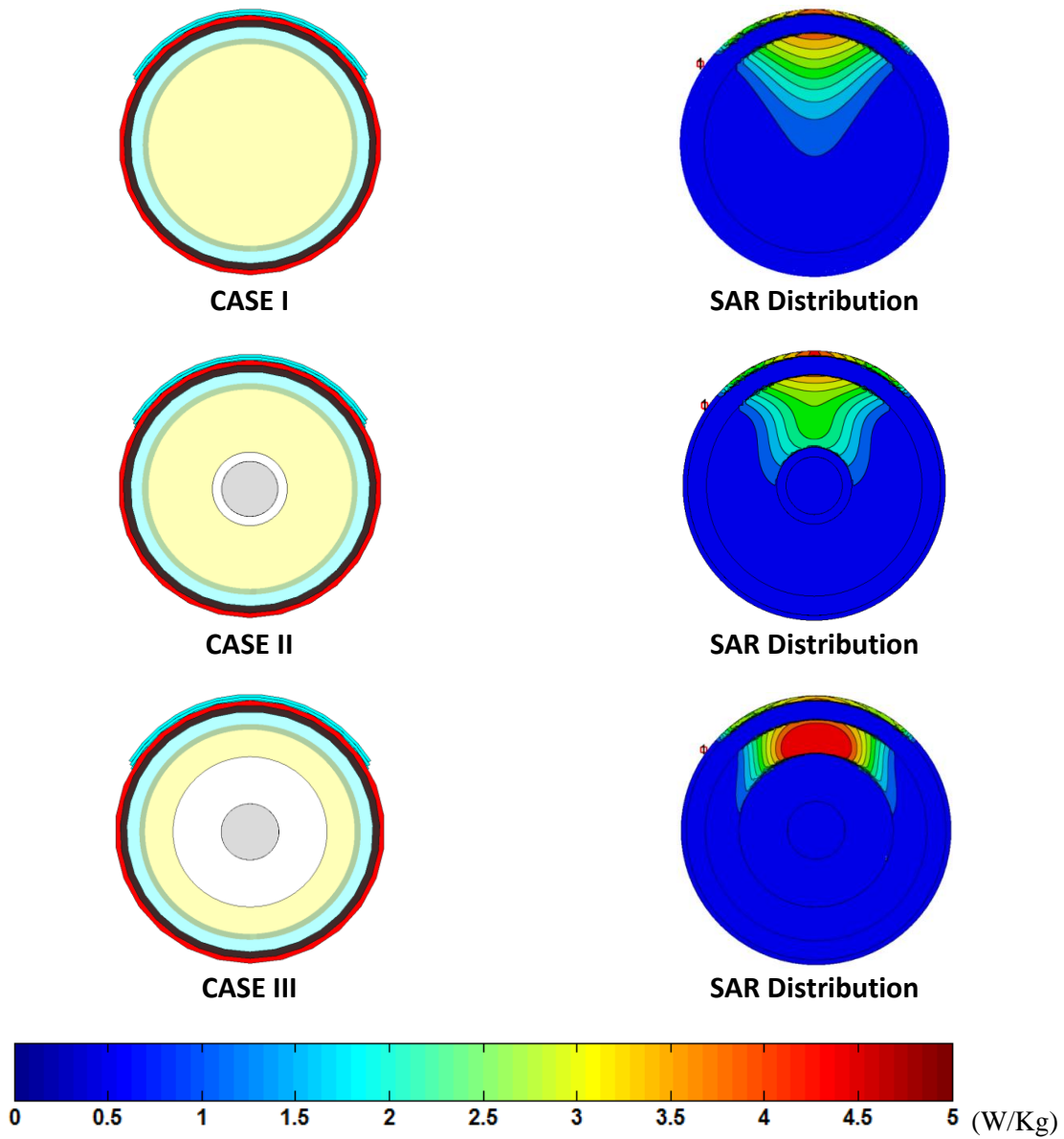


Figure 2.20 Simulated SAR with skin-fat-muscle-bone model.

Figure 2.20 shows a cross section plot of SAR distribution in the tissue at 434 MHz at different skin depth. For example, Figure 2.20(c) illustrates the normalized SAR contours

at 1 cm deep inside the tissue. For the proposed antenna, EFS is 75 cm². Figure 2.21 shows the SAR of UT5 with various curved surfaces. The SAR values in the tissue are normalized to an input power of 1 W and scaled from 0 to 1 W/Kg. It is clear that SAR distribution is uniform and centrally focused.

To study the effect of skin-fat-muscle-bone model, simulations are conducted with three different cases: case I with skin thickness of 2.6 mm, fat of 10 mm, and muscle of 57.4 mm; case II with skin thickness of 2.6 mm, fat of 10 mm, muscle of 37.4 mm, cortical bone of 5 mm, and marrow bone of 15 mm; and case III with skin of 2.6 mm, fat of 10 mm, muscle of 17.4 mm, cortical bone of 25 mm, and marrow bone of 15mm, as shown in Figure 2.21. The conductivity and dielectric constant of bone (cortical and marrow) is significantly lower than those of muscle. Obviously the SAR distribution changes with the composition of the model.

2.6.4. Effects of Patches within the Slot of the Conformal Antennas

This antenna design started with a planar slot antenna without patches. Typically, the presence of high SAR near the surface of the tissue can cause unwanted severe burns in the skin of tissue during the treatment. To reduce a high SAR in this region and increase the penetration depth as well, patches were placed in the slot to produce a better distribution.

The number and size of these patches have significantly affected the performance of the slot antenna. Figure 2.18 indicates that UT3 and UT5 have the optimum return loss performance.

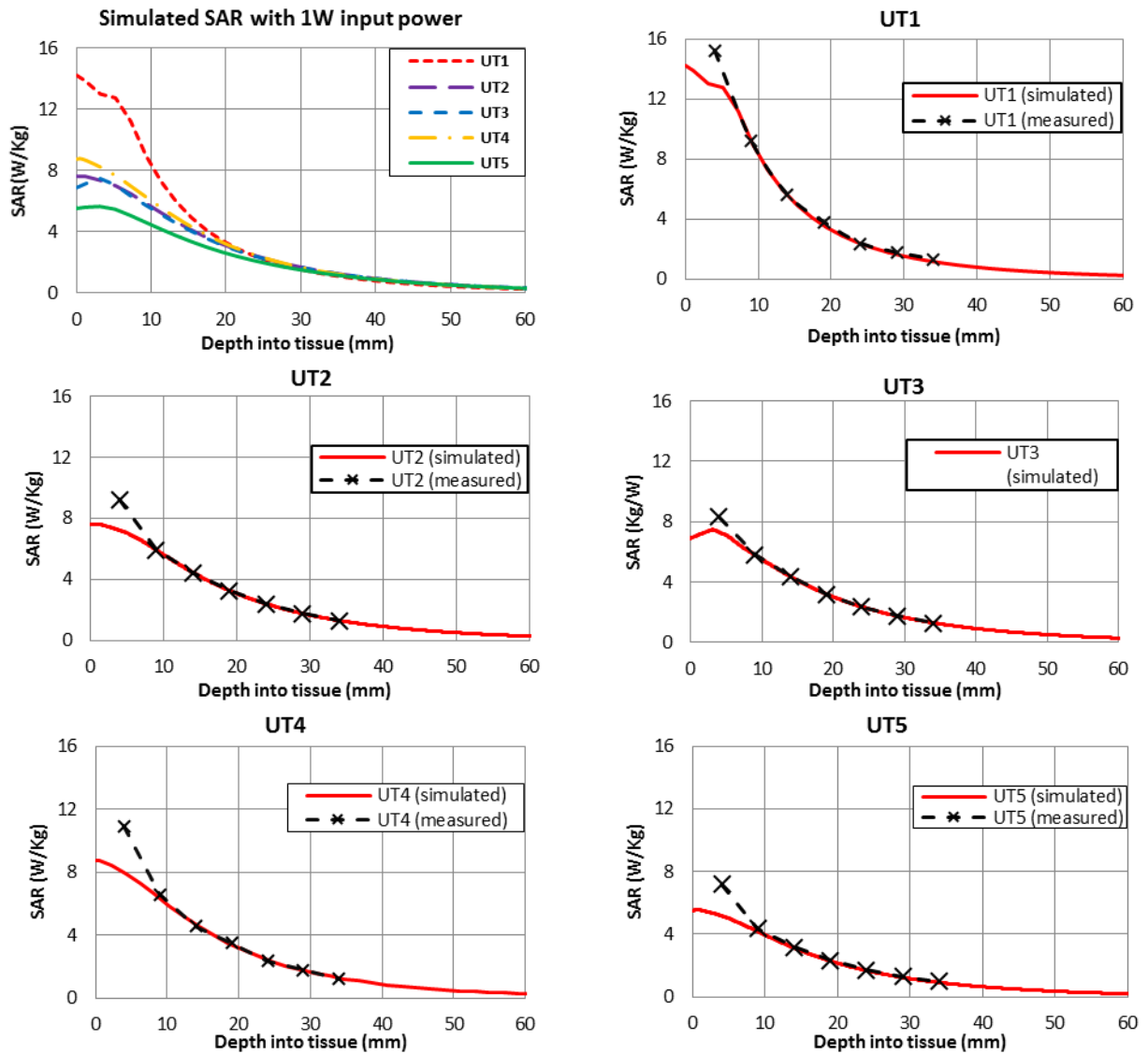


Figure 2.21 Simulated and measured SAR of the antennas.

In Figure 2.22, the measurements were performed to validate our simulations. The phantom is enclosed with a top with permittivity $\epsilon_r < 5$, loss tangent < 0.05 which is compliant with IEC 6229 and IEEE 1528, and has a 2 mm thickness [36]. The

measurement is consistent with the simulation except near the top of the phantom. The presence of the top would cause some discrepancy between the simulation and measurement in this case. Additionally, the presence of various tissue interfaces could create some hot spots; UT3 was utilized for some veterinary patients' treatments and some of these spots were noticed; further details can be seen at [33].

Table 2.5 Penetration Depth for Different Size of the Patches

Antenna	Patch size (mm) and number	PD (13.5%)
UT1	No patches	26.73mm
UT2	22.5 × 25.5, 2	39.91mm
UT3	45.25 × 25.5, 2	38.17mm
UT4	22.5 × 25.5, 2	34.70mm
UT5	45.25 × 25.5, 2	45.47mm

2.6.5. Effects of Body Curvature

SAR analysis of antennas mounted on curved structures was carried out, and the results are shown in Figure 2.23. The curvature radius was varied from 400mm to 30mm and two cases are shown in Figure 2.23. In Case I, a phantom model was used with 2.6 mm of skin, 15 mm of fat and the rest filled with muscle. In case II, the skin is kept to 2.6 mm, fat is increased to 2.5 mm and muscle layer appropriately decreased. As shown in Figure 2.24, it is clear that there is a definite drop in EFS (the area that is enclosed within the 50% SAR curve at 1 cm depth inside the muscle layer) with the radius reduction (i.e.

more curvature), and the EFS gradient has steeper slope for radii <100 mm for case I, and <50 mm for case II.

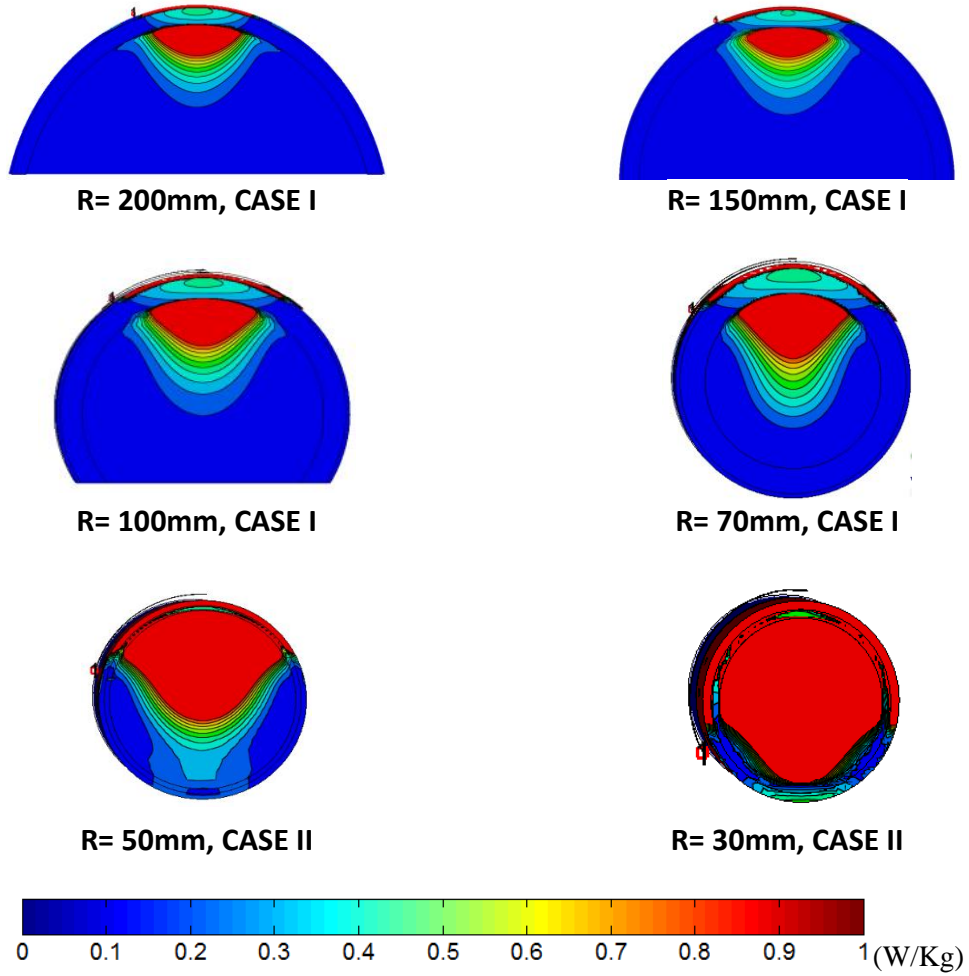


Figure 2.22 Simulated SAR with various curved body.

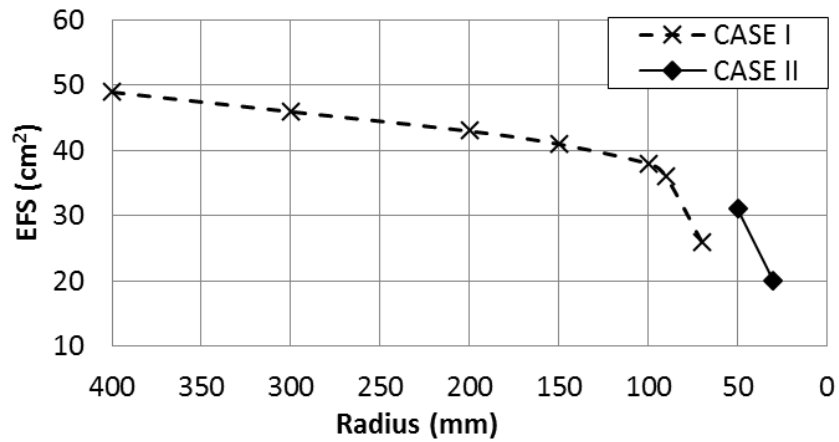


Figure 2.23 EFS defined with various curved surface.

2.7. Conclusion

The newly developed applicator provides compact, efficient, highly focused, deep-penetrating, and effective clinical hyperthermia for the palliative treatment of tumor bearing patients. The new compact slot antenna has been designed as an applicator for hyperthermia targeting veterinary patients. By using an antenna with flexible silicone pads and thin substrates that have been designed to radiate efficiently into the tissue instead of free space, this applicator can be mounted on a curved body and achieve a good match at 434 MHz with detuning insensitivity. This antenna structure has proved to be a good candidate to treat superficial skin cancer.

Simulation results indicate a favorable electric field distribution. This electric field pattern demonstrates the focusing ability of the antenna through its multi-layer structure. Simulation data was used to estimate the effective field size and effective heating depth as a measure of the overall antenna efficiency. Additionally, SAR penetration depth (>0.5

W/Kg) and EHD for the proposed antenna were simulated and measured and their values are 45 mm, and 20.8 mm, compared to measured 45 mm (extrapolated) and 20.9 mm, respectively. This is an excellent agreement between measured and simulated results. These SAR values are much better than wire loop, slot antenna, circular microstrip and patch applicators; but slightly lower than dielectrically loaded waveguide ones.

Moreover, the electric field patterns of this proposed applicator are superior to those obtained from a comparable planar microwave antenna. The applicator exhibits a reduced surface and backfield irradiation and improved directional irradiation along the z-axis compared to a planar slot-antenna. Similarly, the radiated power and depth of penetration of the applicator is notably increased to 5.16 cm (13.5% SAR) in comparison to 3.49 cm for the planar slot-antenna in case of mass averaged SAR (10g). During clinical applications, therapeutic temperatures were achieved at depths ≥ 4 cm. Tissue matching properties (i.e. S11 parameters) and bandwidth measurements were performed on cats, dogs, and horses. Excellent tissue matching properties were achieved with wide bandwidth of >300 MHz at better than 10 dB return loss.

CHAPTER III WIDEBAND EMBEDDED SLOT ANTENNA

3.1. Background

A Lately, there has been a large amount of research/efforts to develop wide band antennas that can be mounted on top (or on the side) of vehicles. These antennas should ideally have low profiles and typically are embedded between substrates and superstrates for protection. Therefore, these layers, however, might affect their performance. These antennas covers wide frequency range, occupy large real-estate, and should have positive gain, especially at the low frequency end; while demonstrating low visibility which makes it very challenging to design. In this chapter, we give a survey of such low profile antennas is given in the following section of Microstrip Slot Antenna, and we will state our proposed solution and their advantages. Numerical and Experimental results of the proposed antenna will be presented, the conclusion will be given at the end of this chapter.

3.1.1. Survey of Low Profile Antennas

Table 3.I list some examples of low profile antennas. The first example, is a novel low profile wideband antenna for digital video broadcasting-handheld (DVB-H) indoor application [5], shown in the first entry. The antenna can operate in two modes (circular patch antenna mode and microstrip mode), which leads to down-tilted beams when the antenna is mounted on a wall. The antenna prototype with a height of 46 mm has been constructed and tested. The simulated and measured results showed better than 2.0:1 VSWRs with shaped radiation beams in the DVB-H band (470-706 MHz).

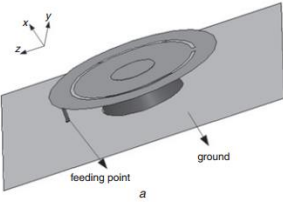
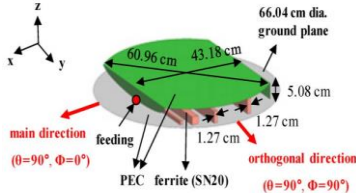

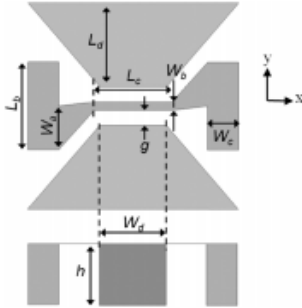
The second example, is a novel, very low-profile wideband antenna operating from 30 to 300 MHz [6], shown in the second entry. The maximum diameter and height of this antenna is only 60.96 cm and 5.08 cm, respectively. This design is composed of a huge grounded metallic plate placed 5.08 cm over a ground plane. Several ferrite bars strategically placed between the plate and ground plane play a critical role in improving the gain at low frequencies and pattern at high frequencies. Minimal number of ferrite rods was used to keep the antenna's weight relatively light.

A third example, is given in [7] where a single-arm spiral (SAS) antenna was developed, the structure also is listed in the third entry in Table I. First, the radiation pattern of the SAS having a disc/ground-plane was investigated. When the radius of the disc is smaller than the radius of the first-mode active region on the spiral and the spacing between the disc and spiral plane is small, the SAS was found to radiate a circularly polarized (CP) bidirectional beam, whose radiation pattern is almost symmetric with respect to the antenna axis normal to the spiral plane. Second, from a practical standpoint, the CP bidirectional beam is transformed into a CP unidirectional beam by placing a conducting cavity behind an SAS with a disc. It is demonstrated that the SAS has a good VSWR (less than 2) and a good axial ratio (less than 3 dB) over a design frequency range of 3 GHz to 10 GHz, where a cavity/antenna height of 7 mm (0.07 wavelength at the lowest design frequency) has been chosen. It was concluded that the SAS with a small disc backed by a cavity realizes a circularly polarized, low-profile, wideband antenna with a simple feed system that does not require a balun circuit.

Our fourth example, is a novel design approach manipulating the topology of a low profile folded monopole antenna with capacitively coupled parasitic elements in the same

plane that was presented to achieve an omnidirectional radiation pattern [8]. The 10-dB return loss fractional bandwidth of 43% was achieved with the dimension of $0.2 \lambda_{LF} \times 0.2 \lambda_{LF} \times 0.06 \lambda_{LF}$ where λ_{LF} is the wavelength at the lowest frequency of the operation. Unlike the conventional wideband $\lambda/4$ monopole antennas utilizing inductively coupled parasitic elements, the $\lambda/2$ folded monopole antenna allows for positioning the capacitively coupled parasitic elements in the middle of the antenna where maximum electric stored energy is formed. This, together with reducing the lateral dimension of the folded monopole antenna, enables the cancellation of radiated fields from electric currents in the horizontal plane of the proposed antenna, which is essential to achieve vertically polarized omnidirectional radiation. The compact parasitic elements introduce additional resonances that significantly increase the antenna bandwidth.

Table 3.1 Various Low Profile Antennas

Reference	Bandwidth (MHz)	Antenna	Dimension (cm)
S.-G. Zhou et al.	470-706		$45 \times 45 \times 4.6$
H. Moon et al.	30-300		$R=30.48$ $H=5.08$
H. Nakano et al.	3,000-10,000		$R=8$, $H=0.7$
J. Oh et al.	300-460		$0.2 \lambda \times 0.2 \lambda \times 0.06 \lambda$

3.1.2. Slot Antennas as a Viable Candidate

Along these lines, microstrip and microstrip slot antennas have attracted many researchers for a long time due to their low fabrication low profile and cost, thus they could be excellent candidate for such low profile applications. In general, microstrip slot antennas have wider impedance bandwidth relative to that of a microstrip patch antenna

and will be the focus of our effort here. However, the radiation pattern of the slot antenna is bi-directional, and it has similar radiation patterns in the front and back sides of the antenna, i.e. poor front to back ratio. This back radiation makes it difficult to mount a slot antenna on a metal ground plane, i.e. close to its backing metal ground plane, and this could diminish its gain.

3.2. Microstrip Slot Antennas

Microstrip lines fed printed slot antennas, especially the ones with wide slots, have received lots of attention. As they are applicable to satellite and communication applications, these antennas fit nicely our implementation. The advantages of slot antennas include:

- Low profile.
- Light weight.
- Easy integration with various circuits
- Stable radiation patterns so they are easy to mount and protect in a harsh environment.

For example, microstrip-line-fed printed wide-slot antenna with a fractal-shaped slot for bandwidth enhancement has been proposed and experimentally studied [9], it is shown in Fig. 3.1 (a). Experimental results indicate that the impedance bandwidth, defined by - 10 dB reflection coefficient, of the proposed fractal slot antenna can reach an operating bandwidth of 2.4 GHz at operating frequencies around 4 GHz, which is about

3.5 times that of a conventional microstrip-line-fed printed wide-slot antenna. It also has achieved a 2-dB gain bandwidth of at least 1.59 GHz.

The shape of the microstrip line feed affects the performance. A novel printed monopole antenna for UWB applications is presented in [10] and shown in Fig. 3.1 (b). The antenna is composed of wide slot and Y-shaped microstrip feed line with a pair of inverted L shaped notches. The relative impedance bandwidth is 110.6% and covers 3.09 GHz to 10.74 GHz.

A compact microstrip line-fed ultrawideband (UWB) tapered-shape slot antenna was developed [11] and shown in Fig. 3.1 (c). The antenna is comprised of a tapered-shape slot and rectangular tuning stub. The antenna is fabricated onto an inexpensive FR4 substrate with an overall dimension of $22 \times 24 \text{ mm}^2$. The experiment showed that the proposed antenna achieves good impedance match, constant gain, and stable radiation patterns over an operating bandwidth of 3-11.2 GHz (115.5%) that covers the entire UWB. The nearly stable radiation pattern with a maximum gain of 5.4 dBi makes the proposed antenna suitable for use in UWB communication applications.

However, the drawback of these slot antennas is their bi-directional radiation as previously mentioned. Ref. [12] in Fig. 3.1 (d) addressed this issue and developed unidirectional slot antennas with two different excitation methods, where unidirectional radiation characteristics are obtained by adding a reflector to the traditional bidirectional slot antennas. One excitation method is a microstrip line feed and the other is a coplanar waveguide feed. With the reflector, unidirectional patterns are obtained, with an impedance bandwidth of 110% and 120%, respectively for the two-excitation methods.

To reduce back radiation of the slot antennas, many designs have been investigated. For example, aperture coupled microstrip antennas have been utilized. Designs have been introduced to reduce the front to back ratio, F/B, and increase the bandwidth as well. In [1], for example, the utilized radiating patch was fed by a microstrip through a slot. In this case both the slot and the feed could be independently optimized for wide bandwidth operation, which could be sustained after integration.

It is the presence of this conducting ground plane that affects the overall radiation patterns, efforts are under way to invent new ways to replace such conducting layer (i.e. short circuit boundary) with out-of-phase reflection to an effective open boundary with in-phase reflection. Hence, ferrite materials or artificial magnetic conductors have been proposed but unfortunately have narrow bandwidth. To achieve even wider bandwidth performance, especially at the MHz range, a hybrid EBG/ferrite ground plane has been developed [2]. A wide operating bandwidth can be achieved too by utilizing an artificial magnetic ground plane backed by a ferrite layer. The use of the ferrite typically causes a significant degradation in the antenna's gain if it is very close to the radiating element. However, use of a relatively thick substrate would cause propagation of unwanted surface waves. Hence, the embedded AMC would be designed to present a reactive impedance surface in addition to providing in-phase reflection to minimize surface wave effects as well.

As shown in Fig. 3.1 (e), long slot antenna with a 41:1 bandwidth has been achieved starting at 120 MHz [13], where the ferrite is used as an absorbing layer at low frequencies, and the EBG provides a complete in-phase reflection at high frequencies.

However, the developed antenna gain was relatively low while the antenna cost and weight were high.

In [14], an antenna formed by the combination of a four-armed, reflective-backed spiral antenna with a top-feed quadrifilar helix, operating over the 0.35-2.6GHz band was developed. The antenna operated in Mode 1, its VSWR had less than 2.2, and was maintained throughout the frequency range. The nominal gain of 7 dBiC with excellent patterns characteristics was demonstrated, while the gain at f_o is 0 dBiC. However, the feeding network is very-complicated.

Subsequently, alternative methods have been introduced to address the weight, cost, and performance issues. Use of planar periodic metallic arrays to behave as artificial magnetic conductor (AMC) surfaces when placed on a grounded dielectric substrate is known to introduce a zero degree reflection phase shift to incident waves. AMC operation of single-layer arrays without vias or even stacks of these arrays are preferred to other structures like mushroom type AMCs [4]. Hence [3] utilized a 3D metamaterial broadband ground plane that was designed using genetic algorithms to enhance the performance, reduce the cost and weight of the EBG/ferrite long slot antennas.

However, none of the above antennas described above are suitable for harsh environment. An antenna under such condition requires additional layer(s) above the antenna for protection. This protective superstrate would distort important characteristics of the antenna such as radiation pattern, gain and bandwidth. Such embedded antennas need to be redesigned or optimized to account for such superstrates.

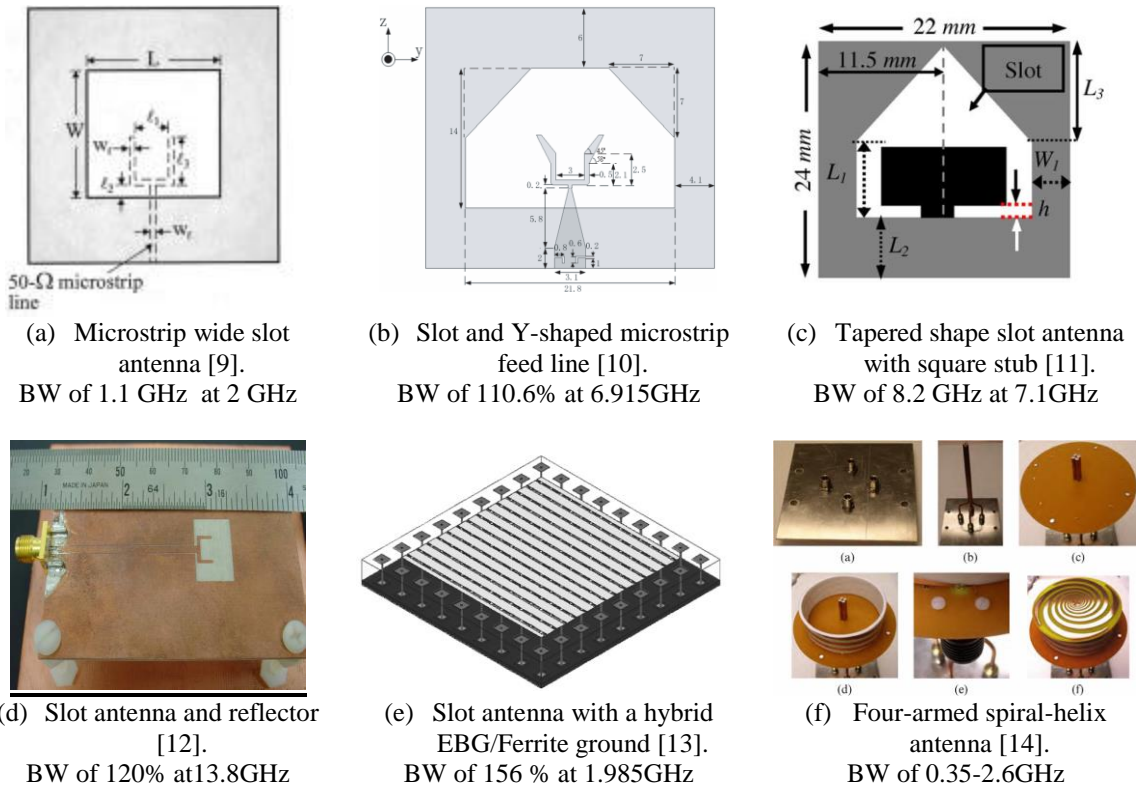


Figure 3.1 Various Antenna Structures.

Different materials can be used as substrates or superstrates, and we need to determine their dielectric properties. Due to their material properties, layers are considered to be either lossy or lossless. The dielectric properties of a material are frequency dependent too. Figure 3.3 and 3.4 show the relative permittivity, and the tangential loss for a panel that can stand harsh environment, measured from 1 to 8 GHz using dielectric probe measurements. It is shown that the permittivity varies with frequency for such a panel.

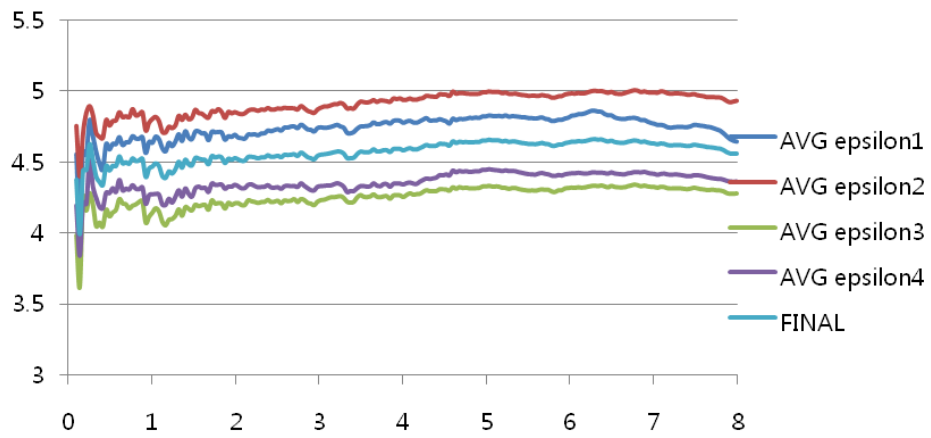


Figure 3.2 Permittivity of the composite panel with a thickness of 35mm.

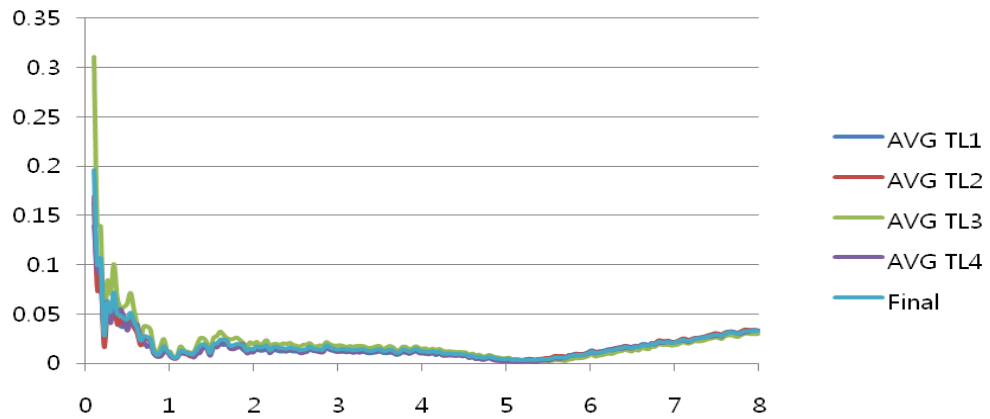


Figure 3.3 Loss tangent of the panel with a thickness of 35 mm.

3.3. Our Proposed Solution and their advantages

To get the bandwidth, a slot antenna is proposed shaped like an iron, fed by microstrip lines and backed by ferrite and metamaterial layers. However, for protection in a harsh environment, heavy duty panels are utilized as a superstrate. Their type and thickness depend on the protection level required for a given application.

The proposed slot antenna is a five-layer structure (as shown in Fig. 3.4) and it is comprised of:

1. A superstrate for protection,
2. A thin layer of double-sided FR4 for printing the antenna,
3. Another FR4 layer for printing a reactive impedance surface.
4. A composite dielectric layer
5. A ferrite layer backing the whole structure.

3.3.1. Antenna Structure

The tapered slot antenna is fed by a fork-shaped feeding structure to enhance the bandwidth of the antenna as reported in [9]. In [17], various tuning stubs and different slot shapes were investigated, and their antenna was comprised of a tapered-shape slot and a rectangular tuning stub. The proposed antenna combines the advantages of both structures. The proposed antenna gives an impedance bandwidth of 4:1, but offers a positive gain as well over the band. Both the tapered iron shaped slot antenna [15] and the reactive impedance layers are printed on FR4 substrate with each layer having a thickness of 1.57mm, $\epsilon_r = 4.4$ and $\tan \delta = 0.02$. The antenna is fed by a microstrip line

printed on the bottom side of the slot antenna layer. The combination of the high reactive impedance surface (RIS) and the ferrite layer is designed to emulate an effective magnetic wall to prevent: phase reversal, reduce sidelobe level, keep good impedance match over a wide frequency range and enhance the antenna gain as well [16].

In its design, we used an exponential taper profile that is defined by an opening rate R and two points $P_1(x_1, y_1)$ and $P_2(x_2, y_2)$ using Equation (1) [18].

$$y = c_1 e^{Rx} + c_2 \quad (1)$$

where

$$c_1 = \frac{y_2 - y_1}{e^{Rx_2} - e^{Rx_1}}$$

$$c_2 = \frac{y_1 e^{Rx_2} - y_2 e^{Rx_1}}{e^{Rx_2} - e^{Rx_1}}$$

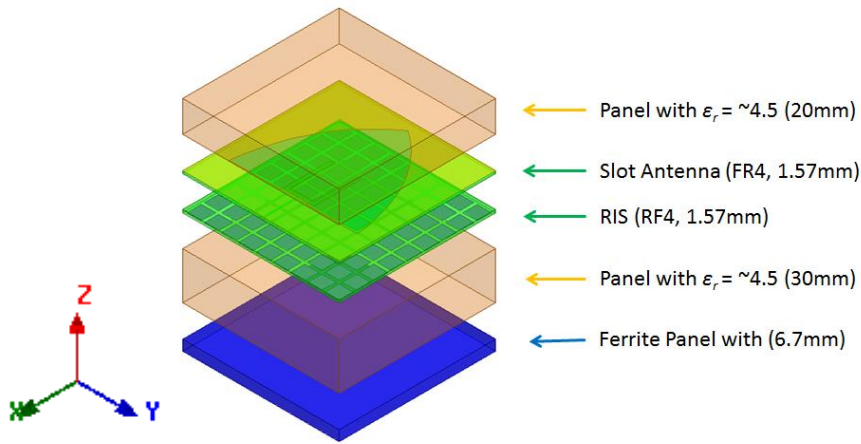


Figure 3.4 The proposed multi-layer antenna structure.

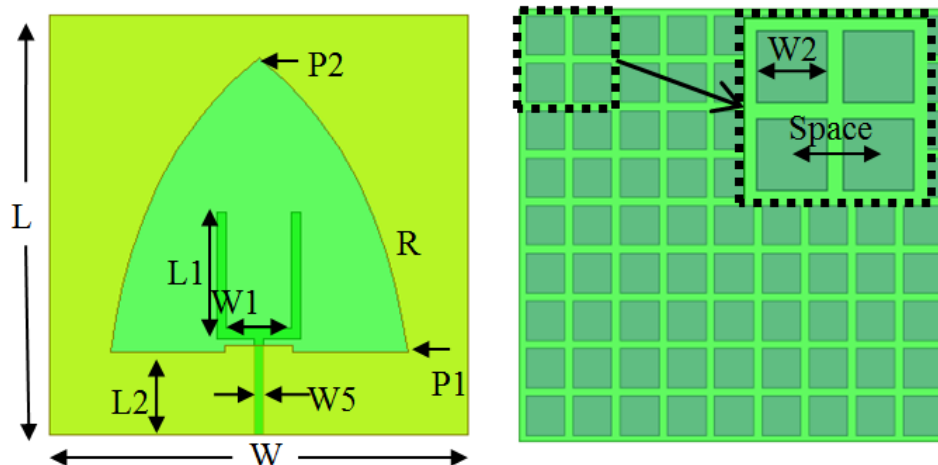


Figure 3.5 Parameters of the proposed antenna after optimization. $L = 100$, $W = 100$, $W50 = 2.2$, $W1 = 15.4$, $W2 = 5.5$, $L = 100$, $L1 = 30$, $L2 = 19.8$, $R = 0.3$, $Space = 10.5$ in mm scale.

The current distributions on the antenna at four different frequencies simulated with HFSS14 are shown in Fig. 3.6. It indicates that at low frequencies, the surface current density is high on the slot as shown in Fig. 3.6 (a). The edge of the iron shape slot controls the radiation at lower frequencies. This is expected because operation of the antenna is attributed to the slot at low frequencies. As the frequency increases, the current density on the slot relatively decreases, and a substantial increase in the current flow is noticed near the fork shaped tuning stub. Hence, at higher frequencies, the radiation is mainly due to the microstrip feed line and the fork. The impedance match is adjusted by tweaking the feed line parameters.

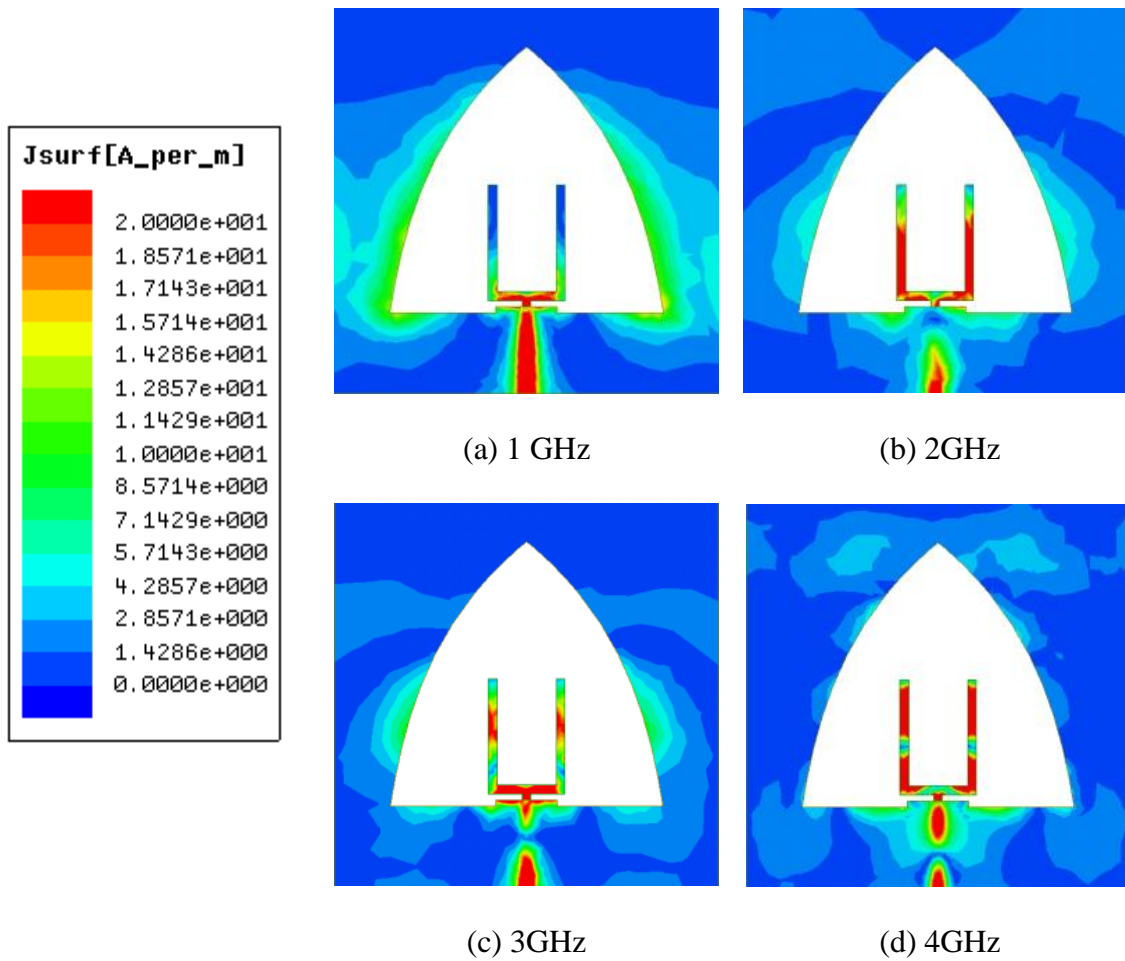


Figure 3.6 Current distribution on the slot and microstrip line at different frequencies.

3.3.2. Parametric Study

A parametric study was carried out to investigate the design sensitivity to the length of the fork shaped microstrip feed line L_1 , the opening rate of the antenna R , and the size

of the reactive impedance surface, W_2 . Parameters were selected to reduce such sensitivity.

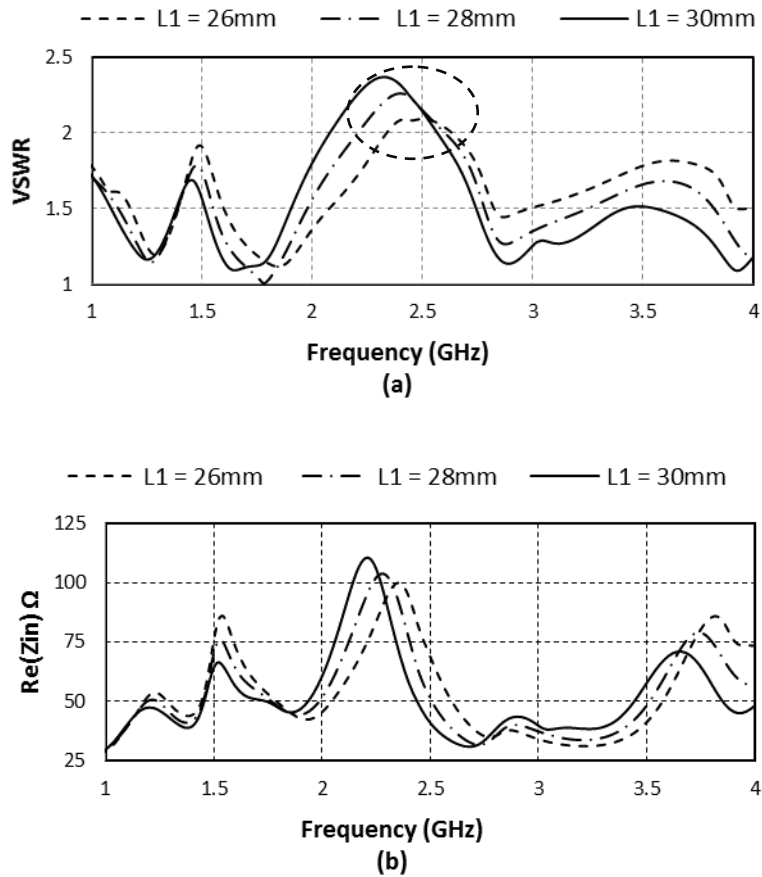


Figure 3.7 Effect of the length of the microstrip feed line on (a) input VSWR and (b) the real part of the input impedance.

The first parameter is the length of the fork shaped microstrip feed line, L_1 . The feed line length L_1 has an inductive effect on the input impedance which affects the resonance frequency. Increasing L_1 results in slightly extending the operating range to lower frequencies as shown in Figure 3.7 (a) and (b), but deteriorates performance in the center of the band.

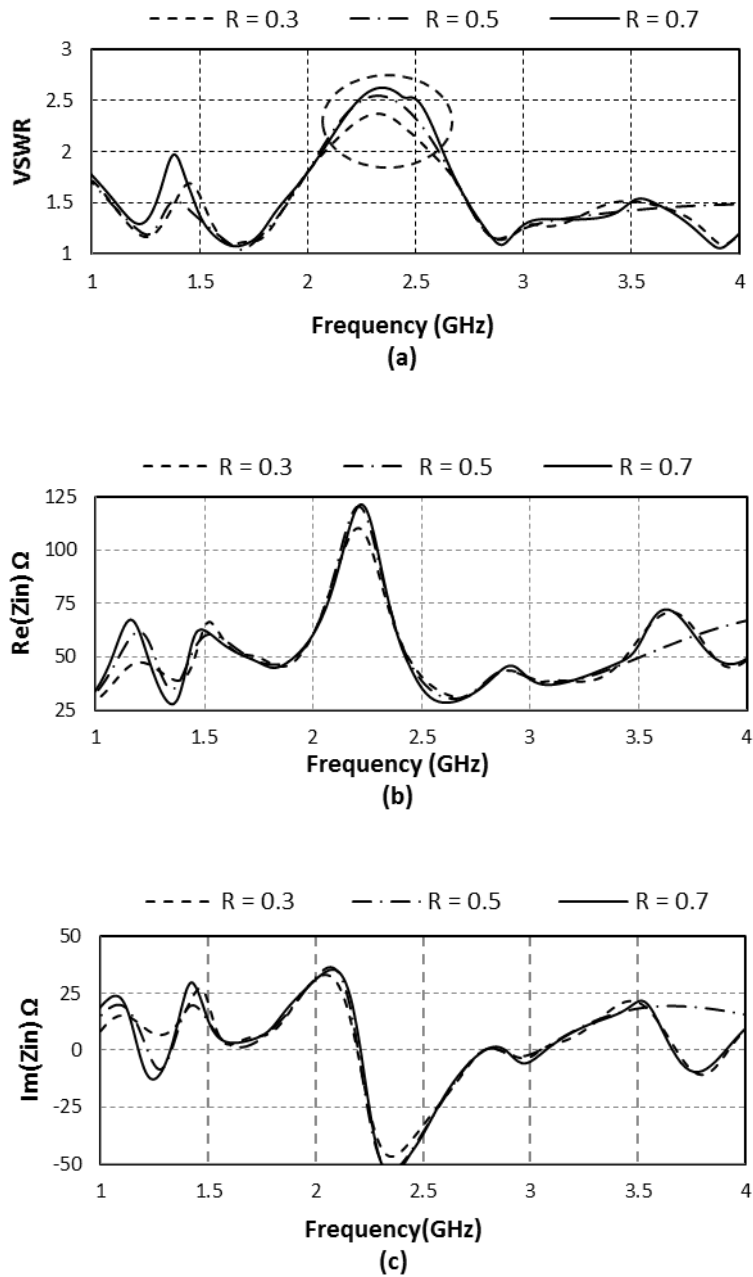


Figure 3.8 Effect of the opening rate, R on (a) input VSWR, (b) the real and (c) imaginary parts of the input impedance.

The second parameter is the opening rate of the antenna, R , shown in Fig. 3.8 (a)-(c). As the opening rate gets smaller, slightly better performance can be seen, especially at low frequencies. On the other hand, when the opening rate gets larger, an increase in the real and imaginary parts of the input impedance is noticed that would cause visible mismatch close to the mid band

The third parameter that significantly affects achieving a good antenna input match is the reactive impedance layer structure, for example, the parameters $W2$ and $Space$ of the unit cell of the periodic structure as shown in Figure 3.5. Both unit cell parameters control the real and imaginary parts of the input impedance. Their effect on the input VSWR and input impedance is shown in Figure 3.9 (a)-(c). Additionally, the reactive impedance surface periodicity determines the reflection phase. The reflection phase for different square lattice widths was calculated using HFSS Floquet modes simulation and is shown in Figure 3.10. The simulation indicates that non-reversal phase shift (i.e. $-90^\circ < \phi < 90^\circ$) occurs around 1.75-2.5GHz with $W2=5\text{mm}$ for an infinite periodic structure. However, the size of the utilized reactive impedance surface is only $10 \times 10 \text{ cm}^2$ and it contains only 9×9 units, and further optimization would still be required to broaden its operating band.

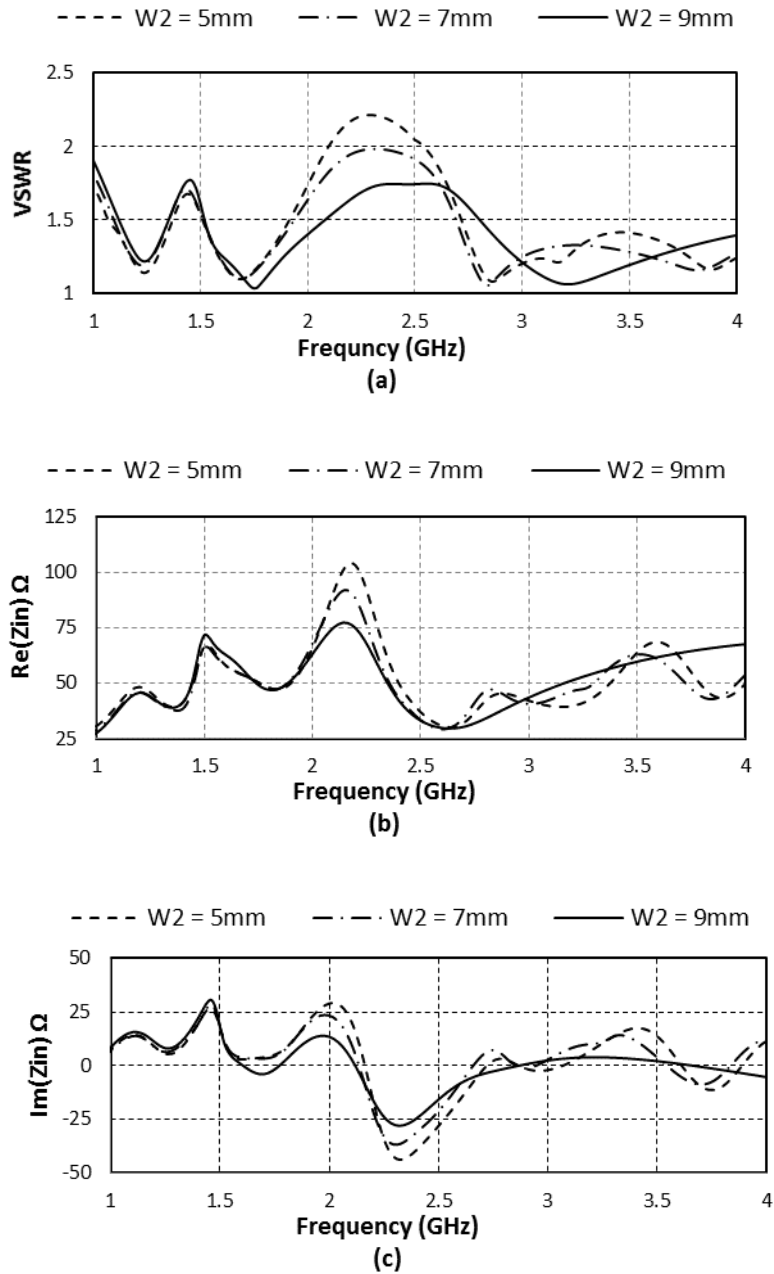


Figure 3.9 Effect of the reactive impedance layer, $W2$ on (a) input VSWR, (b) the real and (c) imaginary parts of the input impedance.

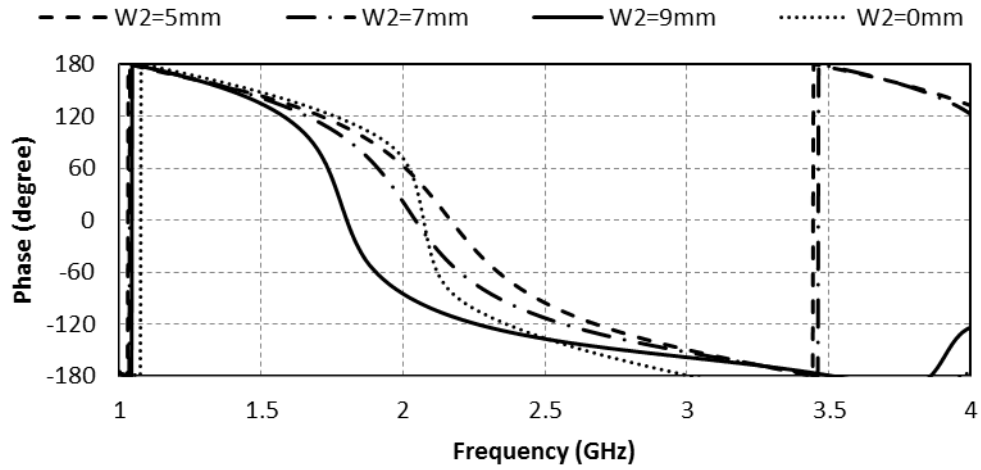
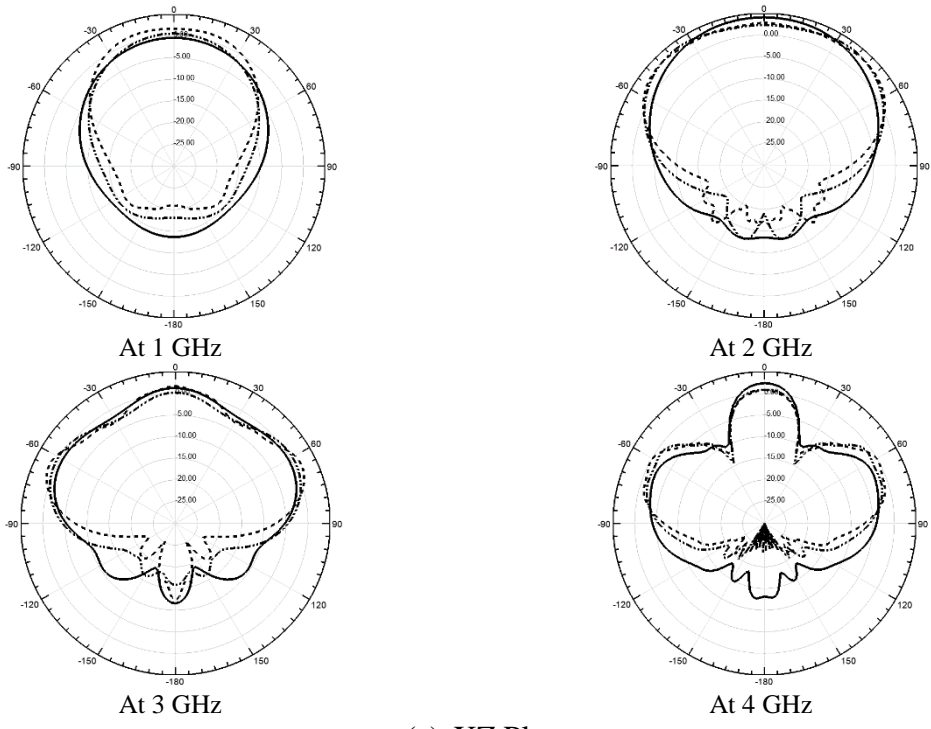


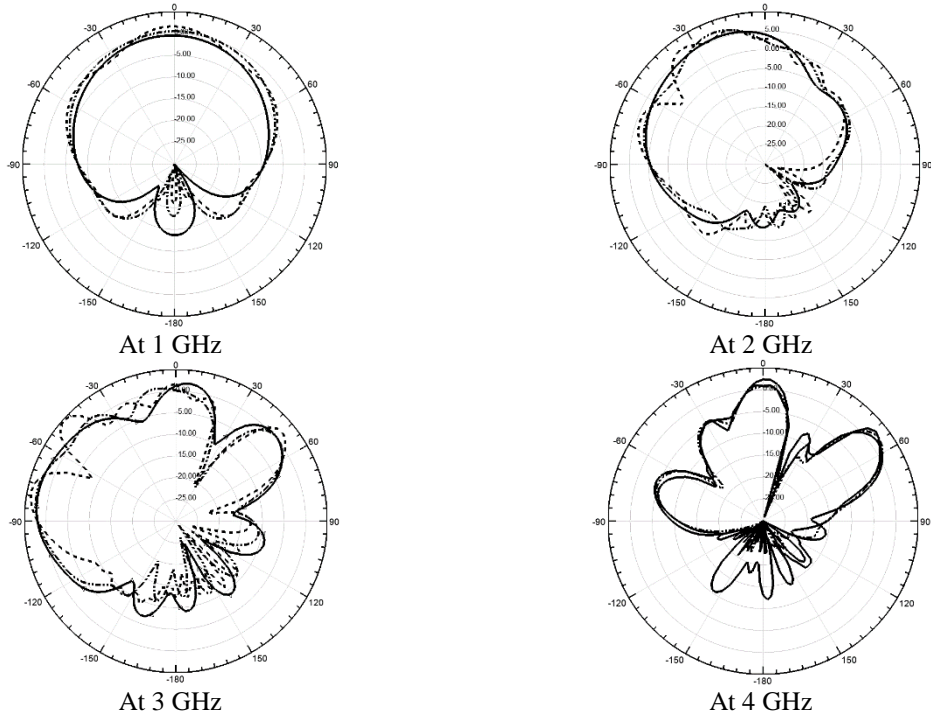
Figure 3.10 Reflection phase of the reactive impedance layer structure.

Another important parameter for the antenna is the effect of the size of its ground plane on its radiation. In Figure 3.11 and 3.12, the radiation pattern and VSWR were not significantly affected by the ground plane size. Hence, the antenna was fabricated and assembled with the various dielectric panels and a ferrite tile on a 10 cm × 10 cm square metallic plate.

— GND : 20 cm x 20 cm - · - GND : 40 cm x 40 cm - - - GND : 80 cm x 80 cm



(a) XZ Plane



(b) YZ Plane

Figure 3.11 Effect of the ground plane size (GND) on the radiation pattern.

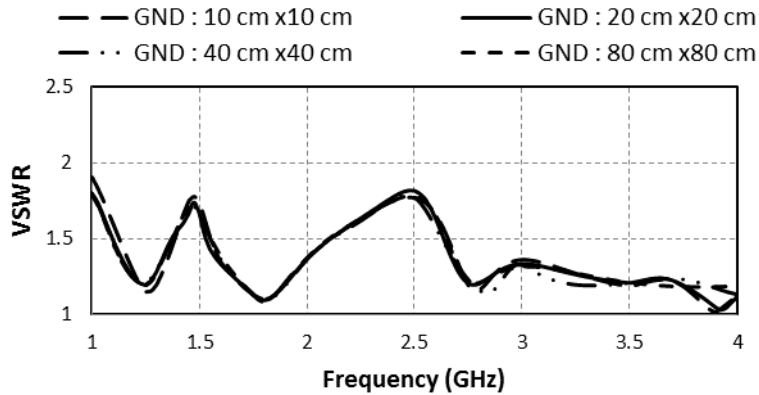


Figure 3.12 Simulated and measured VSWR of the proposed antenna.

3.4. Numerical and Experimental Results

The proposed antenna was fabricated and is shown in Figure 3.13. A 50Ω SMA connector is used to feed the microstrip feed line of the tapered slot wideband antenna. Various structures were evaluated with and without the multi-layer backing. The physical size of the antenna with the composite substrate is 10 cm × 10cm × 6.5cm which is $0.33\lambda \times 0.33\lambda \times 0.22\lambda$ at the lowest operating frequency of 1 GHz.



Figure 3.13 Prototype of the proposed conformal wideband antenna embedded in ballistic panels.

3.4.1. VSWR

Simulation and measurement results of the VSWR are consistent and demonstrate that a good input match has been obtained. Specifically, the input match is better than 10 dB in the frequency range from 1 to 4 GHz as shown in Figure 3.14.

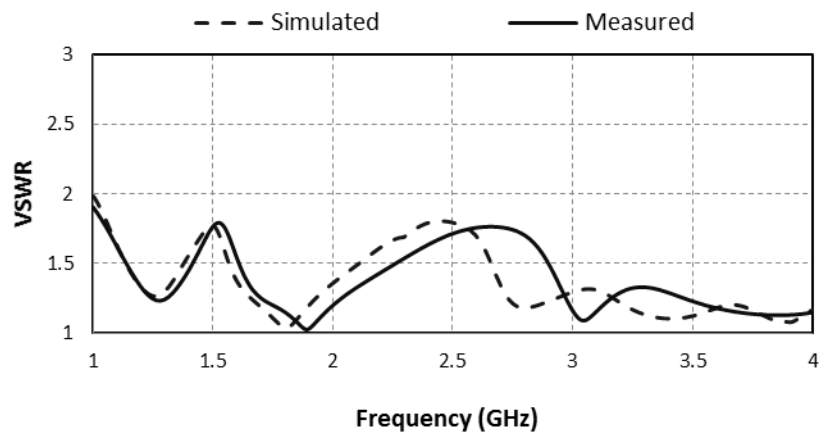


Figure 3.14 Simulated and measured VSWR of the proposed antenna.

3.4.2. Radiation Pattern and Gain

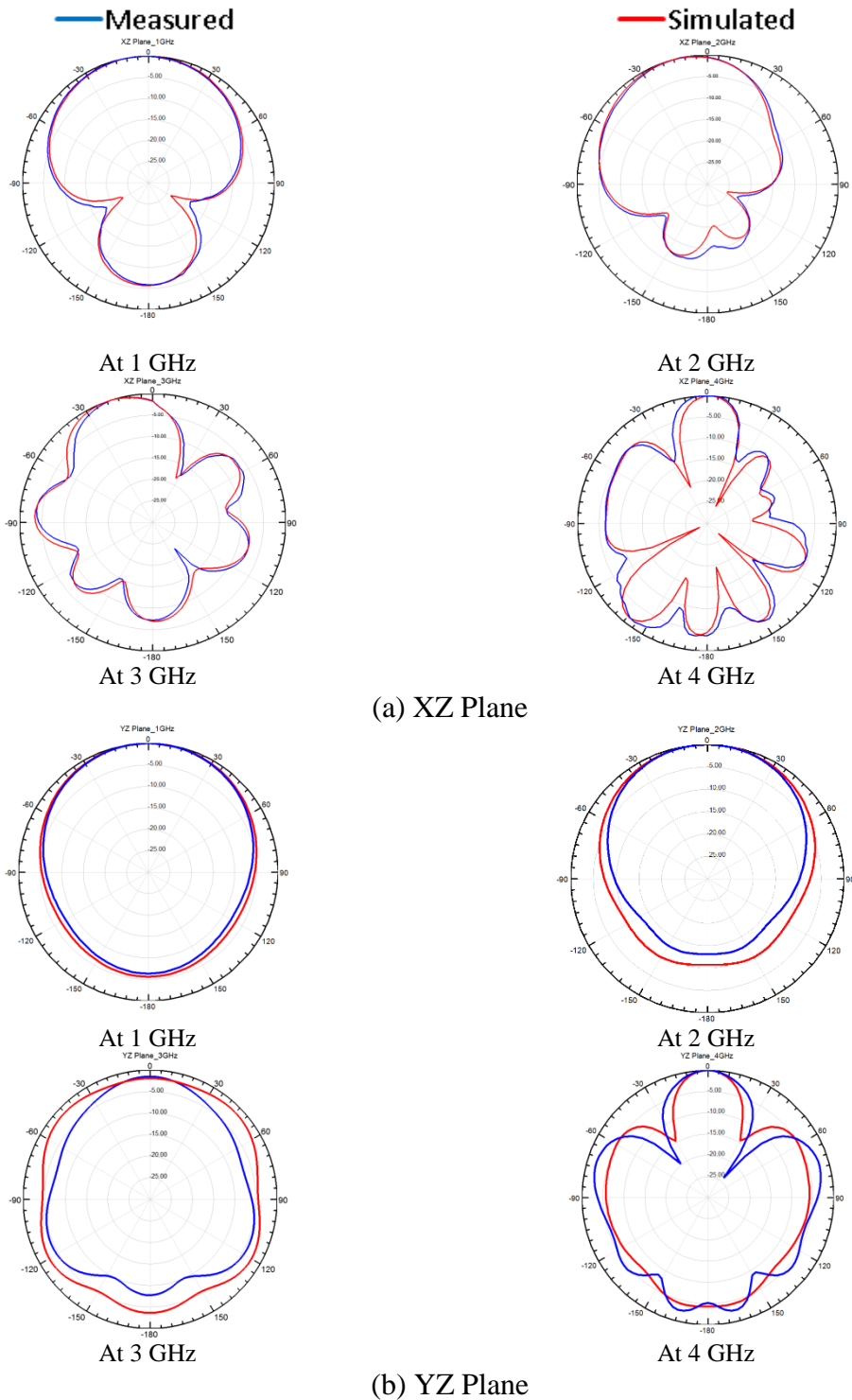


Figure 3.15 Radiation patterns in (a) XZ- and (b) YZ-plane.

Radiation patterns are plotted with respect to two orthogonal planes in Figure 3.15. The gain is positive over 1 to 4 GHz, and it is 0.9, 1.8, 2.6 and 1.9 dB at 1, 2, 3, and 4 GHz respectively. Measured results are similar to the simulated ones as seen in Figure 3.15. The radiation patterns of the slot antenna, however, have a noticeable beam squint in the XZ plane as seen in Figure 3.15.

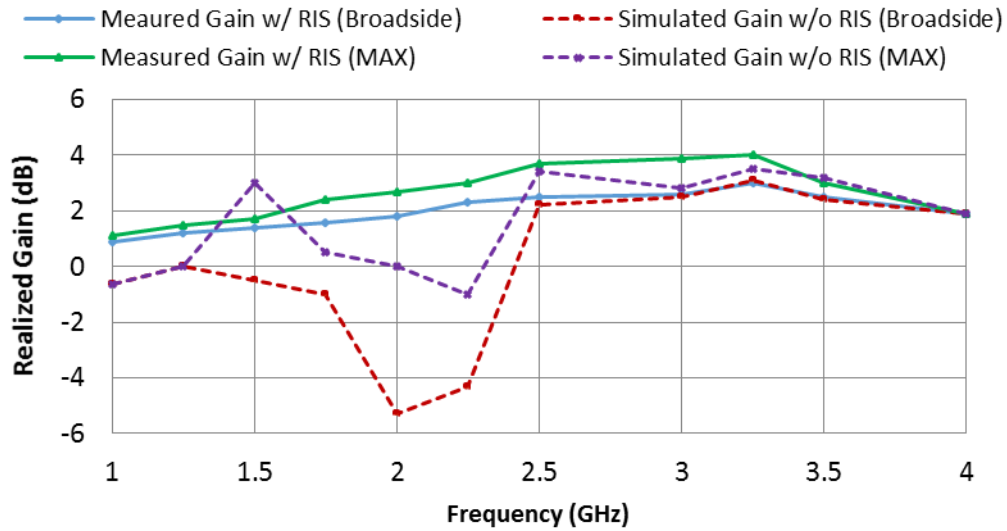


Figure 3.16 Measured and simulated gain of the antenna in dB scale.

Figure 3.16 presents the simulated and measured realized gain in two different cases of the antenna. A noticeable observation from Figure 3.16 is that without a RIS, the slot antenna gain is reduced by as much as 6dB and turned negative between 1.5 and 2.5 GHz. On the contrary, the presence of a RIS not only removes the discontinuity in the center of the desired range, but improves the gain in the mid frequency range.

3.5. Conclusion

A low profile ultra wideband tapered slot antenna with superstrate, a RIS, and a ferrite tile was presented. The antenna is covered with a composite panel as a superstrate. The hybrid RIS and composite ground plane does not cause phase reversal but does improve the broadside gain and eliminates gain drop in the middle of the operating frequency range as well. The composite ground emulates a magnetic wall and operates over wide band. The use of high RIS backed by ferrite prevents surface waves and minimizes ferrite excessive loss effects. A wide band and positive gain performances have been obtained over 1 to 4 GHz with the proposed antenna.

CHAPTER IV ENHANCED SYSTEM FOR VITAL SIGN DETECTION

Many issues related to UWB radar systems implementations have been addressed in the past. However, more improvements are still needed in hardware and software development. In the last few years, for example, there has been significant progress in developing various basic blocks of UWB transceivers [1]-[4]. Additionally, various methods and algorithms were introduced to analyze the return signal and extract various features like heart rate and respiration rate [5].

Typically, we use Vivaldi antennas or Vivaldi antenna arrays for the transmission/reception of the UWB pulse. However, these antennas were designed to work best in free space operation. In this chapter, we will investigate the possibility of redesigning/optimizing this antenna for operation taking into account the wall effects as an integral part of the antenna operation.

Additionally, we will investigate methods to improve heart rate and respiration rate algorithms for both CW and UWB pulsed radar.

First, we will review the operating frequency selection to accommodate walls presence, then review the common blocks of a radar system, then introduce the re-designed Vivaldi antennas with different walls, shows the measurement results. Also, propose a new algorithm with the re-designed antenna for vital signs detection.

4.1. Operation Frequency Selection

The operation frequency selection is essential for the optimal design and implementation of a UWB pulsed radar system. Sometimes the radar is used to detect and investigate human subjects in a harsh environment, such as through barrier, debris or blockage. In another application, the early breast cancer detection, the microwave signal has to penetrate through the normal breast tissue before seeing the cancerous tissue, which is very lossy as well. Therefore, the through barrier attenuation has to be considered during the development of the UWB pulse radar.

To better understand the through-barrier attenuation of a UWB pulse signal, transmission characteristics have been analyzed by Y. Wang [15] for various building materials, including: drywall, wood, glass, brick, and concrete. The typical complex permittivity of these materials [13], [14] is listed in Table 4.1. It was assumed that the materials are homogeneous as well as both the real and imaginary parts are constant with frequency (from DC to 12 GHz). A 6-inch thickness was utilized for all materials in the analysis. The propagation characteristics through the drywall, wooden wall, glass, brick wall, and concrete wall over the DC-12 GHz frequency range are presented in Figure. 4.1. The characteristics of wall are given below in detail. It should be noted that it is based on a one-way propagation. The loss calculation was carried using a plane wave reflection and transmission assumption in [16].

In radar operation, the signal travels a round trip and is attenuated twice by the wall. Therefore, it is suggested that the operation frequency does not go beyond 6 GHz for seeing through brick-wall or 4 GHz for seeing through concrete-wall.

Table 4.1 Characteristics of Various Building Material

Material	ϵ'	ϵ''	Loss Tangent*
Drywall	2.0	0.01	0.005
Wood	2.5	0.05	0.02
Glass	6.4	0.032	0.005
Brick	4.0	0.2	0.05
Concrete	6.8	0.9	0.13

* Loss tangent values were assumed constant in the microwave range.

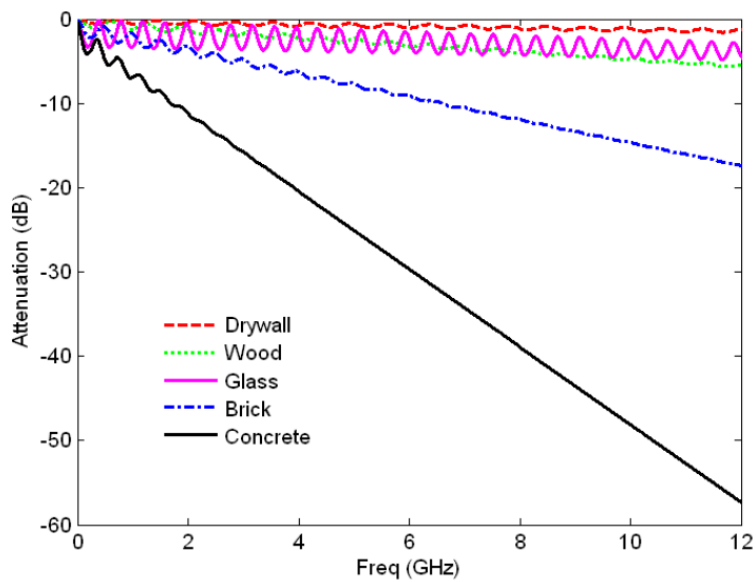


Figure 4.1 Simulated one way through wall reflection and transmission through various building materials with a thickness of 6 inch.

Additionally, and as we expect, the signal decays faster at higher frequencies when penetrating through various building materials. The attenuation is acceptable when penetrating through drywall, wood and glass over the analysis frequency range DC-12 GHz. However, the attenuation increases significantly with frequency for brick walls and concrete walls, as shown in Figure 4.1.

Based on Figure 4.1, it is clear that wall reflections are significant in cases of dry wall and wood, but the through-barrier loss is dominant in the case of cement and bricks compared to reflection loss. We can also observe that for better penetration, in general, we need to operate at lower frequencies. In the case of bricks, significant loss will occur at frequencies beyond 6GHz.

4.2. 1.5-4.5GHz UWB Pulse Radar System

4.2.1. Transceiver RF Front End

The detailed block diagram of the developed UWB Doppler radar is shown in Figure 4.2. At the transmitting link, a 10 MHz driving clock generated by FPGA circuitry is used to drive a 700ps Gaussian pulse generator. The Gaussian pulse is modulated by a 3.1 GHz carrier signal through a Hittite HMC213 mixer before passing through a driving RF amplifier Hittite HMC753 and a high gain power amplifier Mini-Circuits ZHL-42. The amplified signal is then sent out via a wideband Vivaldi antenna. At the receiver side, the collected radar returned signal is amplified by a Hittite HMC753 low noise amplifier (LNA) before being down-converted into baseband. The down conversion is implemented by mixing the modulated signal with the same 3.1 GHz carrier signal through Hittite HMC213 mixer. Therefore, the developed radar is a coherent system, i.e.,

transmitter and receiver use the same carrier signal from a Mini-Circuits ZX95-3360 voltage controlled oscillator (VCO). Next, the baseband I and Q signals are low-pass filtered and amplified before being sent to the data sampling and acquisition module.

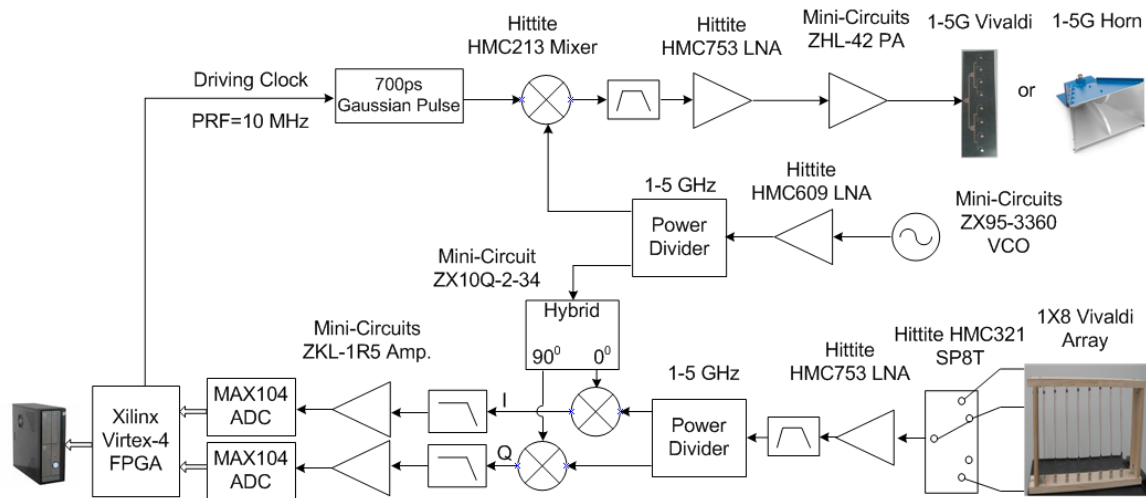


Figure 4.2 Detailed block diagram of the developed UWB pulse radar.

The photograph of the in-house designed transceiver RF front-end prototype is shown in Figure 4.3.

Figure 4.4 introduces the link budget analysis of the radar transceiver. The radar transmitting power level is mainly decided by the last stage power amplifier. The selected commercial component ZHL-42PA from Mini-Circuits provides a 1dB output power compression point of 28dBm. However, we have a slightly left margin when driving the power amplifier to avoid the obvious nonlinearity and signal distribution observed at the spectrum analyzer. A 25dBm output power is finally generated and sent to transmitting antenna. At the receiver side, the commercial LNA HMC753 has a 1dB input

compression point of 1dBm. Meanwhile, it is found that the commercial mixer HMC213 claims a 1dB input gain compression point of 9dBm and that is the limiting factor for maximum receiver input power level. Based on that, we have figured out the maximum input power level injected into radar receiver to be 0dBm. Therefore, the minimum isolation requirement between the radar transmitter and receiver is 25 dB, which can be easily achieved by separating the transmitting and receiving antennas apart, or putting the transmitting antenna slightly forward to reduce the coupling between them. Table 4.2 shows the analysis of the isolation requirement between radar transmitter and receiver.

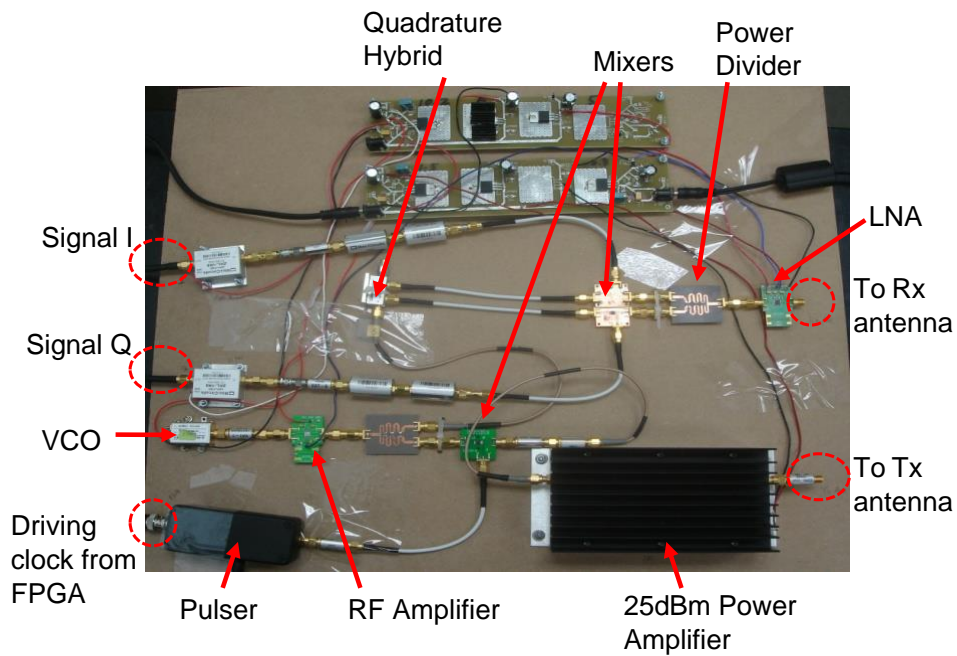


Figure 4.3 Photograph of the developed UWB PD radar RF front-end module.

The dynamic range of the radar receiver is also analyzed, as shown in Table 4.3. The thermal noise floor of the receiver is -174 dBm/Hz, or -114 dBm/MHz. The radar receiver has a bandwidth of about 3 GHz. Thus, the noise floor of the radar receiver is -79 dBm. The receiver has a noise figure of approximately 8dB, which is mainly due to the cable loss, SP8T switch loss, and the noise figure of the HMC753. Meanwhile, the minimum signal-to-noise ratio (SNR) required in order to reconstruct an acceptable image quality is 6dB [6]. Subsequently, we can acquire the radar receiver sensitivity to be -65 dBm. Since the receiver 1dB input compression point is 0dBm, the receiver has a dynamic range of as large as 65 dB.

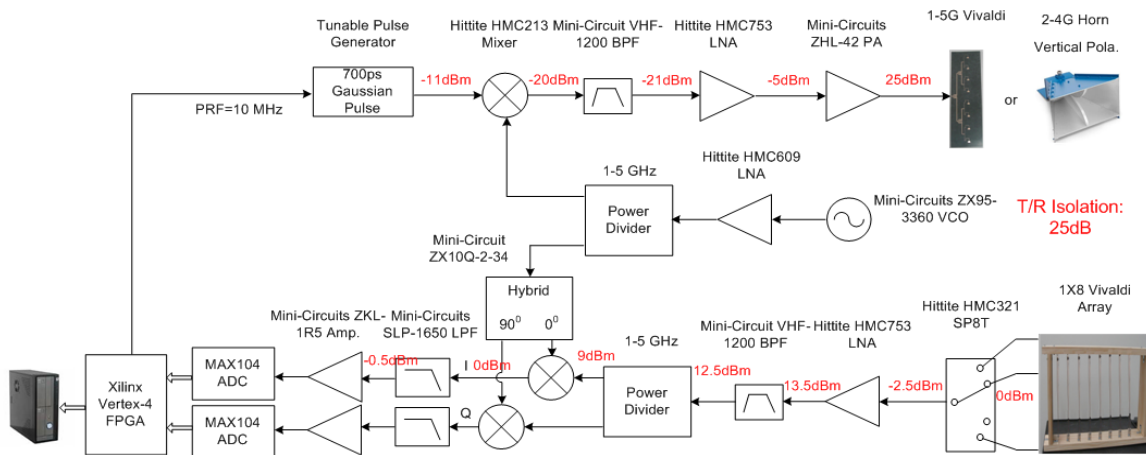


Figure 4.4 Link budget analysis of the radar transceiver.

Table 4.2 Isolation requirement between radar transmitter and receiver

Parameters	Values
Transmitter Total Power (dBm)	25
Rx 1dB Compression Point (dBm)	0
Required Tx-Rx Isolation (dB)	25
Tx/Rx Isolation easily achieved by putting Tx and Rx antennas apart	

Table 4.3 Dynamic range analysis of the radar transceiver

Parameters	Values
Rx Thermal Noise Floor (dBm/Hz)	-174
Rx Thermal Noise Floor (dBm/MHz)	-114
Receiver Bandwidth (GHz)	3
Receiver Thermal Noise Floor (dBm)	-79
Receiver Noise Figure (dB)	8
Receiver Noise Floor (dBm)	-71
Required SNR (dB)	6 (for acceptable image quality)
Receiver Sensitivity (dBm)	-65
Rx 1dB Compression Point (dBm)	0
Receiver Dynamic Range (dB)	65

4.2.2. Conventional 1.5-4.5GHz Vivaldi Antenna and Array Design

It is believed that a good antenna candidate for portable UWB radar systems should feature a wideband, directional radiation pattern, and low phase distortion operation whilst being small size and low cost. There are various options to design such an antenna: stacked patch [7], microstrip slot [7], antipodal/tapered slot Vivaldi [8], coupled sectorial loops [9], elliptical-shaped dipole/monopole [10], or etc. Here we consider an exponential taper slot Vivaldi antenna. A photograph of a fabricated Vivaldi antenna, designed by Y. Wang [17] that was previously used in our system is shown in Figure 4.5, with a size of 12cm by 9cm. It was fabricated on a 31-mil thick Rogers RT5880 substrate, which has a dielectric constant of 2.2 and loss tangent of 0.0009. A wideband microstrip line to slotline transition [11] was utilized to feed the exponential tapered slot which has significantly enhanced the impedance bandwidth. It's measured VSWR performance, in free space operation, agreed very well with the simulation results; indicated by its good match at 1 to 5.5 GHz, as shown in Figure 4.6.

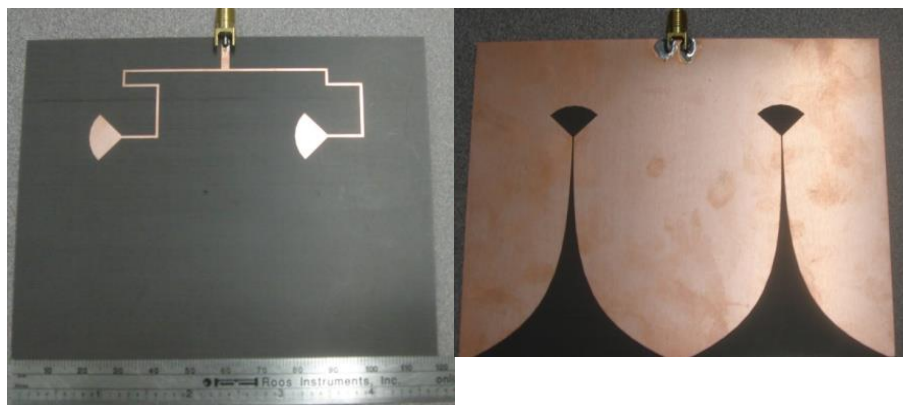


Figure 4.5 Photograph of a top view and bottom view of the compact wideband Vivaldi antenna, with a size of 12cm by 9cm and a thickness of 31-mil.

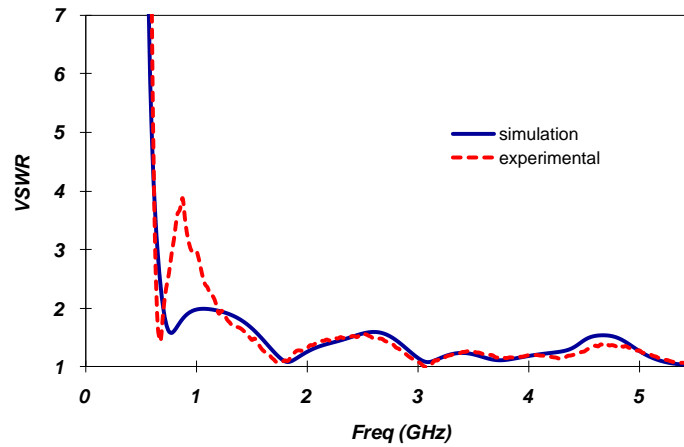
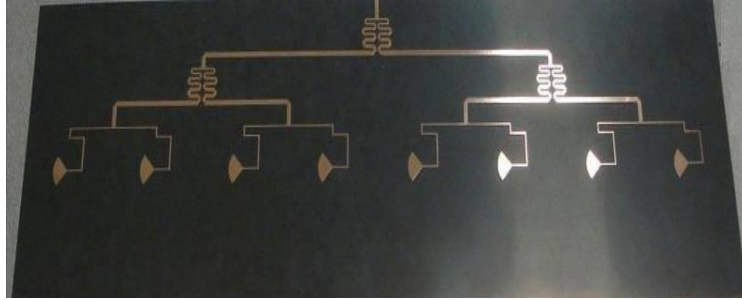


Figure 4.6 Simulation and experimental VSWR result of the fabricated Vivaldi antenna.

The designed, free space operated, Vivaldi antenna was utilized as a basic building block to design a sub-array in order to increase the overall gain and narrow down the beamwidth, i.e. becomes more directive, as shown in Figure 4.7. A three-section wideband power divider [12] was utilized to form the feeding network. Measured return loss indicated a good matching performance of the antenna from 1 to 5.5 GHz, as shown in Figure 4.8. Introduced in Figure 4.9, the Vivaldi sub-array achieved good directional radiation patterns over the operational frequency range based on measurements. A 3dB beamwidth of 12 degrees at E-plane and 120 degrees at H-plane have been achieved at 3 GHz when operating in free space.



(a) Top view



(b) Bottom view

Figure 4.7 Photograph of the fabricated Vivaldi sub-array.

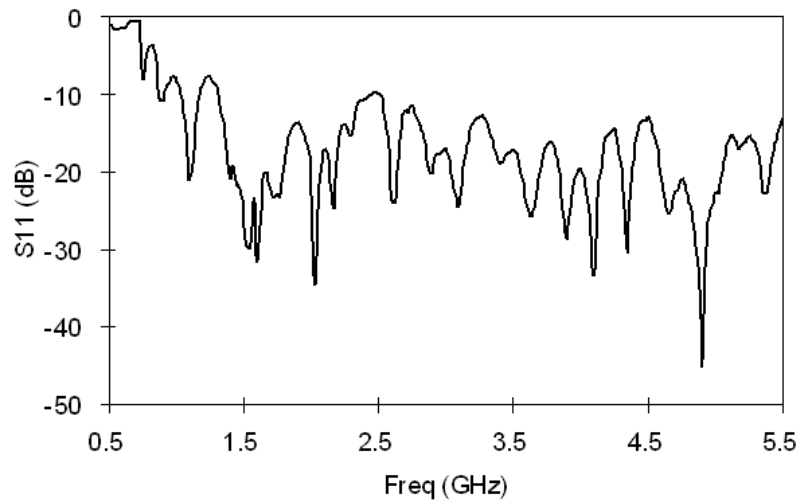
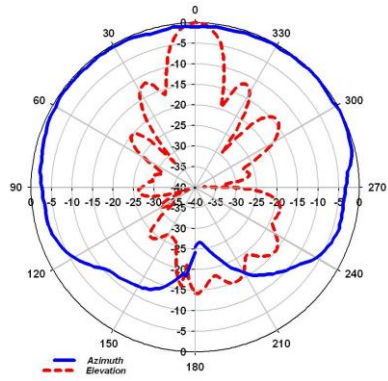
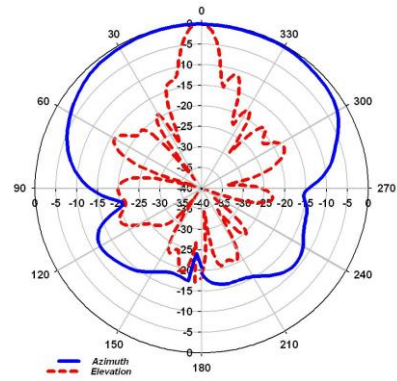


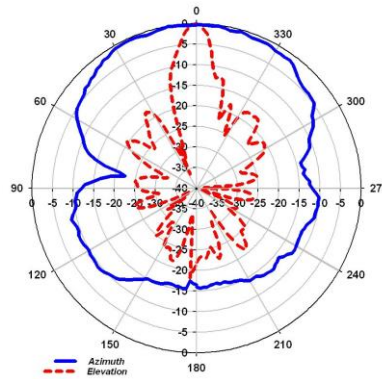
Figure 4.8 Measured return loss of the Vivaldi sub-array, showing good match at 1 to 5.5 GHz.



(a) 2 GHz



(b) 3 GHz



(c) 4 GHz

Figure 4.9 Measured radiation pattern of the Vivaldi sub-array, showing good directional characteristics over the operation frequency

In order to investigate the effect of various walls, we measured the S_{21} (dB) in free space as a reference level of S_{21} at 2.5 m distance from a reference antenna in Figure 4.10.

However, the presence of the wall at a distance can affect the overall performance. We carried out a few experiments to observe the effect of a cement wall in Figure 4. 11. We fixed the distance between the Vivaldi antenna and the reference antenna, and changed the location of the wall from 0 cm to 10 cm. It showed that the Vivaldi antenna

which is designed in free space lost at least 2 dB of transmitted power due to the presence of wall over the operating frequency.

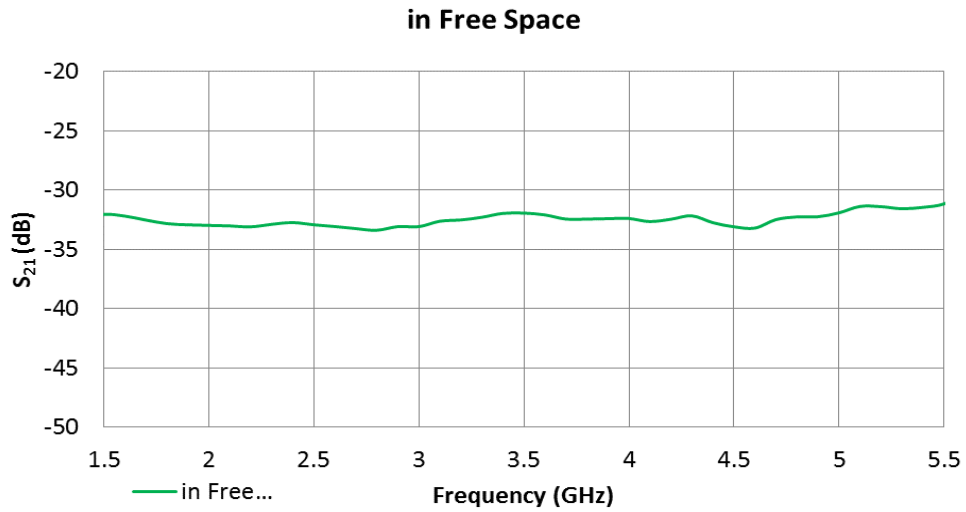


Figure 4.10 Measured S_{21} (dB) of the 2 elements of the Vivaldi antenna, showing good S_{21} (dB) over the operation frequency.

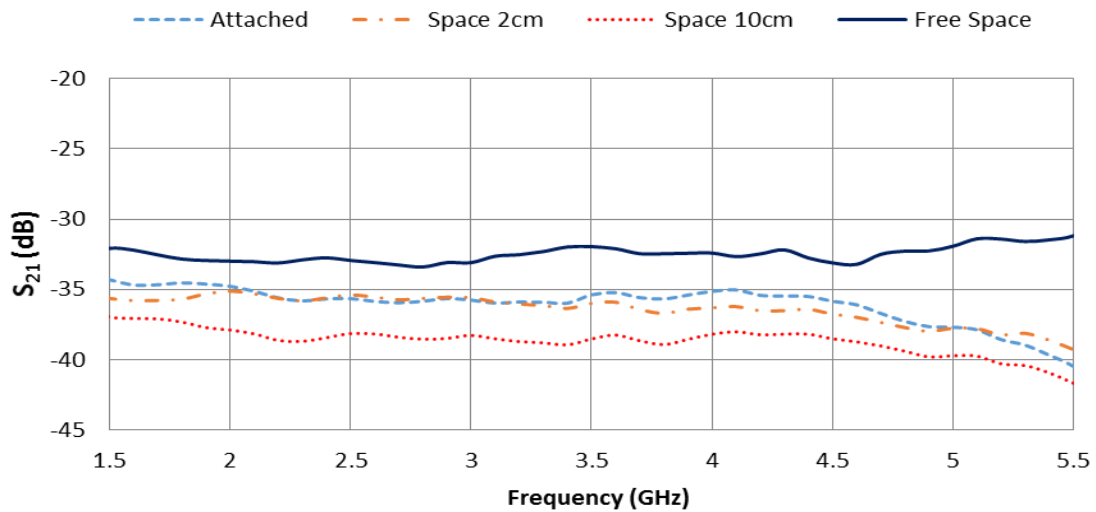


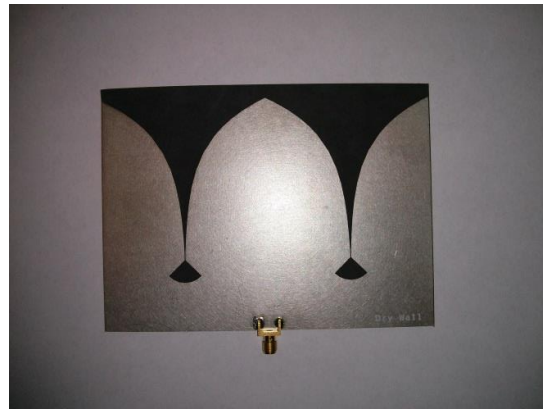
Figure 4.11 Measured S_{21} (dB) of the 2 elements of conventional Vivaldi antenna depending on the location of a brick wall.

Here, in an effort to improve the returned signal from a buried target under debris, or a person hidden behind a wall, we initially investigated the through wall attenuation and reflection. Subsequently, we redesigned the antenna design and re-optimized it to mitigate the wall effects.

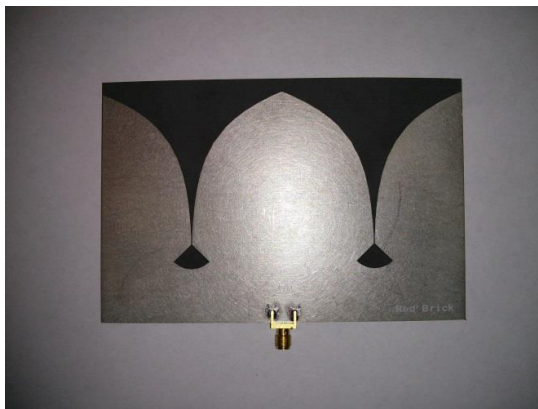
4.3. Antenna Design Optimization with Various Walls



(a) Antenna designed in free space



(b) Antenna designed with wood wall

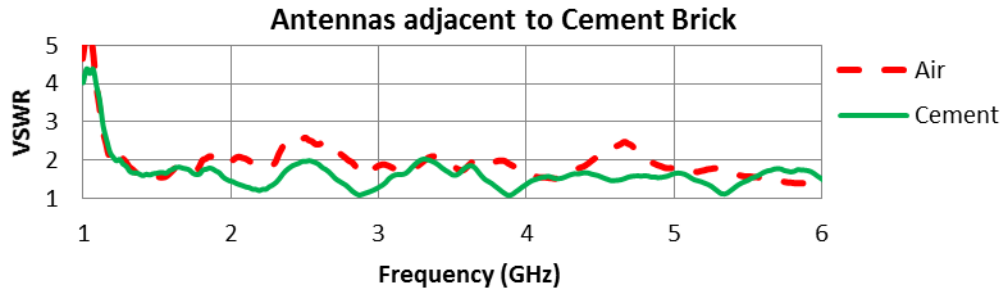


(c) Antenna designed with brick wall

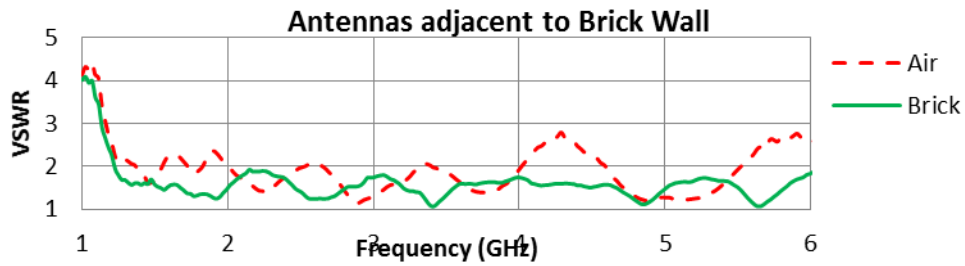


(d) Antenna designed with cement wall

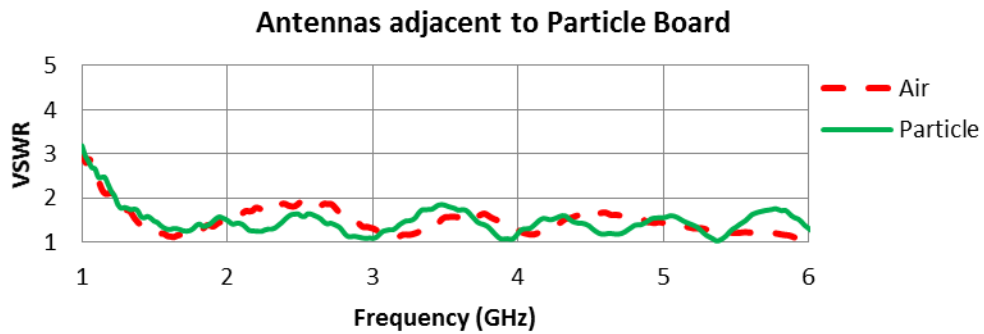
Figure 4.12 Vivaldi Antennas optimized with various walls.



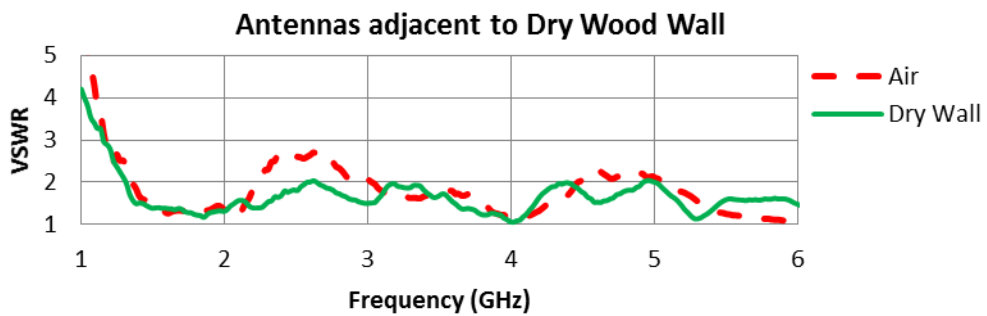
(a) Cement Wall



(b) Brick Wall



(c) Particle Board Wall



(d) Dry Wall

Figure 4.13 Vivaldi Antennas optimized with various walls.

It is believed that a better performance can be achieved if the antenna was redesigned to include the wall as an integral part of the antenna environment, especially when antennas can be attached or in close proximity of the wall situations. Unquestionably, this effect could be pronounced if the standoff distance is short, and obviously it will be impractical to account for that if it is a long distance. Also, previously addressed, wall reflections are significant in cases of dry wall and particle board, while propagation loss through barrier of cement and bricks is more dominant. We considered three different cases; dry wood wall, brick wall and cement wall and modified the current antenna design to improve the performance in Figure 4.12.

As shown in Figure 13, it is clearly visible that now the antennas designed to operate adjacent to cement, brick, wood wall behaves better than antennas designed to operate in air, i.e. the VSWR is sensitive to the material of wall.

Also, more experiments were carried out to investigate the strength of received signal comparing to it with the Vivaldi antenna designed in free space as shown in Figure 4.14.

UWB signals were transmitted with re-designed Vivaldi antennas, reflected by a stationary target, and then received with a horn antenna.

Figure 4.14 shows the strength of received signals with re-designed Vivaldi antennas compared to the strength of signals with a conventional antenna. In wood wall case, the strength of signal is significantly improved with the re-designed antenna. However, the strength of signal was measured slightly better than it with a conventional antenna in both cement wall and brick wall case.



(a) Wood wall

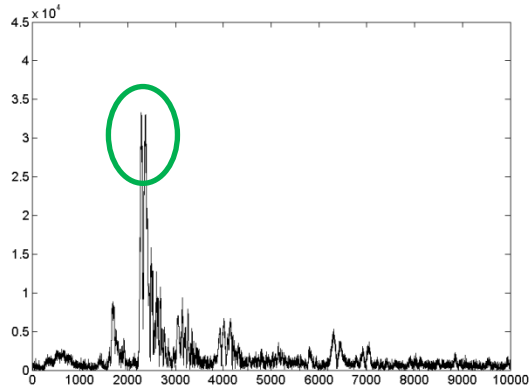
(b) Cement Wall

(c) Brick Wall

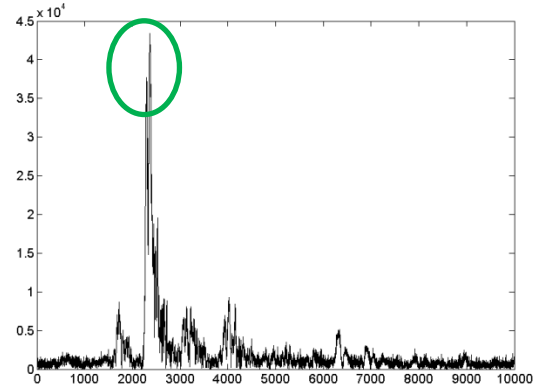
Figure 4.14 Set up for measuring the received signal.

Figure 4.16 compares the performance of various antennas and environment scenarios to indicate the effect of wall on overall radiation pattern. We have studied four cases:

1. The performance of an antenna designed to operate in free space and used it as our reference.
2. The free-space antenna radiates into a wall when it was adjacent to the wall.
3. Free-space antenna separated 3 cm and 10 cm from the wall.
4. Finally, the optimized design that was directly adjacent to the wall. (as shown in Fig. 4.16)

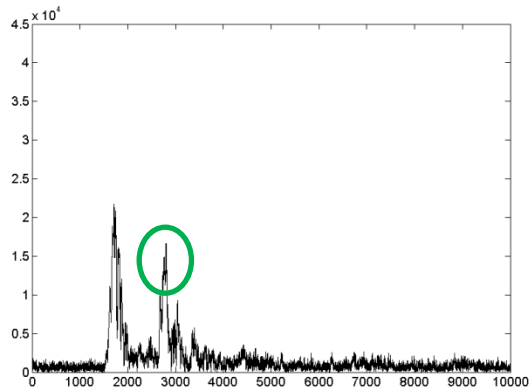


(a) Conventional Vivaldi

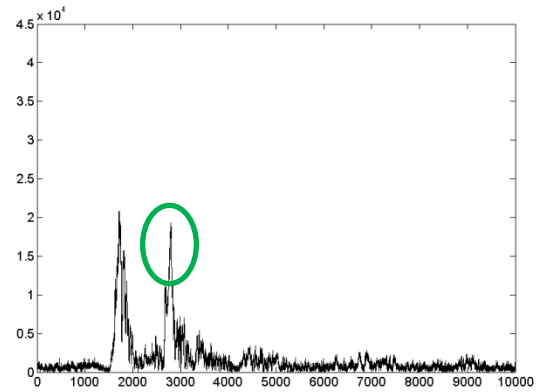


(b) Re-designed Vivaldi

A. Wood wall case

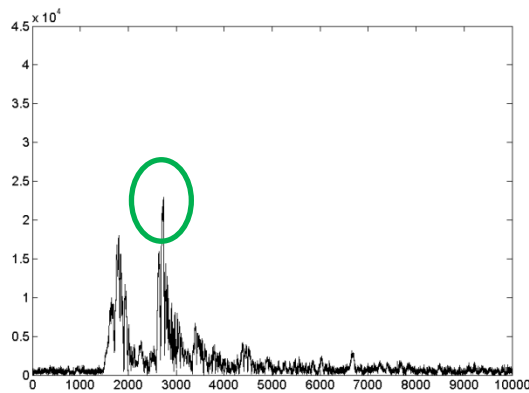


(a) Conventional Vivaldi

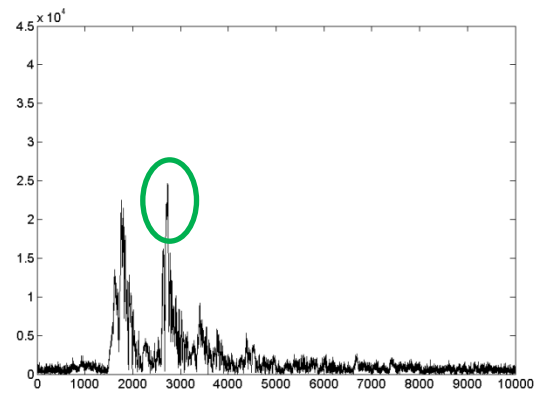


(b) Re-designed Vivaldi

B. Cement wall case



(a) Conventional Vivaldi



(b) Re-designed Vivaldi

C. Brick wall case

Figure 4.15 Received signal comparison in various walls cases.

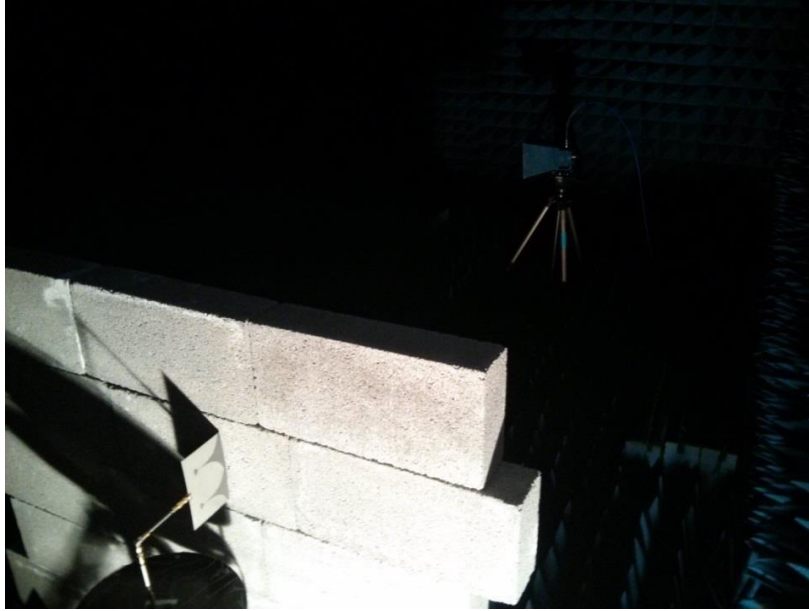


Figure 4.16 Radiation measurement setup adjacent to a cement wall.

Fig. 4.17 shows the measurement of S_{21} (dB) of the optimized Vivaldi antenna on a brick wall comparing to the other cases with a conventional Vivaldi antenna.

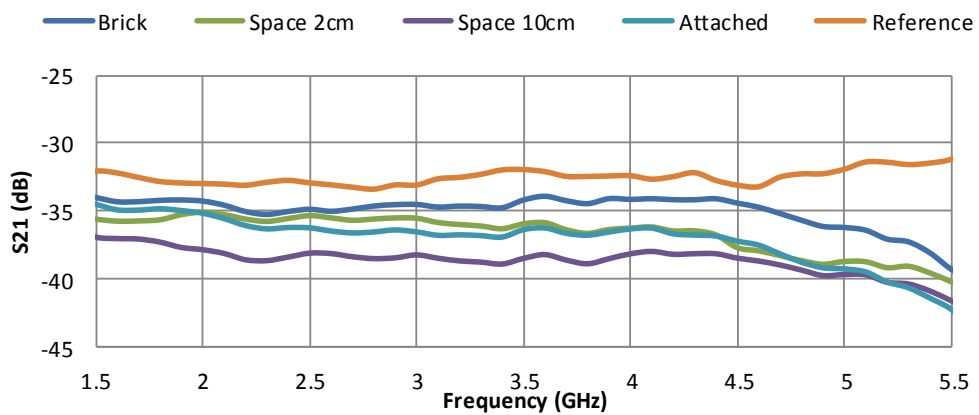
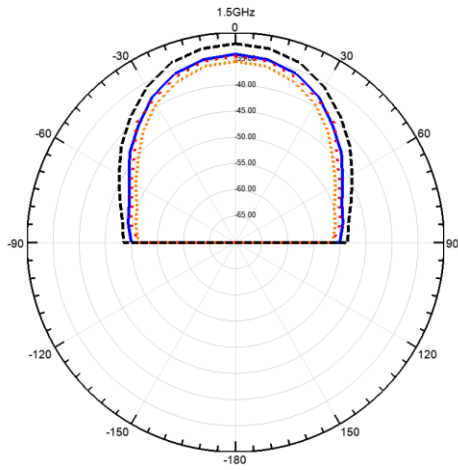


Figure 4.17 Radiation measurement.

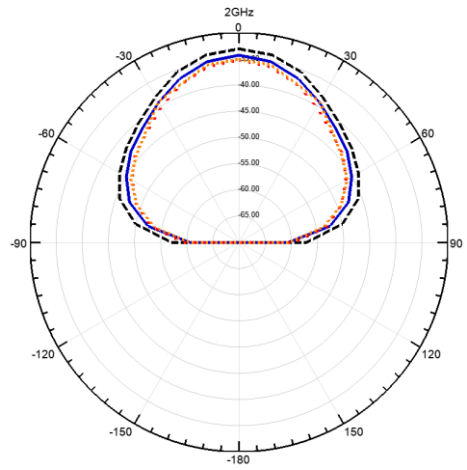
Table 4.3, indicates that over 1.5-5.5 GHz, the optimized antenna has a better performance compared to the conventional design when it was attached or even separated from the wall.

Table 4.4 Performance comparison between an optimized antennas and air Antenna

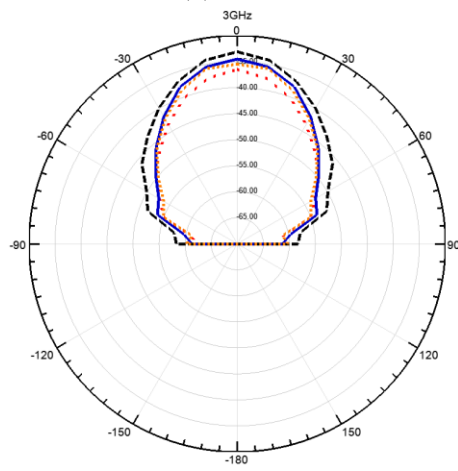
Frequency (GHz)	Opt antenna	Air antenna		Reference S ₂₁ (dB) Air to Air
	Adjacent (difference)	Adjacent (difference)	2 cm space (difference)	
1.5	-34.0 (-2.0)	-34.5 (-2.5)	-35.6 (-3.6)	-32
2	-34.2 (-1.2)	-35.2 (-2.2)	-35.1 (-2.1)	-33
3	-34.5 (-1.5)	-36.6 (-3.6)	-35.6 (-2.6)	-33
4	-34.2 (-2.2)	-36.3 (-4.3)	-36.3 (-4.3)	-32
5	-36.2 (-4.2)	-39.3 (-7.3)	-38.7 (-6.7)	-32
5.5	-39.3 (-7.3)	-42.3 (-11.3)	-40.2 (-9.8)	-31



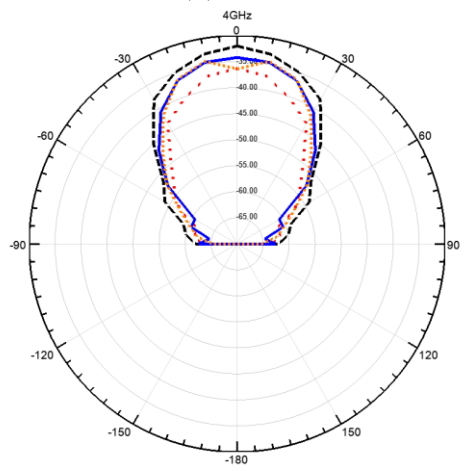
(a) 1.5 GHz



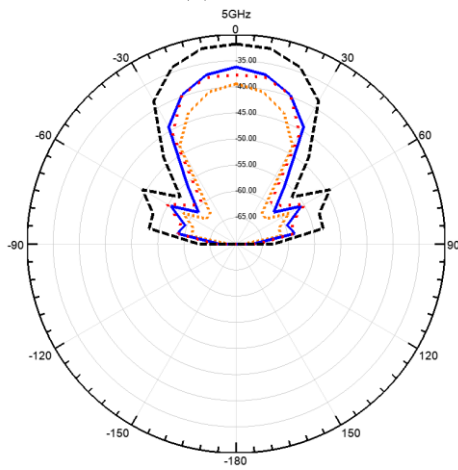
(b) 2.0 GHz



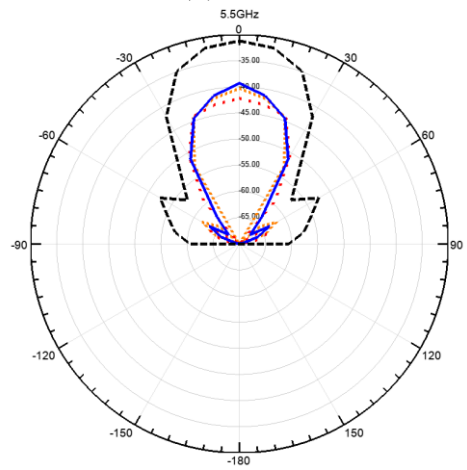
(c) 3.0 GHz



(d) 4.0 GHz



(e) 5.0GHz



(f) 5.5 GHz

-- Air — Brick - - Attached ···· 2 cm space

Figure 4.18 Measured Radiation Pattern through 3 inch brick wall.

Figure. 4.17 shows the S_{21} of each case, the radiation patterns are shown in Fig. 4.18. The Performance comparison is listed in Table 4.3. The measured S_{21} with the re-designed antenna degrades from -1.2dB to -2.2dB compared to the -2.2 dB to -4.3 dB degradation of the S_{21} with a conventional antenna at low and mid frequency range. Using a convention antenna with 2 cm apart from a brick wall, the degradation is worse than the previous cases, and shows -2.1 dB to -4.3. In the entire operating frequency range, re-designed antenna demonstrates from 0.9dB to 5dB improved S_{21} performance among the cases.

4.4. Algorithm to Enhance Vital Sign Detection

Nowadays, UWB radars systems have been used to remotely monitor subjects in many non-contact cases, and show very promising results in indoor target localization, human gait analysis and vital sign detection as well [1]. Compared to CW radar systems, UWB radar systems have the advantages of localization capability, less consumption of power, multiple subjects monitoring and so on.

UWB Doppler radar monitors vital signs of persons in a non-contact method by detecting the changes in the time of flight of narrow pulses emitted by the radar and reflected from the human chest. Conventionally, the respiration rate can be readily detected by fast Fourier transform (FTT) on the slow-time samples along the traversed rang bins, while it is hard to determine the heart rate and amplitude with high accuracy in this manner. One reason is that the amplitude of thorax motion caused by heartbeat is comparatively lower and around 0.5 mm displacement. The other reason is the harmonics

of respiration rate and intermodulation between respiration and heartbeat signals tend to be dominant over the heart rate frequency band.

In order to detect vital signs of subjects with UWB radar systems, various algorithms have been proposed. In [2], the SNR of vital signs is greatly improved by coherently combining traversed data of range-bin target before applying FFT on the slow time samples. In [3], a method based on multiple higher order cumulant is presented. However, the performance of heartbeat detection strongly depending on the frequency window is not stable. In [4], a filter utilizing Moving Target Indicator is introduced to cancel the harmonics of respiration signals. The intermodulation between respiration and heartbeat signals could not be avoided before the implementation of time to frequency transformation.

In [5, 6], complex signal demodulation and arctangent methods with accurate and robust performance in vital signs detection have been widely used for CW radars. In [7], a generalized likelihood ratio test (GLRT) is applied to distinguish between the presences of 2, 1 or 0 subjects, while it has the limitation of labeling the heart rate to each subject.

4.4.1. Conventional 1.5-4.5GHz Vivaldi Antenna and Array Design

The block diagram of Gaussian-pulse UWB radar is shown in Fig. 2 of [8], which uses quadrature mixer to address image problem in conventional mixer. Gaussian pulses are generated and transmitted during operation. Suppose the n th pulse generated by the pulse generator is $p(t, nT)$, where t denotes the time variable in fast time, T denotes the pulse repetition period in slow time.

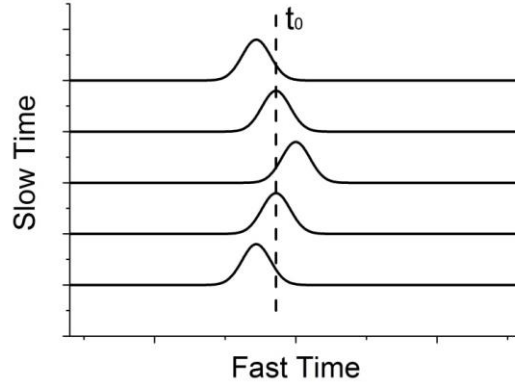


Figure 4.19 Demonstration of collected pulses.

The pulse is modulated by a f_c and the transmitted pulse is

$$\begin{aligned}
 x_t(t, nT) &= p(t, nT) \cdot \sin(\omega_c t) \\
 &= \exp\left[-\frac{t^2}{\delta^2}\right] \cdot \sin(\omega_c t)
 \end{aligned} \tag{1}$$

For convenience, the initial phase difference between pulse and sinusoid signal is supposed to be 0. Due to the derivative characteristic of antenna, monocycle will be used to model pulses reflected from subject and collected by the receiver. The pulse reflected by the subject and received by the system is

$$x_r(t, nT) = \alpha \cdot \frac{d(p(t - t_D, nT) \cdot \sin(\omega_c t - \omega_c t_D))}{dt} + C(t) \tag{2}$$

$$t_D = [2L + 2A_r \sin(\omega_r nT) + 2A_h \sin(\omega_h nT)] / c \tag{3}$$

where α denote attenuation coefficient; c is the speed of light, t_D is the time delay caused by transmission path, including thorax displacements due to respiration, $A_r \sin(\omega_r nT)$ and

heartbeat, $A_h \sin(\omega_h nT)$; L is the distance between subject and UWB radar; $C(t)$ expresses the pulses reflected from static cluttering at distance L , i.e. $t_0=2L/c$.

The reconstructed n th pulses in I and Q channels collected by FPGA are

$$\begin{aligned} I(t, nT) &= x_r(t, nT) \cdot \sin(\omega_c t) \\ &= 1/2 \cdot \sin(\omega_c t_D) \cdot [\alpha \cdot B(t, nT) + C(t)] \end{aligned} \quad (4)$$

$$\begin{aligned} Q(t, nT) &= x_r(t, nT) \cdot \cos(\omega_c t) \\ &= 1/2 \cdot \cos(\omega_c t_D) \cdot [\alpha \cdot B(t, nT) + C(t)] \end{aligned} \quad (5)$$

$$B(t, nT) = \exp\left[-\frac{(t-t_D)^2}{\delta^2}\right] \cdot \left[-\frac{2 \cdot (t-t_D)}{\delta^2}\right] \cdot \tan(\omega_c t - \omega_c t_D) + \omega_c \cdot \exp\left[-\frac{(t-t_D)^2}{\delta^2}\right] \quad (6)$$

Note that $2\omega_c t - \omega_c t_D$ components in (4) and (5) have been filtered by low-pass filter immediately after mixers. Mean value of $B(t, nT)$ in (6) is ω_c .

4.4.2. Conventional Method

The reconstructed n th pulse $P(t, nT)$ based on I/Q data is

$$\begin{aligned} P(t, nT) &= Q(t, nT) + j \cdot I(t, nT) \\ &= 1/2 \cdot \exp(j\omega_c t_D) \cdot [\alpha \cdot B(t, nT) + C(t)] \end{aligned} \quad (7)$$

As shown in Fig. 4.16, slow time samples are composed of traversed data of range-bin target at $t=t_0$. Mean subtraction is used to eliminate unwanted DC power of stationary cluttering. By focusing on the amplitude of resulting slow time samples and applying Taylor Series to (7), we could obtain the polynomial component with t_0-t_D ,

$$f(t-t_D) = \alpha \cdot \omega_c \sum_{m=-\infty}^{\infty} 1/m! \cdot (-1)^m \cdot (t_0 - t_D)^{2m} / \delta^{2m} \cdot [1 - 2 \cdot (t_0 - t_D)^2 / \delta^2] \quad (8)$$

4.4.3. Logarithm Method

Instead of detecting vital signs with variation of energy level of pulses along slow time, the proposed method will directly demodulate phase variation of pulses caused by thorax movement using data from I/Q channels. First, we accumulate each pulse along fast time t , where $[t_1, t_2]$ is the applied time window. Since the subject stays stationary, the amplitude of accumulated results (9) for each pulse is the same.

$$S(nT) = 1/2 \cdot \exp(j\omega_c t_D) \cdot \sum_{t=t_1}^{t_2} [\alpha \cdot B(t, nT) + C(t)] \quad (9)$$

By applying logarithm operation to (9), we could obtain

$$\ln[S(nT)] = j\omega_c t_D + \ln\left\{ \sum_{t=t_1}^{t_2} [\alpha \cdot B(t, nT) + C(t)] \right\} + \ln(1/2) + j \cdot 2k\pi \quad (10)$$

$$k = 0, 1, 2 \dots$$

It is obvious that imaginary part of (10) includes the vital signs related phase variation $\omega_c t_D$. By applying phase unwrapping method to (10), the component $j \cdot 2k\pi$ could be removed and phase variation caused by respiration and heartbeat could be demodulated in a straightforward way. The mean value of $\omega_c t_D$ corresponds to phase delay caused by L , as a result the real time thorax amplitude is

$$A_r \sin(\omega_r nT) + A_h \sin(\omega_h nT) = \frac{c}{2\omega_c} \cdot [\omega_c t_D - \text{Mean}(\omega_c t_D)] \quad (11)$$

Compared with conventional method in (8), harmonics of respiration signal and intermodulation between respiration and heartbeat signals are not involved with this phase-based method. Meanwhile, the cluttering effect has been taken into account as well. The logarithm method which utilizes data collected from I/Q channels is geared towards the real time monitoring of vital signs.

4.4.4. Experimental Results

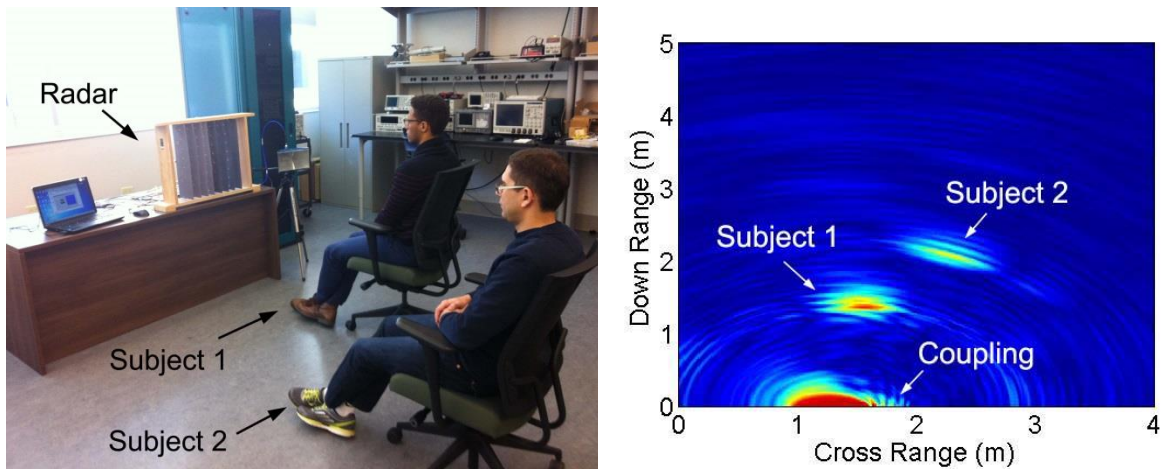


Figure 4.20 (a) Experiment setup, (b) Localization with UWB system.

UWB radar with center frequency at 3 GHz, 2 GHz bandwidth and pulse repetition frequency (PRF) of 75 Hz is used to collect the data. In the experiment of heartbeat detection of multiple subjects, two subjects were sitting 1.5 m and 2.3 m away from the receiver, and both of them breathed normally. One commercial sensor is attached to the finger of each subject as the reference. The experiment setup is shown and both subjects

are labeled in Figure 4.20(a). By using 700-ps Gaussian pulse and equivalent time sampling scheme, the UWB radar has a high resolution in the down range, distinguishing both subjects and accurately localizing them in the image, as presented in Figure 4.20(b).

The demodulated thorax displacement with logarithm method is shown in Fig. 4.21. The detected vital signs for both subjects are presented in Fig. 4.22(a) and (b). The respiration and heart rates of subject 1 are 0.34 Hz and 1.45 Hz; the demodulated respiration and heart rates of subject 2 are 0.25 Hz and 1.2 Hz. Compared with the reference signals, the detected heart rates for subject 1 and 2 show a 5% error and a 3% error respectively.

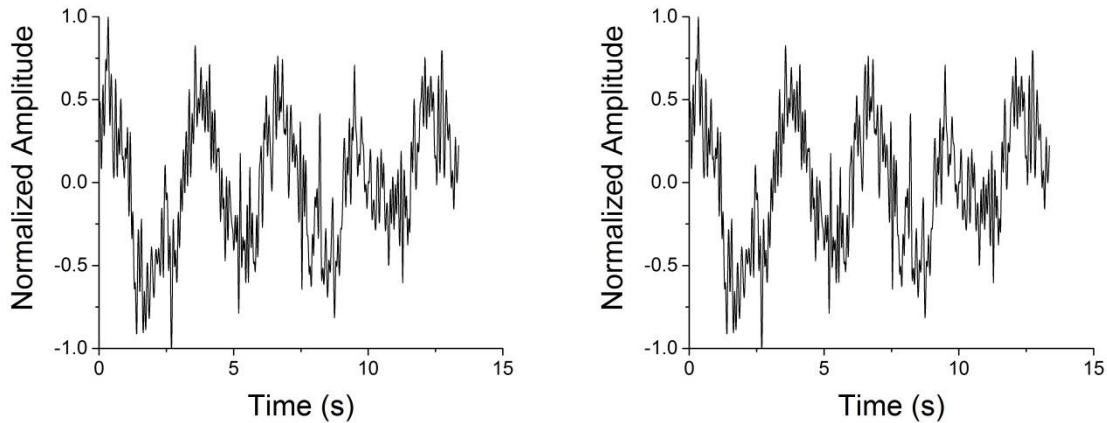


Figure 4.21 Demodulated thorax displacement of (a) subject 1, (b) subject 2.

The collected data from subject 2 was processed with conventional FFT as well to compare its performance with that of logarithm method. As shown in Figure 4.22(c), the detected respiration rate with conventional method is 0.28 Hz, while the heart rate

detected is 1.96 Hz, which actually is the 7th order harmonic of respiration. In this case, high order respiration harmonic has greater magnitude in spectrum than that of heartbeat. The vital signs detected with logarithm method are shown in Figure. 4.22(b), where the respiration rate is 0.28 Hz, the same with rate detected with conventional method, and heart rate matches well the reference with an error of 3%. It is demonstrated in this experiment that logarithm method outperforms the conventional method in heartbeat detection by avoiding the harmonics of respiration signal.

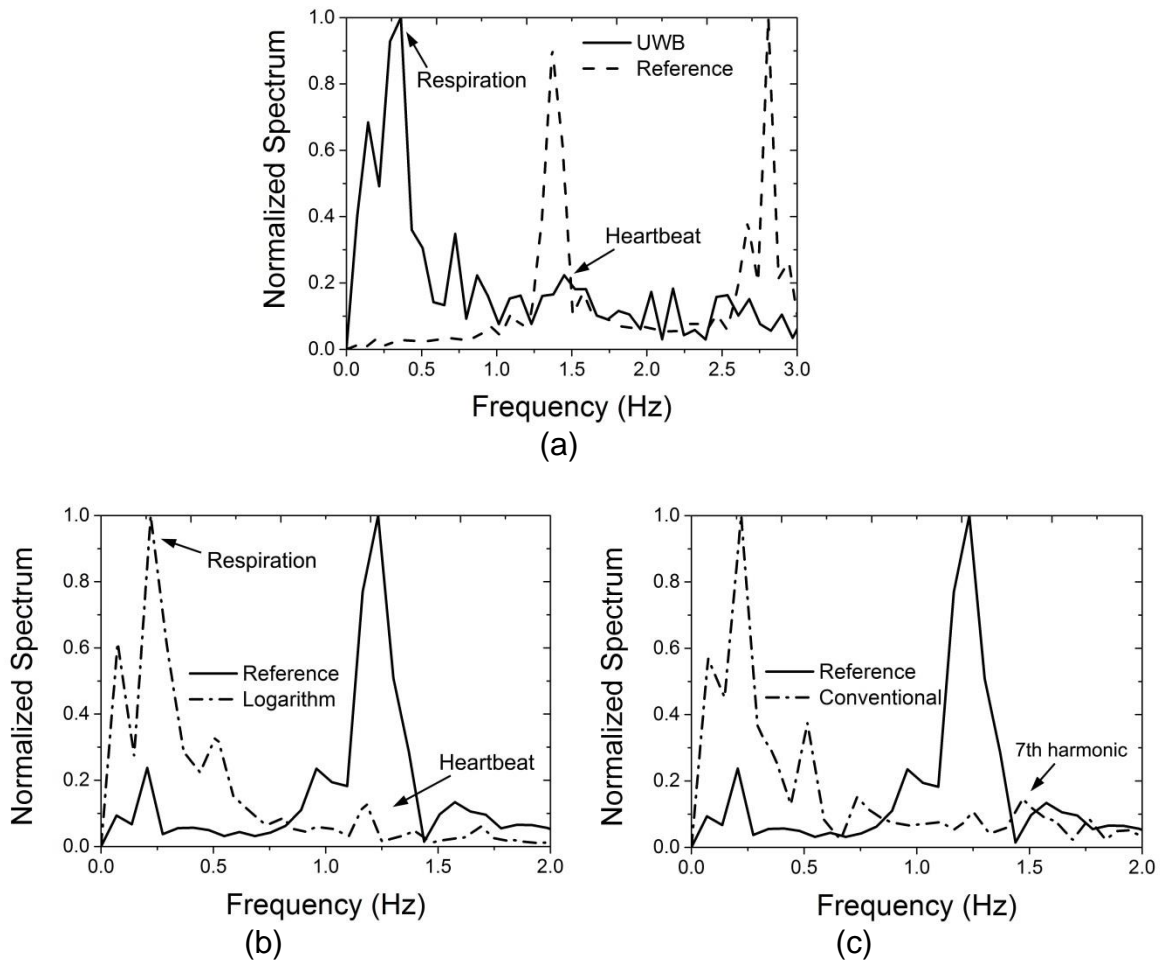


Figure 4.22 Respiration and heart rate of (a) subject 1 using logarithm method, (b) subject 2 using logarithm method, (c) subject 2 using conventional method.

4.5. Conclusion

For UWB radar system, phase-based demodulation method, i.e. logarithm method, is proposed and its mathematical formulations have been introduced as well. Experiments have demonstrated the capability of this method for UWB radar systems in heart rate detection which outperforms the conventional method by avoiding the intermodulation and high order harmonics of respiration. Additionally, experiment with two subjects has been conducted to show that UWB radar system can distinguish the vital signs of multiple subjects at the same time as well as its capability of multiple-subject localization.

CHAPTER V

CONCLUSIONS AND FUTURE WORK

In our investigation of various examples of embedded antennas we came across two topics; use of metamaterials to enhance antenna performance and use of antennas in medical applications. In the following, we will go over some of objectives in tackling these areas and our research in developing these areas. In each section, we will also identify some of needed research in the near future.

5.1. Use of Metamaterials to Enhance Antenna Performance

Magneto, dielectric materials have become the focus of several studies because of their potential to improve the radiation characteristics of antennas. It has been proven that using materials with high but comparable permeability and permittivity results in wideband miniaturized antennas, while materials with only high permittivity result in miniaturized but narrowband antennas. Even though a wideband artificial magnetic conductor (AMC) ground plane was designed using barium-cobalt hexaferrite material to work in the UHF frequency band, but natural materials with high permeability in the microwave regime are rare. Hence, the possibility to create artificial magnetism at microwave frequencies by using engineered structures is promising.

In [1], a novel application for magneto-dielectric materials was introduced. Materials with permeability higher than one are used to increase the in-phase reflection bandwidth of the mushroom-type EBGs, and the designed EBG structure is used to implement a low-profile wideband antenna. Electromagnetic bandgap (EBG) structures have been shown to emulate good magnetic conductors, or high impedance surfaces, in their in-phase reflection bandwidth when used a ground plane in the design of low-profile

antennas [2]. Most EBG structures, however, have desirable properties over a narrow frequency range, thus limiting their application in the design of low-profile wideband antennas.

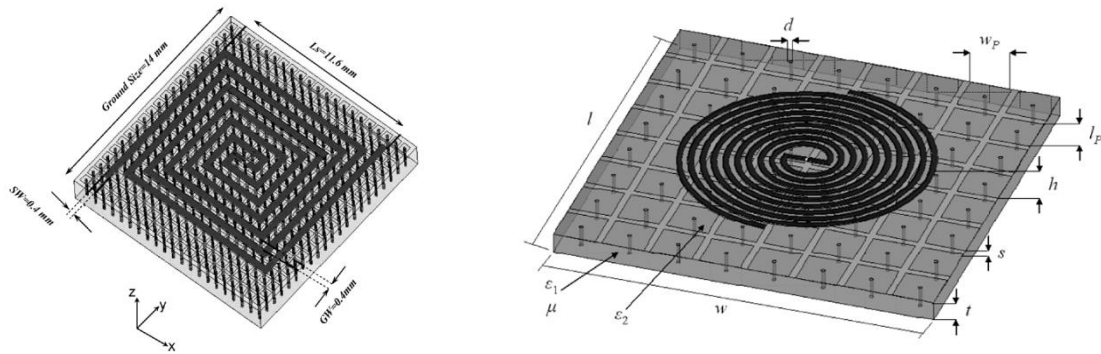


Figure 5.1 The low-profile spiral antennas above the EBG surface [1, 2].

EBG can be used to design low profile antennas, for example metallic periodic arrays typically are placed over a metallic (PEC) ground plane to enhance the directivity of simple radiating sources positioned between the array and the ground to form an open resonant cavity between the ground plane and the array that acts as a partially reflective surface (PRS). Even though a significant gain enhancement of microstrip patches and grounded waveguide apertures has been demonstrated, but the structure is close to half wavelength high to get phase reversal of the reflected signal. Alternatively, if artificial magnetic conductors (AMCs) are used to fully reflect incident waves with zero reflection phase, then novel high gain microstrip patch antenna can be built. Ref. [3] demonstrated similar gain to the cavity backed patches, but with half the height, i.e. $\lambda/4$ high.

Another implementation of electromagnetic band-gap (EBG) structures was developing an inherently wide-band Archimedean spiral antenna. The EBG structure is designed to emulate a perfect magnetic conductor. The combination of technologies produces a low-profile and wide-band antenna. Utilization of the EBG structure offers an antenna height reduction of more than 69%, including the thickness of the EBG structure, compared to the traditional $\lambda/4$ cavity backed implementation of spiral antennas. Ref. [2] demonstrated a spiral antenna maintaining a considerable fraction (71%) of its designed inherent broad-band behavior with no loss to its directive gain.

Along these lines, we developed a low profile ultrawide band tapered slot antenna covered by a superstrate, and backed by an EBG surface comprised of a reactive impedance surface RIS and a ferrite tile. The superstrate has extremely high mechanical strength for protection and will be part of an armory vehicle for example, embedded in the door or side body of an armory vehicle.

The hybrid RIS and ferrite ground plane backed by metal does not cause phase reversal over wide band (i.e. phase of reflection coefficient $<\pm 45^\circ$), improve the broadside gain, and eliminates gain drop in the middle of the operating frequency range as well. The composite ground emulates a magnetic wall and operates over wide band. Additional benefits of using of the high RIS backed by ferrite is preventing surface waves and minimizing ferrite excessive loss effects. A wide band and positive gain performances have been obtained over 1 to 4 GHz with such proposed antenna.

Even though our results are very promising, but use of the ferrite backing is still a big concern for its heavy weight, difficulty in its manufacturing or drilling holes and cost too. In the introduction, we referred to the work by [4] to multi-layer meta-materials to

address the bandwidth issue. Recently, Ref. [5] developed and used genetic programming (GP) software to synthesize true-3D artificial magnetic conductor (AMC) ground planes, with the focus on achieving a lower frequency response (particularly in the high VHF to low UHF bands), low-profile, broadband designs without the use of absorbing or magnetic materials. Metallic 3D patterns were embedded in one or more substrate layers with a PEC bottom, and the patterning in the unit cell was allowed to extend into neighboring unit cells, thus achieving a lower frequency response with much smaller unit cell size and thickness. Two designs synthesized using the developed GP software are presented with achieved bandwidths of 71.1% and 51.6% when using the $\pm 90^\circ$ reflection phase criterion. Results are very encouraging, but experimental results remain to be seen.

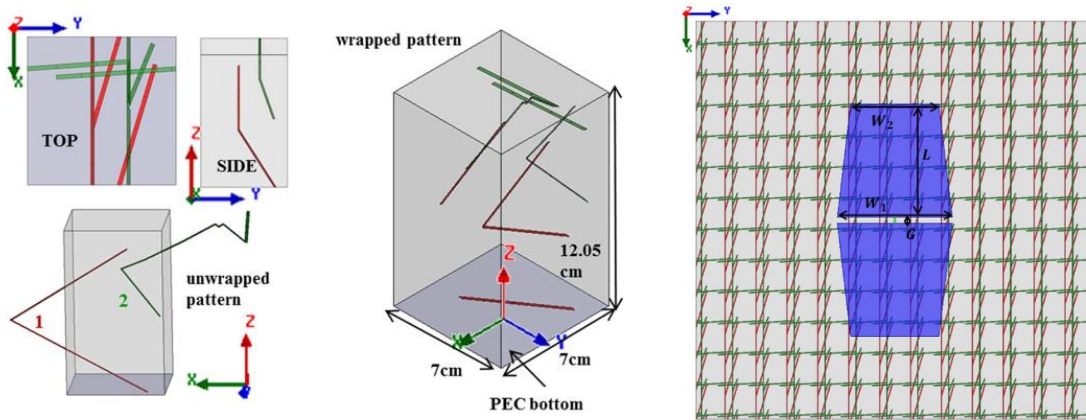


Figure 5.2 Unit cell for AMC ground and a broadband dipole antenna above it [5].

So, innovative methods for implementing metamaterials without the use of ferrites are welcome, however emphasis should be on compactness, low cost, light weight, and demonstrating positive gain over wideband.

5.2. Antenna for Medical Application

In our second example, one of the main objectives of our work in this thesis is to touch upon the feasibility of improving the performance of antennas when they are used either in contact with the subject as in hyperthermia skin cancer treatment, or as implanted antennas for medical wireless communication systems.

Various antennas have been developed for hyperthermia treatment, and it is anticipated too that ever sophisticated medical devices will be implanted inside the human body for medical telemetry and telemedicine. For focusing the energy on the cancerous cells, or to establish effective and efficient wireless links with these implanted devices, it is essential to give special attention to the antenna designs that are required to be low profile, small, safe and cost effective.

Scientists and practitioners are increasingly using radio frequency antennas inside/outside a human body for biomedical applications. Most of the research on antennas for medical applications has focused on producing hyperthermia for medical treatments and monitoring various physiological parameters. Antennas used to elevate the temperature of cancer tissues are located inside or outside of the patient's body, and the shapes of antennas used depend on their locations.

For instance in our work, we used slot antennas fed by microstrip lines and was externally positioned, others have used externally monopole or dipole antennas but were transformed to form a coaxial cable for internal use. In addition to medical therapy and diagnosis, telecommunications are regarded as important functions for implantable medical devices (pacemakers, defibrillators, etc.) which need to transmit diagnostic information. Significant success has been seen related to hyperthermia, but work on

antennas used to build the communication links between implanted devices and exterior instrument for biotelemetry are not widely reported.

It is believed that developing the biomaterials, and CAD tools for designing antennas embedded in human tissues either for treatment or communication would be greatly appreciated.

It is commonly recognized that modern wireless technology will play an important role in making telemedicine possible. In not a distant future, remote health-care monitoring by wireless networks will be a feasible treatment for patients who have chronic disease, or monitoring elderly 24/7 remotely while keeping their privacy [6].

Our developed external applicator specifically provides compact, efficient, focused, deep-penetrating, and effective clinical hyperthermia for the palliative treatment of tumor bearing patients. The newly developed compact slot antenna has been designed as applicator for hyperthermia for veterinary patients. By using an antenna with flexible silicone pads and thin substrates and designed to radiate efficiently into tissue instead on free space, the applicator can be mounted on a curved body and achieve a good match at 434MHz with insensitivity to detuning. The antenna is a good candidate to treat superficial skin cancer. Notice that the main issues in its design is its flexibility and efficiency.

It was very imperative here to develop adequate Simulation tools to indicate the electric field and power distribution and tweak the design to get favorable design. This electric field pattern demonstrates the focusing ability of the antenna through its' multi-layer construction. Directivity is further improved by adding a back shield.

The measured results were very promising as the electric field patterns of the applicator are superior to those obtained from a comparable flat microwave antenna as they are uniform over homogeneous sites. The applicator exhibits a reduced surface and backfield irradiation and improved directional irradiation along the z-axis compared to a flat slot-antenna. Similarly, the radiated power and depth of penetration of the applicator is notably increased to 5.16 cm (13.5% SAR) in comparison to 3.49 cm for the flat slot-antenna in case of mass averaged SAR (10g). During clinical applications, therapeutic temperatures were achieved at depths ≥ 4 cm. Tissue matching properties (i.e. S11 parameters) and bandwidth measurements were determined in cats, dogs, and horses. Excellent tissue matching properties were achieved with wide bandwidth of >400 MHz at better than 10 dB return loss.

One of our design concerns was the use of efficient absorbing back layer to prevent back radiation for operator safety. Here, we used a lossy material and fraction of the radiated power was lost. However, for many other applications, at higher frequency like in radar scattering reduction, typically Salisbury screen can be used to prevent energy to go through, but it could be replaced with a much thinner construction where the conventional perfectly conducting ground plane at $l=\lambda/4$ from the resistive sheet is replaced with a high impedance surface positioned at much smaller spacing from it. The absorber uses a commercially available conductive textile material uniformly coated with doped conducting polymer. The material is placed at close proximity to form an artificial magnetic ground plane that even could help in increasing the directivity by providing in phase reflection. *Use of meta-materials can be thought of for future designs [7].*

BIBLIOGRAPHY

Chapter 1. Introduction

- [1] http://www.eetimes.com/document.asp?doc_id=1271611
- [2] X. Jin and M. Ali, "Embedded antennas in dry and saturated concrete for application in wireless sensors," *Progress In Electromagnetics Research*, vol.102, 197-211, 2010.
- [3] P. Soontornpipit, C. M. Furse and C. You Chung, "Design of implantable microstrip antenna for communication with medical implants," *IEEE Trans. Microwave Theory Tech.*, vol.52, no.8, pp.1944 -1951 2004.
- [4] Deffendol and C. Furse,"Microstrip antennas for dielectric property measurement," *IEEE AP/URSI Int. Symp. Dig.*, vol.3, pp.1954 -1957 1999.
- [5] J. Bahl and S. S. Stuchly, "Analysis of a microstrip covered with a lossy dielectric," *IEEE Trans. Microwave Theory Tech.*, vol.MTT-28, pp.104–109, Feb. 1980.
- [6] M. Furse, "A meander antenna used as a human proximity sensor," Mission Res. Inc., Logan, UT, Final Rep., July 1998.
- [7] N. Madan, "Imbedded antennas for the measurement of electrical properties of materials," M.S. thesis, Dept. Elect. Comput. Eng., Utah State Univ., Logan, UT, 2001.
- [8] Johnson, E. Cherkaev, C. Furse, and A. Tripp, "Cross-borehole delineation of a conductive ore deposit—Experimental design," *Geophysics*, vol.66, no.3, pp.824–835, 2001.
- [9] Johnson, C. Furse, and A. Tripp, "FDTD modeling and validation of EM survey tools," *Microwave Opt. Technol. Lett.*, vol.34, no.6, pp.427 -429 2002.
- [10] P. S. Debroux,"Modeling of the electromagnetic response of geophysical targets using the (FDTD) method," *Geophys. Prospecting*, vol.44, no.3, pp.457 -468 1996.
- [11] R. D. Nevels, D. Arndt, J. Carl, G. Raffoul, and A. Pacifico, "Microwave antenna design for myocardial tissue ablation applications," *IEEE AP-S Int. Symp. Dig.*, vol.3, pp.1572 1995.
- [12] S. Manolis, P. J. Wang, and N. A. Estes, "Radio frequency catheter ablation for cardiac tachyarrhythmias," *Annu. Int. Med.*, vol.121, no.6, pp.452 -461 1994.
- [13] Rosen,"Microwave applications in cancer therapy, cardiology and measurement techniques: A short overview," *IEEE MTT-S Newslett.*, pp.17 -20 1990.
- [14] Guy, J. F. Lehman, and J. B. Stonebridge, "Therapeutic applications of electromagnetic power," *Proc. IEEE*, vol.62, pp.55 -75 1974.
- [15] M. F. Iskander, A. M. Tumeh, and C. M. Furse, "Evaluation and optimization of the EM characteristics of interstitial antennas for hyperthermia," *Int. J. Radiat., Oncol., Biol., Phys.*, vol.18, no.4, pp.895 -902 1990.

- [16] M. Furse and M. F. Iskander, "Three-dimensional electromagnetic power deposition in tumors using interstitial antenna arrays," *IEEE Trans. Biomed. Eng.*, vol.36, pp.977 -986 1989.
- [17] P. C. Cherry and M. F. Iskander, "Calculations of heating patterns of an array of microwave interstitial antennas," *IEEE Trans. Biomed. Eng.*, vol.40, pp.771 -779 1993.
- [18] Bonefačić, S. Hrabar and D. Kvakar, "Experimental investigation of radiation properties of an antenna embedded in low-permittivity thin-wire-based metamaterials," *Microw. Opt. Technol. Lett.*, vol.48, no.12, pp.2581 -2586 2006.
- [19] W. Rotman, "Plasma simulation by artificial dielectrics and parallel-plate media," *Antennas and Propagation, IRE Transactions on*, vol.10, no.1, pp.82,95, January 1962.
- [20] J. B. Pendry, A. J. Holden, D. J. Robbins, W. J. Stewart, "Low frequency plasmons in thin-wire structures," *Journal of Physics: Condensed Matter*, vol.10, no.22, 1998.
- [21] S. Enoch , G. Tayeb , P. Sabouroux , N. Gurin and P. Vincent, "A metamaterial for directive emission," *Phys. Rev. Lett.*, vol.89, 2002
- [22] G. Lovat, P. Burghignoli, F. Capolino, D. R. Jackson, D. R. Wilton, "Analysis of directive radiation from a line source in a metamaterial slab with low permittivity," *Antennas and Propagation, IEEE Transactions on* , vol.54, no.3, pp.1017,1030, March 2006.
- [23] M. Fallah-Rad, and L. Shafai, "Gain enhancement in embedded microstrip antennas," *Microw. Opt. Technol. Lett.*, vol.50 no.2, pp.269–271 2008.
- [24] M.S. Sharawi, D.N. Aloï, O.A. Rawashdeh, "Design and Implementation of Embedded Printed Antenna Arrays in Small UAV Wing Structures," *Antennas and Propagation, IEEE Transactions on*, vol.58, no.8, pp.2531, 2538, Aug. 2010.
- [25] R. L. Cravey *et al.*, "Structurally Integrated antenna concepts for Hale UAVs," NASA Langley Research Center, 2006, NASA/TM-2006-214513.
- [26] L. M. Hilliard *et al.*, "Lightweight linear broadband antennas enabling small UAV wing systems and space flight nanosat concept," in *Proc.IEEE Int. Geoscience and Remote Sensing Symp.*, Sep. 2004.
- [27] N. Chamberlain *et al.*, "The UAVSAR phased array aperture," presented at the IEEE Aerospace Conf., Mar. 2006.
- [28] Quintero *et al.*, "MSAG based MAE-UAV active array antennas," in *Proc. IEEE Radar Conf.*, pp.393–397, May 2001.
- [29] H. Tsuji *et al.*, "Radio location estimation experiment using array antennas for high altitude platforms," in *Proc. 18th Annual IEEE Int. Symp. on Personal, Indoor, and Mobile Radio Communications*, pp.1–5, Sep. 2007.

- [30] S. Jenvey, J. Gustafsson, and F. Henriksson, "A portable monopulse tracking antenna for UAV communications," in *Proc. 22nd Int. Unmanned Air Vehicle Systems Conf.*, pp.1–8, Apr. 2007.
- [31] L. Gezer *et al.*, "Digital tracking array using off-the-shelf hardware," *IEEE Antennas Propag. Mag.*, vol.50, no.1, pp.108–114, Feb. 2008.
- [32] Y. L. Kuo and K. L. Wong, "Printed double-T monopole antenna for 2.4/5.2 GHz dual-band WLAN operations," *IEEE Trans. Antennas Propag.*, vol.51, pp.2187–2192, Sep. 2003.
- [33] H. M. Chen and Y. F. Lin, "Printed monopole antenna for 2.4/5.2 GHz dual-band operation," in *Proc. IEEE Int. Symp. on Antennas and Propagation*, vol.3, pp.60–63 Jun. 2003.
- [34] S.G. Zhou, B.H. Sun, Y.F. Wei, Q.Z. Liu, "Low profile wideband antenna with shaped beams for indoor DVB-H applications," *Electronics Letter*, vol.45, no.23, pp.1151, 1152, November 2009.
- [35] Haksu Moon, Gil-Young Lee, Chi-Chih Chen, J. L. Volakis, "An Extremely Low-Profile Ferrite-Loaded Wideband VHF Antenna Design," *Antennas and Wireless Propagation Letters, IEEE*, vol.11, no., pp.322,325, 2012.
- [36] Nakano, H.; Satake, R.; Yamauchi, J., "Extremely Low-Profile, Single-Arm, Wideband Spiral Antenna Radiating a Circularly Polarized Wave," *Antennas and Propagation, IEEE Transactions on*, vol.58, no.5, pp.1511-1520, May 2010.
- [37] Jungsuek Oh, K. Sarabandi, "Low Profile Vertically Polarized Omnidirectional Wideband Antenna with Capacitively Coupled Parasitic Elements," *Antennas and Propagation, IEEE Transactions on*, vol.62, no.2, pp.977-982, Feb. 2014.
- [38] Gibbins, M. Klemm, I. Craddock, J. Leendertz, A. Preece, and R. Benjamin, "A comparison of a wide-slot and a stacked patch antenna for the purpose of breast cancer detection," *IEEE Trans. Antennas Propag.*, vol.58, no.3, pp.665-674, Mar. 2010.
- [39] Y. Yang, Y. Wang, A.E. Fathy, "Design of Compact Vivaldi Antenna Arrays for UWB See Through Wall Applications," *Progress In Electromagnetics Research*, PIER 82, pp.401- 418, 2008.
- [40] Elsherbini, and K. Sarabandi, "UWB high-isolation directive coupled-sectorial-loops antenna pair," *IEEE Antennas Wireless Propag. Lett.*, vol.10, pp.215-218, 2011.
- [41] K. Browne, R. Burkholder, and J. Volakis, "Through-wall radar imaging system utilizing a light-weight low-profile printed array," in *2010 4th European Antennas and Propag.*, pp.606-609, Barcelona, Spain, Apr. 2010.

Chapter 2

- [1] P. R. Stauffer, "Evolving technology for thermal therapy of cancer," *International Journal of Hyperthermia*, vol.21, no.8, pp.731–744, Dec. 2005.
- [2] J. Keshvari, R. Keshvari, and S. Lang, "The effect of increase in dielectric values on specific absorption rate (SAR) in eye and head tissue following 900, 1800, 2450 MHz radio frequency (RF) exposure," *Physics in Medicine and Biology*, vol.51, no.6, pp.1463-1477, Mar. 2006.
- [3] V. L. Stakhursky, O. Arabe, K. S. Cheng, J. MacFall, P. Maccarini, O. Craciunescu, M. Dewhurst, P. R. Stauffer, and S. K. Das, "Real-time MRI-guided hyperthermia treatment using a fast adaptive algorithm," *Physics in Medicine and Biology*, vol.54, no.1, pp.2131-2145, Mar. 2009
- [4] W. T. Joines, Y. Zhang, C. Li, and R. L. Jirtle, "The measured electrical properties of normal and malignant human tissues from 50 to 900 MHz," *Medical Physics*, vol.21, no.4, pp.547-550, Apr. 1994.
- [5] IEEE Recommended practice for measurements and computations of radio frequency electromagnetic fields with respect to human exposure to such fields, 100 kHz - 300 GHz, IEEE Std. C95.3-2002 (Revision of IEEE Std. C95.3-1991), 2002.
- [6] M. M. Paulides, J. F. Bakker, N. Chavailles, and G. C. Van Rhoon, "A patch antenna design for application in a phased-array head and neck hyperthermia applicator," *IEEE Transactions on Biomedical Engineering*, vol.54, no.11, pp.2057-2063, Nov. 2007.
- [7] J.-C. Lin, G. Kantor, and A. Ghods. A class of new microwave therapeutic applicators. *Radio Science*, 17:119S–123S, 1981.
- [8] R. L. Magin and A. F. Peterson. Noninvasive microwave phase arrays for local hyperthermia: a review. *International Journal of Hyperthermia*, vol.5, no.4, pp.429–450, 1989.
- [9] G. A. Lovisolo, M. Adami, G. Arcangeli, and A. Borroni, "A multifrequency water-filled waveguide application thermal dosimetry in vivo," *IEEE Transactions on Microwave Theory and Techniques*, vol.32, no.8, pp.893– 896, Aug. 1984.
- [10] M. Krairiksh, C. Thongsopa, D. Srimoon, and A. Mearnchu, "Analysis and design of injection-locking steerable active array applicator," *IEICE Transactions on Communications*, E85-B(10):2327–2337, 1999.
- [11] T. Samaras, P. J. M. Rietveld, and G. C. van Rhoon, "Effectiveness of FDTD in predicting SAR distributions from the Lucite cone applicator," *IEEE Transactions on Microwave Theory and Techniques*, vol.48, no.11, pp.2059–2063, Nov. 2000.

- [12] P. J. M. Rietveld, W. L. J. van Putten, J. van der Zee, and G. C. van Rhoon, "Comparison of the clinical effectiveness of the 433 MHz Lucite cone applicator with that of a conventional waveguide applicator in applications of superficial hyperthermia," *International Journal of Radiation Oncology, Biology, Physics*, vol.43, pp.681–687, Feb. 1999.
- [13] R. C. Gupta and S. P. Singh, "Analysis of the SAR distributions in three-layered bio-media in direct contact with a water-loaded modified box-horn applicator," *IEEE Transactions on Microwave Theory and Techniques*, vol.53, no.9, pp.2665–2671, Sep. 2005.
- [14] R. C. Gupta and S. P. Singh, "SAR characterization of focused planar array of water-loaded modified box-horns for hyperthermia," *International Journal of Infrared and Millimeter Waves*, vol.27, no.2, pp.273–291, Feb. 2006.
- [15] R. C. Gupta and S. P. Singh, "Mutual coupling between box-horn elements of a phased array terminated in three-layered bio-media," *IEEE Transactions on Antennas and Propagation*, vol.55, no.8, pp.2219–2227, Aug. 2007.
- [16] M. A. Ebrahimi-Ganjeh and A. R. Attari, "Study of water bolus effect on SAR penetration depth and effective field size for local hyperthermia," *Progress In Electromagnetics Research*, vol.4, pp.273–283, 2008.
- [17] H. R. Underwood, A. F. Peterson, and R. L. Magin, "Electric-field distribution near rectangular microstrip radiators for hyperthermia heating: theory versus experiment in water," *IEEE Transactions on Biomedical Engineering*, vol.39, no.2, pp.146–153, Feb. 1992.
- [18] J. Bahl, S. S. Stuchly, J. W. Lagendijk, and M. A. Stuchly, "Microstrip loop radiators for local hyperthermia," *MTT-S International Microwave Symposium Digest*, vol.81, no.1, pp.465–467, June 1981.
- [19] F. Montecchia, "Microstrip-antenna design for hyperthermia treatment of superficial tumors," *IEEE Transactions on Biomedical Engineering*, vol.39, no.6, pp.580–588, June 1992.
- [20] E. R. Lee, T. R. Wilsey, P. Tarczy-Hornoch, D. S. Kapp, P. Fessenden, A. Lohrbach, and S. D. Prionas, "Body conformable 915 MHz microstrip array applicators for large surface area hyperthermia," *IEEE Transactions on Biomedical Engineering*, vol.39, no.5, pp.470–483, May 1992.
- [21] BSD Medical Corporation, <http://www.bsdmc.com/>.
- [22] R. H. Johnson, A. W. Preece, J. W. Hand, and J. R. James, "A new type of lightweight low-frequency electromagnetic hyperthermia applicator," *IEEE Transactions on Microwave Theory and Techniques*, vol.35, no.12, pp.1317–1321, Dec. 1987.
- [23] M. V. Prior, M. L. D. Lumori, J. W. Hand, G. Lamaitre, C. J. Schneider, and J. D. P. van Dijk, "The use of a current sheet applicator array for superficial

- hyperthermia: incoherent versus coherent operation,” *IEEE Transactions on Biomedical Engineering*, vol.42, no.7, pp.694–698, July 1995.
- [24] W. Guy, “Electromagnetic fields and relative heating patterns due to a rectangular aperture source in direct contact with bilayered biological tissue,” *IEEE Trans. Microw. Theory Tech.*, vol.19, no.2, pp.214–223, Feb. 1971.
- [25] K. S. Nikita and N. K. Uzunoglu, “Analysis of the power coupling from a waveguide hyperthermia applicator in a three-layered tissue model,” *IEEE Trans. Microw. Theory Tech.*, vol.37, no.11, pp.1794–1801, Nov. 1989.
- [26] T. Samaras, P. J. M. Rietveld, and G. C. van Rhoon, “Effectiveness of FDTD in predicting SAR distributions from the Lucite cone applicator,” *IEEE Trans. Microw. Theory Tech.*, vol.48, no.11, pt. 2, pp.2059–2063, Nov. 2000.
- [27] R. C. Gupta and S. P. Singh, “Analysis of the SAR distributions in three-layered bio-media in direct contact with a water-loaded modified box-horn applicator,” *IEEE Trans. Microw. Theory Tech.*, vol.53, no.9, pp.2665–2671, Sep. 2005.
- [28] I. J. Bahl, S. S. Stuchly, J. W. Lagendijk, and M. A. Stuchly, “Microstrip loop radiators for local hyperthermia,” *IEEE MTT-S Int. Microw. Symp. Dig.*, pp.465–467, Jun. 1981.
- [29] D. Andreuccetti, M. Bini, A. Ignesti, R. Olmi, S. Priori, and R. Vanni, “High permittivity patch radiator for single and multi-element hyperthermia applicators,” *IEEE Trans. Biomed. Eng.*, vol.40, pp.711–715, Jul. 1993.
- [30] E. A. Celvich and V. N. Mazokhin, “Contact flexible microstrip applicator (CFMA) in a range from microwaves up to short waves,” *IEEE Trans. Biomed. Eng.*, vol.49, pp.1015–1023, Sep. 2002
- [31] S. Curto, and M. J. Ammann, “Electromagnetic interaction between resonant loop antenna and simulated biological tissue,” *Microw. Opt. Technol. Lett.*, vol.48, no 12, pp.2418–2421.
- [32] T. Drizdal, P. Togni, J. Vrba, “Microstrip Applicator for Local Hyperthermia,” *Electromagnetics in Advanced Applications, 2007. ICEAA 2007. International Conference on*, vol., no., pp.1047,1049, 17–21 Sept. 2007
- [33] J. Safarik, J.; Jan Vrba, “Slotted Applicator for Microwave Local Hyperthermia,” *Microwave Techniques, 2008. COMITE 2008. 14th Conference on*, vol., no., pp.23–24 April 2008.
- [34] S. Curto, P. McEvoy, X. Bao, M. J. Ammann, “Compact patch antenna for electromagnetic interaction with human tissue at 434 MHz,” *IEEE Trans. Ant. Propag.*, vol.57, no.9, pp.2564–2571, Sept. 2009.
- [35] P. Stauffer, J. Schlorff, R. Taschereau, T. Juang, D. Neuman, P. Maccarini, J. Pouliot, and J. Hsu. Combination applicator for simultaneous heat and radiation. *In Annual International Conference of the IEEE Engineering in Medicine and Biology Society*, volume 1, pages 2514–2517, Sep. 2004.

- [36] P. Wust, B. Hildebrandt, G. Sreenivasa, B. Rau, J. Gellermann, H. Riess, R. Felix, and P. M. Schlag, "Hyperthermia in combined treatment of cancer," *Lancet Oncol.*, vol.3, no.8, pp.487-497, Aug. 2002.
- [37] J. van der Zee, "Heating the patient: A promising approach?," *Annal. Oncol.*, vol.13, no.8, pp.1173-1184, May 2002.
- [38] G. Wang, and Y. Gong, "Metamaterial lens applicator for microwave hyperthermia of breast cancer," *Int. J. of Hyperthermia*, vol.25, no.6, pp.434-445, Jan. 2009.
- [39] R. Antolini, G. Cerri, L. Cristoforetti, and R. De Leo, "Absorbed power distributions from single or multiple waveguide applicators during microwave hyperthermia," *Phys. Med. Biol.*, vol.31, pp.1005-1019, 1986.
- [40] M. D. Sherar, H. Clark, B. Cooper, J. Kumaradas, and F. F. Liu, "A variable microwave array attenuator for use with single-element waveguide applicators," *Int. J. Hyperthermia*, vol.10, no.5, pp.723-731, 1994.
- [41] T. Juang, D. Neuman, J. Schlorff, and P. R. Stauffer, "Construction of a conformal water bolus vest applicator for hyperthermia treatment of superficial skin cancer," *26th Annual IEEE Int. Conf. Eng. Medicine Biology Soc.*, vol.2, pp.3467-3470, Sep. 2004.
- [42] F. Montecchia, "Microstrip-antenna design for hyperthermia treatment of superficial tumors," *IEEE Trans. Biomed. Eng.*, vol.39, no.6, pp.580-588, Jun. 1992.
- [43] H. Kok, Petra, M. De Greef, D. Correia, P. J. Zum Vörde Sive Vörding, G. Van Stam, E. A. Gelvich, A. Bel, and J. Crezee, "FDTD simulations to assess the performance of CFMA-434 applicators for superficial hyperthermia," *Int J. Hyperthermia*, vol.25, no.6, pp.462-476, 2009.
- [44] L. H. Lindner, and R. D. Issels, "Hyperthermia in soft tissue sarcoma," *Current Treatment Options in Oncology*, vol.12, no.1, pp.12-20, 2011.
- [45] S. Gabriel, R. W. Lau and C. Gabriel, "The dielectric properties of biological tissues: II. Measurements in the frequency range 10 Hz to 20 GHz," *Physics in Medicine and Biology*, vol.41, no.11, pp.2251-2269, Nov. 1996.
- [46] J. E. Johnson, D. G. Neuman, P. F. Maccarini, T. Juang, P. R. Stauffer, and P. Turner, "Evaluation of a dual-arm Archimedean spiral array for microwave hyperthermia," *Int. J. Hyperthermia*, vol.22, pp.475-490, 2006.
- [47] T. Drizdal, M. Vrba, M. Cifra, P. Togni, and J. Vrba, "Feasibility study of superficial hyperthermia treatment planning Using COMSOL Multiphysics," *14th Conf. Microw. Tech.*, pp.1-3, April 2008.
- [48] W. Guy, "Electromagnetic fields and relative heating patterns due to a rectangular aperture source in direct contact with bilayered biological tissue," *IEEE Trans. Microw. Theory Tech.*, vol.19, no.2, pp.214-223, Feb. 1971.

- [49] K. S. Nikita and N. K. Uzunoglu, "Analysis of the power coupling from a waveguide hyperthermia applicator in a three-layered tissue model," *IEEE Trans. Microw. Theory Tech.*, vol.37, no.11, pp.1794-1801, 1989.
- [50] T. Samaras, P. J. M. Rietveld, and G. C. van Rhoon, "Effectiveness of FDTD in predicting SAR distributions from the Lucite cone applicator," *IEEE Trans. Microw. Theory Tech.*, vol.48, no.11, pp.2059-2063, 2000.
- [51] R. C. Gupta and S. P. Singh, "Analysis of the SAR distributions in three-layered bio-media in direct contact with a water-loaded modified box-horn applicator," *IEEE Trans. Microw. Theory Tech.*, vol.53, no.9, pp.2665-2671, Sep. 2005.
- [52] I. J. Bahl, S. S. Stuchly, J. W. Lagendijk, and M. A. Stuchly, "Microstrip loop radiators for local hyperthermia," *IEEE MTT-S Int. Microw. Symp. Dig.*, pp.465-467, Jun. 1981.
- [53] D. Andreuccetti, M. Bini, A. Ignesti, R. Olmi, S. Priori, and R. Vanni, "High permittivity patch radiator for single and multi-element hyperthermia applicators," *IEEE Trans. Biomed. Eng.*, vol.40, pp.711-715, Jul. 1993.
- [54] E. A. Celvich and V. N. Mazokhin, "Contact flexible microstrip applicator (CFMA) in a range from microwaves up to short waves," *IEEE Trans. Biomed. Eng.*, vol.49, pp.1015-1023, Sep. 2002.
- [55] S. Curto, and M. J. Ammann, "Electromagnetic interaction between resonant loop antenna and simulated biological tissue," *Microw. Opt. Technol. Lett.*, vol.48, no 12, pp.2418-2421, 2006.
- [56] T. Drizdal, P. Togni, and J. Vrba, "Microstrip Applicator for Local Hyperthermia," *Int. Conf. Electromagnetics in Advanced Applications (ICEAA)*, pp.1047-1049, Sept. 2007.
- [57] J. Safarik, and J. Vrba, "Slotted Applicator for Microwave Local Hyperthermia," *14th Conf. Microw. Tech. (COMITE)*, pp.23-24, 2008.
- [58] S. Curto, P. McEvoy, X. Bao, and M. J. Ammann, "Compact patch antenna for electromagnetic interaction with human tissue at 434 MHz," *IEEE Trans. Ant. Propag.*, vol.57, no.9, pp.2564-2571, Sept. 2009.
- [59] P. Wust, H. Föhling, W. Wlodarczyk, M. Seebass, J. Gellermann, P. Deuflhard, and J. Nadobny, "Antenna arrays in the SIGMA-Eye applicator: Interactions and transforming networks," *Med. Phys.*, vol.28, no.8, pp.1793-1805, Aug. 2001.
- [60] M. M. Paulides, J. F. Bakker, N. Chavannes, and G. C. Van Rhoon, "A patch antenna design for application in a phased-array head and neck hyperthermia applicator," *IEEE Trans. Biomed. Eng.*, vol.54, pp.2057- 2063, Nov. 2007.
- [61] K. M. Jones, J. A. Mechling, J. W. Strohbehn, and B. S. Trembly, "Theoretical and experimental SAR distributions for interstitial dipole antenna arrays used in hyperthermia," *IEEE Trans. Microw. Theory Tech.*, vol.37, no.8, pp.1200-1209, Aug 1989.

- [62] C.-K. Chou, "Evaluation of microwave hyperthermia applicators," *Bioelectromag.*, vol.13, no.6, pp.581-597, Jun. 1992.
- [63] D. Correia, H. P. Kok, M. de Greef, A. Bel, N. van Wieringen, and J. Crezee, "Body conformal antennas for superficial hyperthermia: The impact of bending contact flexible microstrip applicators on their electromagnetic behavior," *IEEE Trans. Biomed. Eng.*, vol.56, no.12, pp.2917-2926, Dec. 2009.
- [64] N. Siauve, L. Nicolas, C. Vollaie, A. Nicolas, and J. A. Vasconcelos, "optimization of 3-D SAR distribution in local RF hyperthermia," *IEEE Trans. Magnetics*, vol.40, no.2, pp.1264-1267, 2004.
- [65] A. V. Vorst, A. Rosen, and Y. Kotsuka, *RF/Microwave Interaction with Biological Tissues*, New Jersey, J. Wiley, 2006.
- [66] P. H. Schwan, K. Li, "Capacity and Conductivity of Body Tissues at Ultrahigh Frequencies," *Proc. IRE*, vol.41, no.12, pp.1735-1740, 1953.
- [67] M. Lazebnik, M. C. Converse, J. H. Booske, and S. C. Hagness, "Ultra- wideband temperature-dependent dielectric properties of animal liver tissue in the microwave frequency range," *Phys. Med. Biol.*, vol.51, pp.1941-1955, 2006.
- [68] O. A. Smrkovski, Y. Koo, R. Kazemi, L. M. Lembcke, A. Fathy, Q. Liu, and J. C. Phillips, "Performance characteristics of a conformal ultra-wideband multilayer applicator (CUMLA) for hyperthermia in veterinary patients: a pilot evaluation of its use in the adjuvant treatment of non-resectable tumours," *Veterinary and Comparative Oncology*, vol.11, no.1, pp.14–29, 2013.
- [69] C. Gabriel, S. Gabriel, and E. Corthout, "The dielectric properties of biological tissues: I. Literature survey," *Phys. Med. Biol.*, vol.41, pp.2231-2249, 1996.
- [70] C. Gabriel, "Compilation of the dielectric properties of body tissues at RF and microwave frequencies," *Brooks Air Force Technical Report AL/OE-TR-1996-0037*, 1996.
- [71] <http://www.speag.com/products/dasy/dasy-systems/>

Chapter 3

- [1] R. Chair, A. A. Kishk, K.-F. Lee, C. E. Smith, and D. Kajfez, "Microstrip line and CPW FED ultra wideband slot antennas with u-shaped tuning stub and reflector," *Progress In Electromagnetics Research*, vol.56, pp.163-182, 2006.
- [2] Bell, J.M.; Iskander, M.F.; Lee, J.J., "Ultrawideband Hybrid EBG/Ferrite Ground Plane for Low-Profile Array Antennas," *Antennas and Propagation, IEEE Transactions on* , vol.55, no.1, pp.4-12, Jan. 2007.
- [3] Rayno, J.T.; Nakatsu, J.S.K.; Gui Chao Huang; Celik, N.; Iskander, M.F., "3D metamaterial broadband ground plane designed using genetic programming for the long slot array antenna," *Antennas and Propagation Society International Symposium (APSURSI)*, 2013 IEEE , vol., no., pp.400-401, 7-13 July 2013.
- [4] D. Sievenpiper, L. Zhang, R. Broas, N. Alexopolous, and E. Yablonóvitch, *IEEE Transactions on Microwave Theory and Techniques*, Vol.47, no.11, Nov. 1999.
- [5] Zhou, S.G.; Sun, B.H.; Wei, Y.F.; Liu, Q.Z., "Low profile wideband antenna with shaped beams for indoor DVB-H applications," *Electronics Letters* , vol.45, no.23, pp.1151,1152, November 2009.
- [6] Haksu Moon; Gil-Young Lee; Chi-Chih Chen; Volakis, J.L., "An Extremely Low-Profile Ferrite-Loaded Wideband VHF Antenna Design," *Antennas and Wireless Propagation Letters, IEEE* , vol.11, no., pp.322,325, 2012.
- [7] Nakano, H.; Satake, R.; Yamauchi, J., "Extremely Low-Profile, Single-Arm, Wideband Spiral Antenna Radiating a Circularly Polarized Wave," *Antennas and Propagation, IEEE Transactions on* , vol.58, no.5, pp.1511,1520, May 2010.
- [8] Jungsuek Oh; Sarabandi, K., "Low Profile Vertically Polarized Omnidirectional Wideband Antenna With Capacitively Coupled Parasitic Elements," *Antennas and Propagation, IEEE Transactions on* , vol.62, no.2, pp.977,982, Feb. 2014.
- [9] Jia-Yi Sze; Kin-Lu Wong, "Bandwidth enhancement of a microstrip-line-fed printed wide-slot antenna," *Antennas and Propagation, IEEE Transactions on* , vol.49, no.7, pp.1020,1024, Jul 2001.
- [10] X. Zhang, Y.-Y. Xia, J. Chen, and W.-T. Li, "Compact microstrip-fed antenna for ultra-wideband applications," *Progress In Electromagnetics Research Letters*, Vol.6, 11-16, 2009.
- [11] Azim, R.; Islam, M.T.; Misran, N., "Compact Tapered-Shape Slot Antenna for UWB Applications," *Antennas and Wireless Propagation Letters, IEEE*, vol.10, no., pp.1190-1193, 2011.
- [12] R. Chair, A. A. Kishk, K.-F. Lee, C. E. Smith, and D. Kajfez, "Microstrip line and CPW fed ultra wideband slot antennas with u-shaped tuning stub and reflector," *Progress In Electromagnetics Research*, Vol.56, 163-182, 2006.

- [13] J. M. Bell, M. F. Iskander, J. J. Lee, "Ultrawideband Hybrid EBG/Ferrite Ground Plane for Low-Profile Array Antennas," *Antennas and Propagation, IEEE Transactions on*, vol.55, no.1, pp.4-12, Jan. 2007.
- [14] Radway, M.J.; Filipovic, D.S., "Four-Armed Spiral-Helix Antenna," *Antennas and Wireless Propagation Letters, IEEE*, vol.11, no., pp.338-341, 2012.
- [15] Y. Wang, A. E. Fathy, M. R. Mahfouz, "Novel compact tapered microstrip slot antenna for microwave breast imaging," *IEEE Antennas and propagation international symposium*, 2011, pp.2219-2122.
- [16] F. Yang, Rahmat-Samii, Y., "Reflection phase characterizations of the EBG ground plane for low profile wire antenna applications," *Antennas and Propagation, IEEE Transactions on*, vol.51, no.10, pp.2691- 2703, Oct. 2003.
- [17] R. Azim, M. T. Islam, N. Misran,"Compact Tapered-Shape Slot Antenna for UWB Applications," *Antennas and Wireless Propagation Letters, IEEE*, vol.10, no., pp.1190-1193, 2011.
- [18] J. Gibson, "The Vivaldi aerial," *Proc. 9th European Microwave Conf.*, Brighton, U.K., 1979, pp.101-105.

Chapter 4

- [1] V. Jain, S. Sundararaman, and P. Heydari, "A 22-29GHz UWB pulse-radar receiver frontend in 0.18- μ m CMOS," *IEEE Trans. Microw. Theory Tech.*, vol.57, no.8, pp.1903-1914, Aug. 2009.
- [2] I. Gresham et al., "Ultra-wideband radar sensors for short-range vehicle applications," *IEEE Trans. Microw. Theory Tech.*, vol.52, no.9, pp.2105-2122, Sep. 2004.
- [3] Brian Yamauchi, "Daredevil: ultra-wideband radar sensing for small UGVs," *Proc. of SPIE*, vol.6561, May 2007.
- [4] Comlab Inc. Final Report, Ultra-wideband radar through-wall measurements, Jun. 2003.
- [5] B. R. Crowgey, E. J. Rothwell, and L. C. Kempel, "Comparison of UWB short-pulse and stepped-frequency radar systems for imaging through barriers," *Progress In Electromagnetics Research*, vol.110, pp.403-419, 2010.
- [6] D. Gibbins, M. Klemm, I. Craddock, J. Leendertz, A. Preece, and R. Benjamin, "A comparison of a wide-slot and a stacked patch antenna for the purpose of breast cancer detection," *IEEE Trans. Antennas Propag.*, vol.58, no.3, pp.665-674, Mar. 2010.
- [7] Y. Yang, Y. Wang, A.E. Fathy, "Design of Compact Vivaldi Antenna Arrays for UWB See Through Wall Applications," *Progress In Electromagnetics Research*, PIER 82, pp.401-418, 2008.
- [8] A. Elsherbini, and K. Sarabandi, "UWB high-isolation directive coupled-sectorial-loops antenna pair," *IEEE Antennas Wireless Propag. Lett.*, vol.10, pp.215-218, 2011.
- [9] K. Browne, R. Burkholder, and J. Volakis, "Through-wall radar imaging system utilizing a light-weight low-profile printed array," in *2010 4th European Antennas and Propag*, pp.606-609, Barcelona, Spain, Apr. 2010.
- [10] M. M. Zinieris et al., "A broadband microstrip-to-slot-line transition," *Microwave and Optical Technology Letters*, Vol.18, No.5, Aug. 1998.
- [11] S.B. Cohn, "A Class of Broadband Three-Port TEM-Mode Hybrids," *IEEE Trans.Microwave Theory and Tech.*, vol.MTT-16, No.2, pp.110-116, Feb. 1968.
- [12] M. Farwell, J. Ross, R. Luttrell, D. Cohen, W. Chin, and T. Dogaru, "Sense through the wall system development and design considerations," *Journal of The Franklin Institute*, 345, pp.570-591, Sep. 2008.
- [13] Inigo Cuinas et al., "Permittivity and conductivity measurements of building materials at 5.8 GHz and 41.5 GHz," *Wireless Personal Communications*, pp.93-100, 2002.

- [14] Y. Wang, A. E. Fathy, "Advanced System Level Simulation Platform for Three-Dimensional UWB Through-Wall Imaging SAR Using Time-Domain Approach," *Geoscience and Remote Sensing, IEEE Transactions on* , vol.50, no.5, pp.1986,2000, May 2012
- [15] C. A. Balanis, *Advance Engineering Electromagnetics*, New York: Van Nostrand Reinhold, 1990.
- [16] Y. Wang, Q. Liu, and A.E. Fathy, "Simultaneous localization and respiration detection of multiple people using low cost UWB biometric pulse Doppler radar sensor," *IEEE MTT-S Int. Microwave Symp. Dig.*, pp.1-3, Jun. 2012.
- [17] Y. Wang, Q. Liu, and A. E. Fathy, "CW and pulse-Doppler radar processing based on FPGA for human sensing applications," *IEEE Trans. Geosci. Remote Sens.*, vol.51, no.5, May 2013.
- [18] D. T. Petkie, C. Benton, E. Bryan, "Millimeter wave radar for remote measurement of vital signs," *IEEE Radar Conference*, Pasadena, CA, pp.1–3, May 2009.
- [19] Changzhi Li and Jenshan Lin, "Random body movement cancellation in Doppler radar vital sign detection," *IEEE Trans. Microwave Theory & Tech.*, vol.56, no.12, pp.3143-3152, November 2008.
- [20] Y. Wang, Q. Liu and A. E. Fathy, " Simultaneous localization and respiration detection of multiple people using low cost UWB biometric pulse Doppler radar sensor," *IEEE MTT-S International Microwave Symposium Digest*, Jun. 2012.
- [21] Y. Wang, Q. Liu and A. E. Fathy, "CW and pulse-Doppler radar processing based on FPGA for human sensing applications," *IEEE Transactions on Geoscience and Remote Sensing*, vol.51, no.5, pp.3097-3107, May 2013.
- [22] Yanyun Xu, Shun Dai, Shiyou Wu, Jie Chen and Guangyou Fang, "Vital sign detection method based on multiple higher order cumulant for ultrawideband radar," *IEEE Transactions on Geoscience and Remote Sensing*, vol.50, no.4, pp.1254-1265, April 2012.
- [23] A. Lazaro, D. Girbau, and R. Villarino, "Analysis of vital signs monitoring using an ir-UWB radar," *Progress In Electromagnetics Research*, vol.100, 265-284, 2010.
- [24] Changzhi Li and Jenshan Lin, "Random body movement cancellation in Doppler radar vital sign detection," *IEEE Transactions on Microwave Theory and Techniques*, vol.56, no.12, pp.3143-3152, November 2008.
- [25] Byung-Kwon Park, Boric-Lubecke, O. and Lubecke, V.M., "Arctangent demodulation with DC offset compensation in quadrature Doppler radar receiver systems," *IEEE Transactions on Microwave Theory and Techniques*, vol.55, no.5, pp.1073-1079, May 2007.

- [26] Q. Zhou, J. H. Liu, A. Host-Madsen, O. Boric-Lubecke, and V. Lubecke, "Detection of multiple heartbeats using Doppler radar," in *Proceedings, IEEE International Conference on Acoustics, Speech and Signal Processing (ICASSP)*, vol.2, pp.1160-1163, 2006.
- [27] Yun Seo Koo, L.-Y. Ren, Yazhou Wang, Aly Fathy, "UWB MicroDoppler Radar for Human Gait Analysis, Tracking More Than One Person, and Vital Sign Detection of Moving Persons," *IEEE MTT-S International Microwave Symposium Digest*, Jun. 2013.

Chapter 5

- [1] L. Yousefi, B. Mohajer-Iravani, Omar M. Ramahi, "Enhanced Bandwidth Artificial Magnetic Ground Plane for Low-Profile Antennas," *Antennas and Wireless Propagation Letters, IEEE*, vol.6, no., pp.289-292, 2007.
- [2] J. M. Bell and M. F. Iskander "A low-profile archimedean spiral antenna using an EBG ground plane," *IEEE Antennas Wireless Propag. Lett.*, vol.3, pp.223-226 2004.
- [3] S. Wang, A.P. Feresidis, G. Goussetis, J.C. Vardaxoglou, "Low-profile resonant cavity antenna with artificial magnetic conductor ground plane," *Electronics Letters*, vol.40, no.7, pp.405, 406, 1 April 2004.
- [4] D. Bonefačić, S. Hrabar and D. Kvakar "Experimental investigation of radiation properties of an antenna embedded in low-permittivity thin-wire-based metamaterials," *Microw. Opt. Technol. Lett.*, vol.48, no.12, pp.2581-2586 2006.
- [5] J. Rayno, M.F. Iskander, N. Celik, "Synthesis of Broadband True-3D Metamaterial Artificial Magnetic Conductor Ground Planes Using Genetic Programming," *Antennas and Propagation, IEEE Transactions on*, vol.62, no.11, pp.5732, 5744, Nov. 2014.
- [6] R. S. Yahya and J. H. Kim "Implanted antennas in medical wireless communications," *Synthesis Lectures Antennas*, vol.1, no.1, pp.1 -82 2006.
- [7] S. Simms, V. Fusco, "Thin radar absorber using artificial magnetic ground plane," *Electronics Letters*, vol.41, no.24, pp.1311,1313, 24 Nov. 2005

APPENDIX

Appendix A Matlab Code

This appendix presents all the Matlab code we have used in Chapter IV.

A. Conventional Algorithm and Logarithm Algorithmic Algorithm for Vital Signs Detection

```
clc
clear all
close all
Freq=75;
Number_pulse=150;
num=11008;
filename = '20141123_190254_CH7.dat';
fp=fopen(filename,'rb');
fseek(fp,Number_pulse*num*2*2,-1); % begin of file, I Q, 16bit
data1=fread(fp,'uint16');% I0 Q0 I1 Q1 ...
fclose(fp);
%read I Q data
N_pulse = 2*round(length(data1)/num/2/2-1);
sigwave1 = zeros(num, N_pulse);
for i1 = 1 : 1 : N_pulse
    data_I_1 = data1((i1-1)*num*2+1:2:i1*num*2)-32768;
    data_Q_1 = data1((i1-1)*num*2+2:2:i1*num*2)-32768;
    sigwave1(:,i1) = data_I_1 + j*data_Q_1;
end
% set time window
start1=2300;%2300
end1=2440;%2440
% conventional method
slow_time=sum(sigwave1(start1:end1,:));
slow_time=slow_time-mean(slow_time);
sig1=sigwave1(start1:end1,:);
x1_fourier=zeros(1,N_pulse);
signal_ln=zeros(1,N_pulse);
x_label=linspace(0,5,5/(Freq/N_pulse));
fft_direct=fft(slow_time);
figure

plot(x_label,abs(fft_direct(1:length(x_label)))/max(abs(fft_direct(1:length(x_label)))));
    title('Conventional
method','linewidth',12,'fontsize',12,'Fontname','Timesnewroman','fontWeight','bold')
    xlabel('Frequency
(Hz)','linewidth',12,'fontsize',12,'Fontname','Timesnewroman','fontWeight','bold')
    ylabel('Normalized
Spectrum','linewidth',12,'fontsize',12,'Fontname','Timesnewroman','fontWeight','bold')
    dlmwrite('direct_x.txt',x_label')
```

```

dlmwrite('direct.txt', (abs(fft_direct(1:length(x_label)))/max(abs(fft_d
irect(1:length(x_label))))))')
%logarithmic method
for i1=1:1:N_pulse
    for j1=1:1:end1+1-start1
        x1_fourier(i1)=x1_fourier(i1)+sig1(j1,i1);
    end
    signal_ln(i1)=imag(log(x1_fourier(i1)));
end
signal_ln=unwrap(signal_ln);
signal_ln=signal_ln-mean(signal_ln);

t=N_pulse/Freq*linspace(0,1,N_pulse);
fft_signal_ln=fft(signal_ln);
x_label=linspace(0,5,5/(Freq/N_pulse));
figure %plot time domain signal
time_domain=(1:1:N_pulse)/Freq;
plot(time_domain,real(ifft(fft_signal_ln))*0.1/4/3.14*1000);
title('Singnal demodulated with logarithmic
method', 'linewidth',12, 'fontsize',12, 'Fontname', 'Timesnewroman', 'fontWeigh
t', 'bold')
xlabel('tiem
(s)', 'linewidth',12, 'fontsize',12, 'Fontname', 'Timesnewroman', 'fontWeigh
t', 'bold')
ylabel('Amplitude
(mm)', 'linewidth',12, 'fontsize',12, 'Fontname', 'Timesnewroman', 'fontWeigh
t', 'bold')
dlmwrite('subject2timesignalx.txt', (time_domain)')

dlmwrite('subject2timesignaly.txt', (real(ifft(fft_signal_ln))*0.1/4/3.1
4*1000)')

%belt sensor, reference for respiration rate
temporary=load('breath1.txt');
breath=temporary(:,2);
breath_num=length(breath);
breath=breath-mean(breath);
breath_freq=50;
fft_breath=fft(breath);
breath_label=linspace(0,5,5/(breath_freq/breath_num));
%pulse sensor, reference for heart rate
test2=load('ren1.txt');
sensor_num=length(test2);
sensor_freq=50;
cutoff_sensor1=round(0.4/(sensor_freq/sensor_num));
cutoff_sensor2=round(2/(sensor_freq/sensor_num));
cutoff_sensor3=round(37/(sensor_freq/sensor_num));
fft_sensor=fft(test2);
fft_sensor(1:cutoff_sensor1)=0;
fft_sensor(sensor_num-cutoff_sensor1:sensor_num)=0;
fft_sensor(cutoff_sensor2:sensor_num-cutoff_sensor2)=0;
figure
sensor_label=linspace(0,5,5/(sensor_freq/sensor_num));

```

```

plot(sensor_label,abs(fft_sensor(1:length(sensor_label)))/max(abs(fft_s
ensor(1:length(sensor_label)))), 'k:');
    dlmwrite('heartsensorx.txt', (sensor_label)')

dlmwrite('heartsensory.txt', (abs(fft_sensor(1:length(sensor_label)))/ma
x(abs(fft_sensor(1:length(sensor_label))))))')

hold on
plot(breath_label,abs(fft_breath(1:length(breath_label)))/max(abs(fft_b
reath(1:length(breath_label)))));
    dlmwrite('breathsensorx.txt', (breath_label)')

dlmwrite('breathsensory.txt', (abs(fft_breath(1:length(breath_label)))/m
ax(abs(fft_breath(1:length(breath_label))))));
    hold on

y2=abs(fft_signal_ln(1:length(x_label)))/max(abs(fft_signal_ln(1:length
(x_label))));
    plot(x_label,y2, 'r--');
        dlmwrite('uwbx.txt',x_label')
        dlmwrite('uwby.txt',y2')
    xlabel('Frequency
(Hz)', 'linewidth',12, 'fontsize',12, 'Fontname', 'Timesnewroman', 'fontWeig
ht', 'bold')
    ylabel('Normalized
Spectrum', 'linewidth',12, 'fontsize',12, 'Fontname', 'Timesnewroman', 'font
Weight', 'bold')
    h_legend=legend('Heart rate Reference', 'Respiration Reference', 'UWB')
    set(h_legend, 'fontWeight', 'bold');
    xlim([0 3])

```

VITAE

Yun Seo Koo was born in Seoul, Republic of Korea, in 1977. He received the B.S degree in Physics and Electronics Engineering from Sogang University, Seoul, Republic of Korea 2005. And the M.S degree in Electrical Engineering from Polytechnic University, Brooklyn, New York in 2008 and the Ph.D degree in Electrical Engineering from The University of Tennessee, Knoxville, in 2015.

In summer 2013, he was an intern IC design engineer with the RF Micro Devices, Greensboro, NC, where he was engaged in the development of RFIC amplifiers at 2.4GHz. His current research interests include UWB systems for biomedical applications, RFIC/MMIC design, and UWB antennas.